Stabilizing Degenerate Dopants in Colloidal Semiconductor Nanocrystals

Kimberly H. Hartstein

A dissertation
submitted in partial fulfillment of the
requirements for the degree of

Doctor of Philosophy

University of Washington
2018

Reading committee:
Daniel R. Gamelin, Chair
Brandi M. Cossairt
David J. Masiello

Program authorized to offer degree:
Chemistry

University of Washington

Abstract

Stabilizing Degenerate Dopants in Colloidal Semiconductor Nanocrystals

Kimberly H. Hartstein

Chair of the Supervisory Committee:
Professor Daniel R. Gamelin
Department of Chemistry

Semiconductor nanocrystals possessing excess delocalized charge carriers are garnering considerable attention for their applications in a wide range of emerging technologies. In order to realize their incorporation into practical devices, a detailed understanding of their electronic structural properties is essential. Precise control over the introduction and removal of degenerate dopants from semiconductor nanostructures presents exciting opportunities for careful study of their electronic structures and associated capabilities. This thesis explores the careful incorporation and characterization of the stability of degenerate dopants in semiconductor nanomaterials. Chapter 1 introduces degenerately doped semiconductor nanocrystals, briefly describing methods to incorporate and confirm the presence of excess charge carriers. We explore factors that influence charge carrier stability in a variety of semiconductor nanocrystal lattices and consider what limits the extent of stable carrier incorporation. Chapter 2 investigates the stability of degenerate dopants in *n*-doped CdSe/CdS core/shell quantum dots and explores

their luminescent signatures. These studies reveal that CdS shell deposition greatly slows electron trapping, and we characterize the luminescence from a photogenerated four-carrier negative tetron (three electrons and one hole). Chapter 3 applies *in situ* spectroelectrochemical potentiometry to quantify the Fermi-level energy in *p*-doped plasmonic copper-sulfide nanocrystals. We reversibly tune the plasmon absorption band using redox chemistry and demonstrate identical absorption bands in low-chalcocite copper-sulfide nanocrystals with and without cation vacancies. This work demonstrates that cation vacancies internal to the nanocrystal lattice are far more effective at stabilizing free carriers than anions at the nanocrystal surfaces. Chapter 4 applies magnetic circular dichroism (MCD) spectroscopy to identify classical cyclotron splittings in plasmonic semiconductor nanocrystals and compares their magnetic signatures with those exhibited by plasmonic metal nanoparticles. We demonstrate that the sign of the MCD signal is sensitive to the sign of the carriers (*n* or *p*), and that the magnitude of the cyclotron splitting reflects the carrier effective masses for the delocalized carriers. Overall, this work focuses on stable incorporation of degenerate dopants into semiconductor nanocrystals as a method to improve our understanding of the fundamental electronic structural properties of these materials to work toward their implementation into practical device architectures.

In loving memory of
Betty Hoffmann

Acknowledgements

I want to begin by thanking Prof. Daniel Gamelin for providing a home for me in his lab at the University of Washington and for giving me access to every resource to assist me on my scientific journey. Your dedication and knowledge of inorganic chemistry, spectroscopy, and nanoscience are truly an inspiration. I feel incredibly fortunate to have an advisor who tailors his mentorship so specifically to each individual student. Your leadership fosters an exceptionally collaborative community where I've had the pleasure of working with wonderful colleagues, coauthors, and friends.

I'll try to keep this short, but I really do feel compelled to thank some individual members of the Gamelin Group for their contributions to my time in grad school. Dr. Charlie Barrows, thank you for sharing your ice cream with me and for being my first friend in Seattle. I'm so happy that our shared love for waffles and M&M bowl-in-a-bowls planted the seed for what became a meaningful friendship. Katherine Bryant, you're awesome and I'm forever thankful that you introduced me to the Wine & Novels family. Dr. Liam Bradshaw, thank you for sharing bread and wisdom with me. Dr. Mike Carroll, thanks for directing me so I could catch pop-ups when I played right field for the Ligand Fielders. I want to express my gratitude to Prof. Katie Knowles for spearheading team copper, to Prof. Emily Tsui for teaching me (more than I ever wanted to know) about nanocrystal surface chemistry, and to Dr. Arianna Marchioro for always being available for tech support and troubleshooting. Thank you to Dr. Patrick Whitham also for tech support, and for baking the most incredible pies. Keep it up, especially with the sweet potatoes. Prof. Carl Brozek, thank you for asking tough questions and for helping me to become a better scientist. To the newly minted Dr. Heidi Nelson, thank you for going on this journey alongside me. It's been so rewarding to watch you grow both professionally and personally. Michael De Siena, thank you for scientific (and emotional) support. Let it be stated that your fish survived (and thrived) under my supervision. Jose Araujo, you are among the most selfless people I know. Somehow you always complete the task I left half-finished and ask for nothing in return. You are an incredible coworker and friend. Christian Erickson, your nanocrystal heterostructures were heaven-sent, your relentless mockery less so. Thanks for making me think outside the box. Tyler Milstein, I don't always understand your jokes but I can still tell you're a funny guy. Ted Cohen, your upbeat outlook is a great asset. Dr. Sid Creutz, I admire your capabilities as both a brilliant scientist and a reliable labmate. Dr. Dan Kroupa, I always appreciate your positive attitude, fresh perspective, and innovative ideas. I'm also happy you share my enthusiasm for Imo's pizza and Cardinal baseball. Diana Roh, I can see that the future of the group is in good hands. Next time we meet, I expect it to be in some exotic land. Skylar Sherman, I was supposed to be mentoring you, but often it worked the other way around. Thank you for everything you've taught me – your intelligence, enthusiasm, and open-mindedness are a triple threat and I am so excited to see where life takes you. Prof. Victor Polinger, thank you for making weekly group meetings more informative and more enjoyable. I benefited a great deal from interacting with you. Kira Hughes and Prof. Alina Schimpf, the friendships I've built with each of you are among my favorite products from my time as a grad student. I am a better person for having you two in my life.

Also beyond the walls of the lab, the Department of Chemistry has been a wonderfully supportive environment. I cherish my memories of time spent with fellow grad students and post-docs, from winning IM softball championships, to midday coffee breaks and celebrating milestones at Big Time Brewery. Thank you to Prof. Brandi Cossairt for being a standout mentor and role model, and to Dr. Danielle Henckel and Jenny Stein for your camaraderie.

Thank you to Prof. Efrat Lifshitz for hosting me at the Technion in Israel for an incredible summer research experience, and to Yahel Barak and the rest of the Lifshitz Group for creating an incredibly hospitable work environment that far surpassed my expectations. I want to express my gratitude to the Monday Junta crew for helping me to explore so much of Israel in a very short period of time, and to Avi Shumacher for making Haifa feel like a home. Our friendship remains very special to me.

I want to thank my undergraduate research advisor, Prof. Sophia Hayes. I absolutely would not be where I am today without your encouragement, guidance, and support. Thank you for believing in me in those early days, and for patiently helping me to believe in myself.

Outside of science, the community at Shakti Vinyasa Yoga has been instrumental in helping me to discover and reconnect with the values I cherish most. Thank you also to the staff and fellow volunteers at the Queen Anne Food Bank for your kindness and for helping me engage with my community, something that I find so incredibly fulfilling.

To the most wonderful book club, Wine & Novels – you ladies support me in ways I never dreamed possible. Thank you for sharing your homes and your hearts with me, and for absolutely *always* being there. You make me my best.

To Marianna Sofman, thank you for being my interactive diary and most trusted ally. Germany was one of the best things to ever happen to me, in large part because I met you.

To Prof. Mike Larsen, your endless support and encouragement overwhelm me more each day. I am forever grateful for you.

My family, biological and chosen, means everything to me. I am incredibly fortunate to have grown up surrounded by a close network of aunts and uncles, cousins, grandparents, and dear friends (*i.e.* family). You are too many to name individually in these pages, but please know that you are so very appreciated.

And finally, to my main three – Mama, thank you for being so uniquely you, and always encouraging me to be me. I am so lucky to have the greatest role model and my best friend in a single package. Dad, thank you for finding the most innovative ways to teach me, to motivate me, and to relate to me. Your creativity and your passion are my greatest inspirations. David, you are forever my moral compass and without a doubt the best person I will ever know. To all three of you, thank you for always encouraging me to strive for greatness and for demonstrating how through your own examples. I love you loads and then some.

Table of Contents

List of Figures and Schemes

List of Tables

Abbreviations and Chemical Symbols

Ag	Silver
Au	Gold
AZO	Aluminum-doped zinc oxide
$[BAr^F_4]^-$	Tetrakis(3,5-trifluoromethylphenyl)borate
CB	Conduction band
CdS	Cadmium sulfide
CdSe	Cadmium selenide
$CoCp^*_2$	Decamethylcobaltocene
Cu	Copper
Cu_2S	Copper sulfide
Cu_2Se	Copper selenide
$Cu_{2-x}S$	Copper-deficient copper sulfide
$Cu_{2-x}Se$	Copper-deficient copper selenide
CW	Continuous wave
E_F	Fermi level
E_g	Band gap
EPR	Electron paramagnetic resonance
EtOH	Ethanol
eV	Electronvolts
e^-_{CB}	Conduction-band electron
Fc	Ferrocene
Fc^+	Ferrocenium
$[FeCp^*_2]^+$	Decamethylferrocenium
h^+_{VB}	Valence-band hole
IR	Infrared
IRF	Instrument response function
ITO	Tin-doped indium oxide
I_2	Iodine
$[I]^-$	Iodide
$LiBEt_3H$	Lithium triethylborohydride
LSPR	Localized surface plasmon resonance
MCD	Magnetic circular dichroism
MCET	Metal-ion coupled electron transfer
meV	Millielectronvolts
m^*	Carrier effective mass
NIR	Near-infrared
$\langle n \rangle$	Average number of excess conduction-band electrons per nanocrystal
$[OTf]^-$	Triflate
PL	Photoluminescence
QD	Quantum dot
QY	Quantum yield (photoluminescence)
TBAI	Tetrabutylammonium iodide
$TBAPF_6$	Tetrabutylammonium hexafluorophosphate
TRPL	Time-resolved photoluminescence

THF	Tetrahydrofuran
VB	Valence band
V_{OC}	Open-circuit potential
XRD	X-ray diffraction
X	Exciton
X^-	Negative trion
X^{2-}	Negative tetron
ZnO	Zinc oxide

Chapter 1: Introduction

1.1 Overview

Semiconductor nanocrystals possessing excess band-like charge carriers are attracting considerable attention for their applications in a wide range of emerging technologies, from solar energy conversion to photocatalysis and bioimaging.[1,2] A complete understanding of the fundamental electronic structural properties of these materials is a prerequisite to their implementation in functional device architectures. The ability to precisely, stably, and reversibly incorporate degenerate dopants into semiconductor nanocrystals enables systematic study of their band structures through careful characterization of the influence of free carriers on optoelectronic properties. Here we begin with a brief introduction to the incorporation of degenerate dopants (*n*- and *p*-type carriers) into semiconductors to make them more metallic in nature and describe how to confirm the presence of band-like charge carriers in semiconductor nanocrystals. We demonstrate that the location of the charge-compensating ion plays a crucial role to the stability of degenerate dopants in nanocrystals at high free-carrier concentrations. Spectroscopic observations and spectroelectrochemical measurements reveal that nanocrystal surface chemistry can also impact the incorporation and stability of degenerate dopants, limiting some semiconductor materials to more modest carrier concentrations. The work highlighted here is intended as an exploration of considerations relevant to incorporating and stabilizing degenerate dopants in colloidal semiconductor nanocrystals.

1.2 A brief introduction to band theory as it applies to extended solids

We can begin by considering the simple band diagram picture for common extended materials in Scheme 1.1, where continuous bands of electron orbitals are represented simply as cartoon blocks. The shaded regions indicate where valence electrons completely occupy the available orbitals, and the unfilled regions represent space for conduction. In a metal, the frontier band is only partially filled with electrons, leaving empty orbitals for conduction in direct contact with occupied orbitals. The Fermi level (E_F) is defined as the energy (or chemical potential) with 50 percent probability of finding an electron. In metals, E_F lies within one of the bands such that electrons can move freely throughout the band, yielding a conductive material.

Scheme 1.1. Band structure representation for common extended materials.

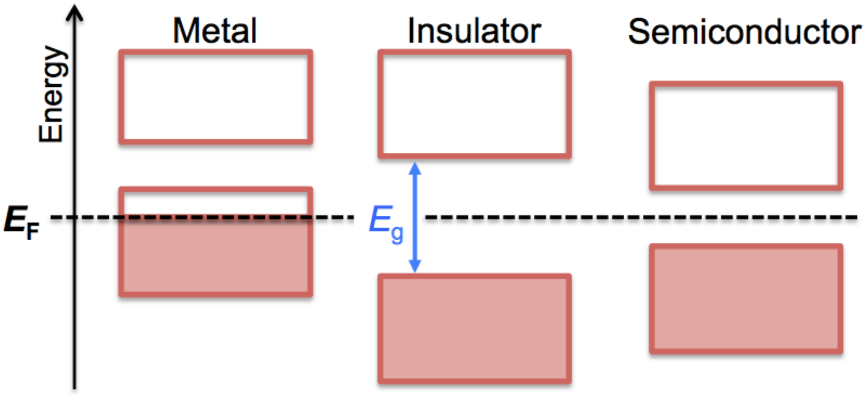

An insulating material (*e.g.* wood, plastic) is distinguished from a metal by its energetically sizable band gap (E_g) that separates its valence band (VB) and conduction band (CB) in energy. Semiconductors also possess a substantial band gap, but the energy of the semiconductor gap is smaller than that of an insulator. With an external input such as light, application of an electric bias, or even thermal energy, the semiconductor band gap can be overcome, introducing free electronic carriers and enabling conductive behavior in the material. E_F in insulators and in semiconductors intrinsically resides exactly in the middle of the band gap as indicated by the dashed line in Scheme 1.1. Here we discuss controlled introduction of free carriers into semiconductor nanocrystals to adjust E_F stably into one of the bands, modifying the semiconductor band structure to resemble that of a metal.

1.3 Incorporating degenerate dopants into semiconductor nanocrystals

Adding delocalized conduction-band electrons (e^-_{CB}) or valence-band holes (h^+_{VB}) into semiconductors is a useful way to introduce large free-carrier densities ($\langle N \rangle$ or $\langle P \rangle$ for e^-_{CB} and h^+_{VB}, respectively) and to methodically study the electronic properties of these materials. Scheme 1.2 depicts a generalized band structure for intrinsic, *n*-doped, and *p*-doped semiconductors and their associated Fermi-level energies (dashed lines), located in the middle of the band gap, and within the conduction and valence bands, respectively.

Scheme 1.2. E_F modulation in degenerately doped semiconductor materials.

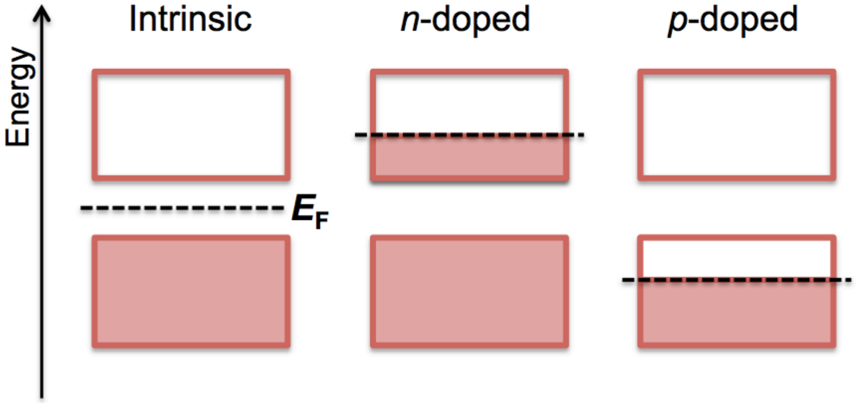

The last several decades of research on colloidal semiconductor nanocrystals demonstrate many unusual and potentially very useful characteristics of these materials. Their small dimensions make them subject to the effects of quantum confinement, and their tunable surface chemistries afford the opportunity to process them as solutions, making these materials uniquely suited for myriad applications and scalable production.[1,3-5] Degenerate doping is realized in nanocrystals through a variety of avenues,[6] including aliovalent[7-10] and vacancy-mediated doping,[11-14] chemical and electrochemical carrier injection,[15-20] and photodoping.[20-23] Aliovalent and vacancy-mediated doping are unique from the others in that these methods can be executed during particle formation, in many cases yielding air-stable charge carriers that are charge-compensated by dopants *internal* to the nanocrystal lattice. In contrast, the latter methods are attractive because they enable post-synthetic, oftentimes reversible charge carrier incorporation with ions at the nanocrystal *surface* responsible for charge compensation. Scheme 1.3 visually illustrates distinct motifs to charge-compensate excess e^-_{CB} in n-doped semiconductor nanocrystals, with either internal lattice dopant ions (d^+) or ions at the nanocrystal surface (Q^+). In either case, the nanocrystals remain overall net neutral in terms of charge. It is worth noting that the type of carriers incorporated (n or p) depends on the identity of the lattice and the method of carrier incorporation, and these factors determine which of the motifs from Scheme 1.3 applies to stabilize the incorporated carriers.

Scheme 1.3. Charge-compensation motifs in semiconductor nanocrystals.

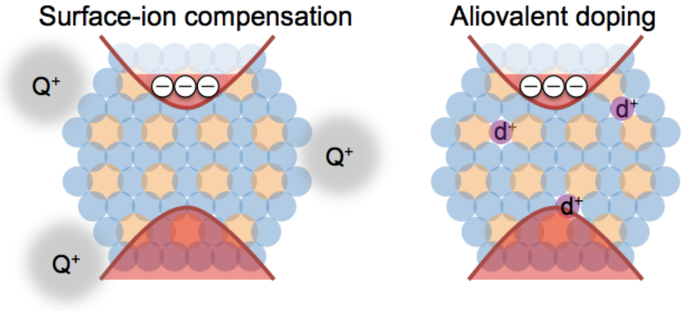

Regardless of the carrier type or mechanism for charge compensation, a host of hallmark spectroscopic characteristics confirm the presence of excess delocalized charge carriers in semiconductor nanocrystals.[6] Figure 1.1 highlights changes to the electronic absorption upon carrier incorporation in CdSe nanocrystals, where arrows indicate the direction of increasing $\langle N \rangle$. These changes include (1) bleaching of the first excitonic (interband) absorption feature due to carrier occupation of the band edge, and (2) introduction of a new absorption feature in the near-infrared (NIR) associated with intraband absorption of these band-edge carriers.

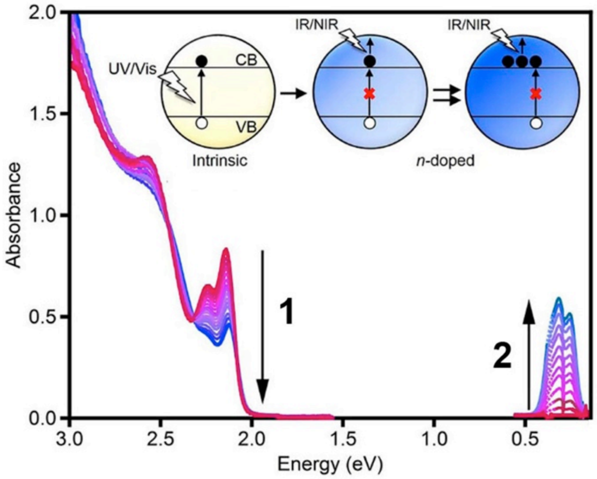

Figure 1.1. Spectroscopic signatures of delocalized charge carriers in CdSe nanocrystals include (1) bleaching of the first excitonic absorption feature and (2) introduction of intraband absorption in the NIR. Inset: Schematic depiction of the photodoping process. Figure reprinted from ref. 6.

The delocalized e_{CB}^{-} in Figure 1.1 were introduced through photodoping, a photo-initiated process to facilitate incorporation of stable band-edge carriers into semiconductor nanocrystals. This process is schematically depicted in the inset, where incident light with sufficient energy excites the material band gap, creating an exciton. In the presence of a suitable chemical reductant, h_{VB}^{+} is rapidly reduced, leaving e_{CB}^{-} charge-compensated by surface ions (as shown in Scheme 1.3). With excess reductant and continuous excitation, this process can occur repeatedly to build up a population of e_{CB}^{-} at the conduction-band edge. The spectroscopic signatures in

Figure 1.1 are generally universal to degenerately doped semiconductor nanocrystals, regardless of lattice identity, charge-compensation motif, and experimental conditions. However, these factors do substantially impact the extent to which E_F can be modulated. The implications of these effects will be explored in the following sections.

1.4 Relationship between charge-compensation motif and degenerate dopant stability

Aliovalent dopant incorporation is a highly effective method for introducing degenerate dopants into bulk semiconductor materials, where each lattice-incorporated dopant introduces one band-edge carrier. The extent of degenerate doping by this method is ultimately limited by the solubility of dopant ions in the host semiconductor nanocrystal lattice. Incorporating dopant ions into nanocrystal lattices can prove challenging due to self-purification and dopant expulsion to minimize free energy in the small nanostructures, but a number of novel synthetic tools are being developed to facilitate stable ion incorporation or even complete lattice transformation.[24-27] Using a suitable dopant/host combination, sufficient aliovalent dopant inclusion can yield relatively large values of $\langle N \rangle$ or $\langle P \rangle$ (up to 10^{21} cm^{-3} in some cases). At these high doping levels, the intraband absorption feature shown in Figure 1.1 is often (but not always) ascribed to a localized surface plasmon resonance (LSPR) due to resonant oscillation of delocalized carriers within the valence or conduction band for *n*- or *p*-doped materials, respectively.[7,12,14,28-31] LSPRs and their magnetic signatures will be discussed in Chapter 4.

n-doped Al^{3+}:ZnO (AZO) is a classic example of aliovalent doping in a common semiconductor nanocrystal lattice to achieve high quantities of free carrier inclusion, yet studies reveal that only ~5% of Al^{3+} (substituted for lattice Zn^{2+}) actually yield electron incorporation.[32] Similar discrepancies have been reported between number of dopants and number of free carriers for *n*-doped Sn^{4+}:In_2O_3 (ITO)[33,34] and *p*-doped Ag^+:PbSe nanocrystals.[10] Systematic studies on the radial distribution of Sn^{4+} ions in ITO nanocrystals demonstrate incorporation of greater $\langle N \rangle$ values when dopants are located central to the nanocrystal core and spatially isolated from the surface.[35] In all of these systems, many of the aliovalent dopant ions presumably reside at or near to nanocrystal surfaces, and are likely charge-compensated at the nanocrystal surface by ligand stoichiometries or surface ions. Beyond some critical amount of dopant solubility and lattice incorporation, dopant ions likely adsorb to the nanocrystal surface and nearby ligands rearrange to accommodate the charge imbalance, limiting the stabilization of additional free carriers.[10]

Despite competition from dopant compensation at nanocrystal surfaces, aliovalent doping is highly effective at stabilizing considerable free-carrier densities in semiconductor nanocrystals. In fact, at a common value of $\langle N \rangle$ and with nearly indistinguishable spectroscopic signatures, e^-_{CB} are demonstrably less reactive in AZO nanocrystals than comparable e^-_{CB}:ZnO prepared *via* photodoping with EtOH as the sacrificial reductant (*i.e.* H^+ at the nanocrystal surface for charge compensation).[32] A similar result is observed when comparing the stability of e^-_{CB} in *n*-doped ITO and In_2O_3 nanocrystals.[36] Scheme 1.4 conveys the idea that instead of raising E_F (represented here as chemical potential), incorporating Sn^{4+} dopants stabilizes the conduction-band edge of In_2O_3 nanocrystals, such that E_F of the as-prepared nanocrystals (V_0) remains constant, irrespective of Sn^{4+} content and $\langle N \rangle$ value.

Scheme 1.4. Stabilization of In_2O_3 band edges through Sn^{4+} incorporation. Reprinted from ref. 36.

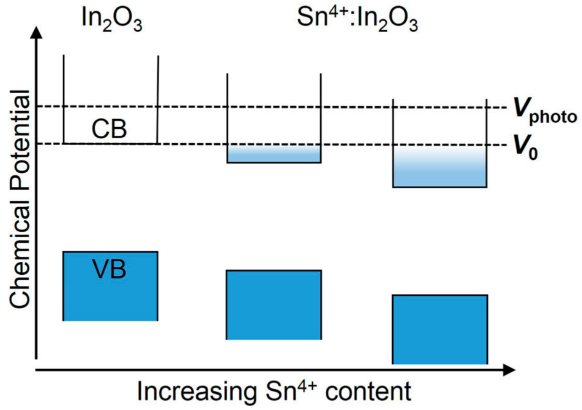

Scheme 1.4 shows that although $\langle N \rangle$ scales with Sn^{4+} content for any given ensemble of nanocrystals, the value of additional $\langle N \rangle$ incorporable *via* photodoping remains constant independent of Sn^{4+} content. In this manner, the maximum achievable Fermi-level (E_F^{max}, V_{photo} in Scheme 1.4) equilibrates at a common value for a series of In_2O_3-ITO nanocrystals despite disparate levels of aliovalent dopant inclusion.

This shared value of E_F^{max} achievable *via* photodoping can be explained by examining what limits the extent of photodoping. When ZnO nanocrystals are photodoped with EtOH serving as the sacrificial h_{VB}^{+} reductant, $\langle N \rangle$ increases and E_F rises until it reaches the chemical potential associated with the reaction that reverses the photo-oxidation of EtOH (aldehyde hydrogenation).[37] Thus under these conditions, ZnO nanocrystals consistently photodope to a constant carrier density of $\langle N_{max} \rangle \sim 1.4 \times 10^{20}$ cm^{-3} regardless of nanocrystal size.[22,31] When more reducing $Li[Et_3BH]$ instead serves as the hole quencher, ZnO can incorporate nearly 4× as many carriers ($\langle N_{max} \rangle \sim 6 \times 10^{20}$ cm^{-3}).[22] Reported values of $\langle N_{max} \rangle$ vary also with the identity of the cation, suggesting that the cation's ability to approach the nanocrystal surface and/or intercalate into the lattice for charge compensation influence the extent of photodoping.[22]

Interestingly, photodoping ZnO even with EtOH results in a greater quantity of more thermodynamically stable electrons (by ~600 mV at a common value of $\langle N \rangle$) than e^-_{CB}:ZnO introduced chemically with decamethylcobaltocene (CoCp$^*_2$).[37] In this case, $E_{\mathrm{F}}^{\mathrm{max}}$ is limited only by the reducing potential of the chemical reducant and/or its ability to reduce something else in solution. Photoreduction in the presence of EtOH yields more stable e^-_{CB} than chemical reduction, likely because H$^+$ becomes closely associated with the nanocrystal surface and is thus more stabilizing than the bulkier [CoCp$^*_2$]$^+$ cation. Potentiometric titrations on ZnO nanocrystals further demonstrate[38] and a theoretical "charged sphere" model support[39] this notion that the physical proximity of charge-compensating cations to the nanocrystal surface impacts the stability of E_{F} substantially. Chapter 3 of this thesis applies spectroelectrochemical potentiometry to directly probe the impact of charge-compensating ion location on the thermodynamic stability of free carriers in *p*-doped copper-sulfide nanocrystals.

1.5 Prominent role of nanocrystal surfaces

Most of the materials considered thus far can sustain reasonably high carrier densities (>10^{20} cm^{-3}) with upper limits determined by solubility of dopant ions in the lattice or as described, a back-reaction involving redox-active species in solution external to the nanocrystal. For example, ZnO is intrinsically essentially free of mid-gap electron traps, and thus large quantities of photodoped electrons are indefinitely stable under rigorously anaerobic conditions. This is not true of many semiconductor nanocrystals, however, where redox-active surface species give rise to mid-gap trap states that can greatly impact optical and electronic properties of the material. In fact, such redox-active species are of paramount importance to the mechanism of photodoping CdSe nanocrystals, where surface-bound oxidized selenium moieties first undergo a dark reduction reaction with a suitable reducing agent to facilitate photodoping and stable e_{CB}^{-} incorporation when the nanocrystals are subsequently photoexcited.[40]

As a result of these rich surface chemistries, electronic dopants are easily trapped at redox-active mid-gap trap states, limiting the extent of stable dopant incorporation. The maximum number of e_{CB}^{-} incorporable *via* photodoping ($\langle n_{\mathrm{max}}\rangle$) is determined in CdSe nanocrystals by kinetic competition between the rates of photodoping and carrier trapping, and thus varies considerably with experimental conditions.[41] Figure 1.2A shows absorption spectra of undoped CdSe, and n-doped CdSe nanocrystals with Cd^{2+}- and Se^{2-}-enriched surfaces photodoped to $\langle n_{\mathrm{max}}\rangle$. Values of $\langle n\rangle$ in CdSe are determined according to the relationship $\langle n\rangle = (|2\Delta A/A_0|)$ where $\Delta A/A_0$ is the normalized bleach intensity at the first exciton because the conduction-band edge in CdSe is 2-fold degenerate. The Cd^{2+}-enriched nanocrystals in Figure 1.2A reach a larger value of $\langle n_{\mathrm{max}}\rangle$ than the same nanocrystals enriched with Se^{2-} anions. The inset plots the slow recovery of the absorption bleach intensity as $-\Delta A/A_0$ *vs* time after photodoping, demonstrating that carrier trapping occurs on relatively long timescales in CdSe nanocrystals.[41] These long timescales are consistent with atomic rearrangements at nanocrystal surfaces often held responsible for luminescence intermittency ("blinking") at the single nanoparticle level.[41-44]

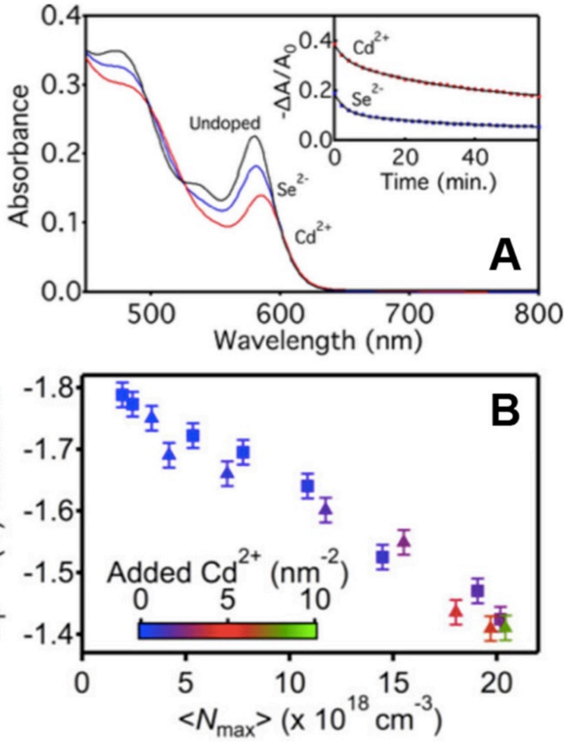

Figure 1.2. **(A)** Electronic absorption spectra of undoped CdSe nanocrystals (black), and *n*-doped CdSe with Cd^{2+}- (red) and Se^{2-}-enriched (blue) surfaces, photodoped with $Li[Et_3BH]$ to incorporate $\langle n_{\mathrm{max}} \rangle$ e^-_{CB} . Inset: Normalized differential absorption intensity characterizes slow anaerobic recovery after photodoping. Reprinted from ref. 41. **(B)** $E_{\mathrm{F}}^{\mathrm{max}}$ *vs* $\langle N_{\mathrm{max}} \rangle$ for CdSe nanocrystals (d = 4.4 nm, d = 5.5 nm) with different amounts of Cd^{2+} added per unit surface area to Se^{2-}-enriched nanocrystals. Reprinted from ref. 45.

The absorption spectra in Figure 1.2A highlight the importance of nanocrystal surface chemistry to the incorporation of electronic dopants, and electrochemical characterization provides insight into the physical origin for this behavior. Plotting $E_{\mathrm{F}}^{\mathrm{max}}$ *vs* $\langle N_{\mathrm{max}} \rangle$ for 2 sizes of CdSe as in Figure 1.2B reveals that adding increasing amounts of Cd^{2+} to nanocrystal surfaces enables incorporation of greater $\langle n \rangle$ values and stabilizes the associated E_{F} values. Analysis of these data suggests that Se^{2-}-enrichment at CdSe nanocrystal surfaces induces dipoles that can destabilize experimental conduction-band edge potentials by up to 400 mV relative to nanocrystals with Cd^{2+}-enriched surfaces.[45] The data demonstrate that regardless of size, there is a linear relationship between $E_{\mathrm{F}}^{\mathrm{max}}$ and $\langle N_{\mathrm{max}} \rangle$ in *n*-doped CdSe nanocrystals, and that both values are highly tunable (400 mV in $E_{\mathrm{F}}^{\mathrm{max}}$ and an order of magnitude in $\langle N_{\mathrm{max}} \rangle$) simply by altering the degree of ion enrichment at the nanocrystal surfaces.

These observations facilitate creation of the picture in Figure 1.3, where some trap probability distribution exists at the nanocrystal surface originating from slow rearrangement of nanocrystal surfaces.[41] The position of the band edges as drawn are highly tunable and can be made more or less stable (more positive or negative in chemical potential, respectively) relative to the trap distribution by tuning the size of the nanocrystal, and as evidenced in Figure 1.2B, by altering the surface stoichiometry. A similar picture likely applies to degenerately doped PbSe nanocrystals.[46] Ultimately, rapid trapping of carriers out of the conduction band and into surface states plays a significant role in determining the value of $\langle n_{\mathrm{max}} \rangle$ achievable by a given nanocrystal ensemble in materials with relevant mid-gap trap states, in stark contrast to metal oxide systems discussed in the previous section.

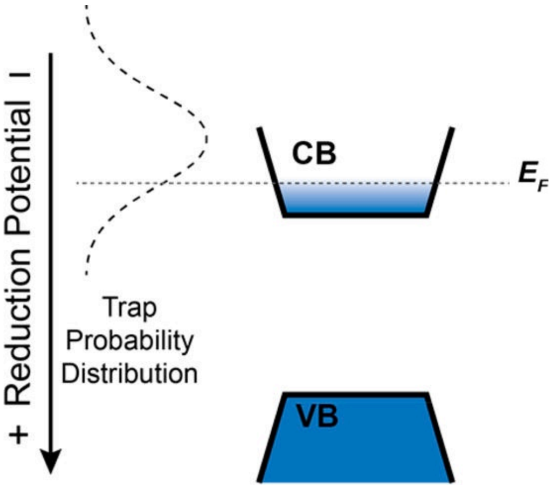

Figure 1.3. Schematic depiction of the relationship between a trap potential's fluctuating probability distribution and the band edges of photodoped colloidal CdSe nanocrystals. Adapted from ref. 41.

Consistent with this discussion of surface states, passivating nanocrystal surfaces with shells reduces the rate of carrier trapping noticeably, increasing $\langle n_{\mathrm{max}} \rangle$ and stabilizing conduction-band carriers substantially.[16,47] Similarly, thin films of CdSe/CdS core/shells under an applied electrochemical potential support more robust carriers than unshelled CdSe nanocrystals under similar conditions.[48] Even in core/shell heterostructures, $\langle N_{\mathrm{max}} \rangle$ cannot attain values $>10^{20}$ cm^{-3} and anaerobic recovery is slowed but not altogether suppressed, suggesting that perhaps thicker shells or alternative heterostructures are required to prevent rapid trapping of e_{CB}^{-} under these conditions. *n*-doped CdSe/CdS heterostructures and their photoluminescent signatures will be discussed in detail in Chapter 2.

1.6 Summary & conclusions

A thorough understanding of degenerately doped semiconductor nanocrystal fundamentals is essential to their controlled tunability and implementation for a variety of emerging technologies. It is imperative to characterize not only the mechanisms for incorporating excess carriers into semiconductor nanocrystals, but also the factors that impact the stability of those carriers and ultimately limit the extent of achievable carrier incorporation. Redox-active surface species in *n*-doped CdSe and PbSe nanocrystals enable e_{CB}^{-} trapping at mid-gap trap states, facilitating anaerobic recovery and limiting $\langle N_{\mathrm{max}} \rangle$ to modest values relative to *n*-doped metal oxide nanocrystals (*e.g.* ZnO, AZO, $\mathrm{In_2O_3}$, ITO), where mid-gap electron traps are not present and/or inconsequential to carrier incorporation. Instead, $\langle N_{\mathrm{max}} \rangle$ in these materials is governed by competition from some other redox reaction or external mechanism for charge compensation. Studies of reactivity and spectroelectrochemical measurements indicate that the location of the charge-compensating ion significantly impacts E_{F}, even at constant carrier densities. Knowledge of processes that govern the extent of carrier inclusion in colloidal semiconductor nanocrystals and development of methods to quantify the stability of free carriers are vital to the practical implementation of these materials in emerging technological applications.

1.7 References

1. Kovalenko, M. V.; Manna, L.; Cabot, A.; Hens, Z.; Talapin, D. V.; Kagan, C. R.; Klimov, V. I.; Rogach, A. L.; Reiss, P.; Milliron, D. J.; Guyot-Sionnest, P.; Konstantatos, G.; Parak, W. J.; Hyeon, T.; Korgel, B. A.; Murray, C. B.; Heiss, W., Prospects of Nanoscience with Nanocrystals. *ACS Nano* **2015,** *9*, 1012-1057.
2. Vanmaekelbergh, D.; Liljeroth, P., Electron-Conducting Quantum Dot Solids: Novel Materials Based on Colloidal Semiconductor Nanocrystals. *Chem. Soc. Rev.* **2005,** *34*, 299-312.
3. Smith, A. M.; Nie, S., Semiconductor Nanocrystals: Structure, Properties, and Band Gap Engineering. *Acc. Chem. Res.* **2010,** *43*, 190-200.
4. Boles, M. A.; Ling, D.; Hyeon, T.; Talapin, D. V., The Surface Science of Nanocrystals. *Nat. Mater.* **2016,** *15*, 141-153.
5. Efros, A. L.; Rosen, M., The Electronic Structure of Semiconductor Nanocrystals. *Annu. Rev. Mater. Sci.* **2000,** *30*, 475-521.
6. Schimpf, A. M.; Knowles, K. E.; Carroll, G. M.; Gamelin, D. R., Electronic Doping and Redox Potential Tuning in Colloidal Semiconductor Nanocrystals. *Acc. Chem. Res.* **2015,** *48*, 1929-1937.
7. Agrawal, A.; Johns, R. W.; Milliron, D. J., Control of Localized Surface Plasmon Resonances in Metal Oxide Nanocrystals. *Annu. Rev. Mater. Res.* **2017,** *47*, 1-31.
8. Buonsanti, R.; Llordes, A.; Aloni, S.; Helms, B.; Milliron, D., Tunable Infrared Absorption and Visible Transparency of Colloidal Aluminum-Doped Zinc Oxide Nanocrystals. *Nano Lett.* **2011,** *11*, 4706-4716.
9. Kanehara, M.; Koike, H.; Yoshinaga, T.; Teranishi, T., Indium Tin Oxide Nanoparticles with Compositionally Tunable Surface Plasmon Resonance Frequencies in the Near-IR Region. *J. Am. Chem. Soc.* **2009,** *131*, 17736-17737.
10. Kroupa, D. M.; Hughes, B. K.; Miller, E. M.; Moore, D. T.; Anderson, N. C.; Chernomordik, B. D.; Nozik, A. J.; Beard, M. C., Synthesis and Spectroscopy of Silver-Doped PbSe Quantum Dots. *J. Am. Chem. Soc.* **2017,** *139*, 10382-10394.
11. Elimelech, O.; Liu, J.; Plonka, A. M.; Frenkel, A. I.; Banin, U., Size Dependence of Doping *via* Vacancy Formation in Copper Sulfide Nanocrystals. *Angew. Chem. Int. Ed.* **2017,** *56*, 10335-10340.
12. Luther, J. M.; Jain, P. K.; Ewers, T.; Alivisatos, A. P., Localized Surface Plasmon Resonances Arising from Free Carriers in Doped Quantum Dots. *Nat. Mater.* **2011,** *10*, 361-366.
13. Manthiram, K.; Alivisatos, A., Tunable Localized Surface Plasmon Resonances in Tungsten Oxide Nanocrystals. *J. Am. Chem. Soc.* **2012,** *134*, 3995-3998.

14. Zhao, Y.; Pan, H.; Lou, Y.; Qiu, X.; Zhu, J.; Burda, C., Plasmonic $Cu_{2-x}S$ Nanocrystals: Optical and Structural Properties of Copper-Deficient Copper(I) Sulfides. *J. Am. Chem. Soc.* **2009,** *131*, 4253-4261.
15. Guyot-Sionnest, P., Charging Colloidal Quantum Dots by Electrochemistry. *Microchim Acta* **2008,** *160*, 309-314.
16. Koh, W.-K.; Koposov, A. Y.; Stewart, J. T.; Pal, B. N.; Robel, I.; Pietryga, J. M.; Klimov, V. I., Heavily Doped *n*-Type PbSe and PbS Nanocrystals Using Ground-State Charge Transfer from Cobaltocene. *Sci. Rep.* **2013,** *3*, 1-8.
17. Wang, C.; Shim, M.; Guyot-Sionnest, P., Electrochromic Nanocrystal Quantum Dots. *Science* **2001,** *291*, 2390-2392.
18. Wehrenberg, B. L.; Guyot-Sionnest, P., Electron and Hole Injection in PbSe Quantum Dot Films. *J. Am. Chem. Soc.* **2003,** *125*, 7806-7807.
19. Yu, D.; Wang, C.; Guyot-Sionnest, P., *n*-Type Conducting CdSe Nanocrystal Solids. *Science* **2003,** *300*, 1277-1280.
20. Shim, M.; Guyot-Sionnest, P., Organic-Capped ZnO nanocrystals: Synthesis and *n*-Type Character. *J. Am. Chem. Soc.* **2001,** *123*, 11651-11654.
21. Rinehart, J. D.; Schimpf, A. M.; Weaver, A. L.; Cohn, A. W.; Gamelin, D. R., Photochemical Electronic Doping of Colloidal CdSe Nanocrystals. *J. Am. Chem. Soc.* **2013,** *135*, 18782-18785.
22. Schimpf, A. M.; Gunthardt, C. E.; Rinehart, J. D.; Mayer, J. M.; Gamelin, D. R., Controlling Carrier Densities in Photochemically Reduced Colloidal ZnO Nanocrystals: Size Dependence and Role of the Hole Quencher. *J. Am. Chem. Soc.* **2013,** *135*, 16569-16577.
23. Haase, M.; Weller, H.; Henglein, A., Photochemistry and Radiation Chemistry of Colloidal Semiconductors. 23. Electron Storage on Zinc Oxide Particles and Size Quantization. *J. Phys. Chem.* **1988,** *92*, 482-487.
24. Rivest, J. B.; Jain, P. K., Cation Exchange on the Nanoscale: An Emerging Technique for New Material Synthesis, Device Fabrication, and Chemical Sensing. *Chem. Soc. Rev.* **2013,** *42*, 89-96.
25. Vlaskin, V. A.; Barrows, C. J.; Erickson, C. S.; Gamelin, D. R., Nanocrystal Diffusion Doping. *J. Am. Chem. Soc.* **2013,** *135*, 14380-14389.
26. Beberwyck, B. J.; Surendranath, Y.; Alivisatos, A. P., Cation Exchange: A Versatile Tool for Nanomaterials Synthesis. *J. Phys. Chem. C* **2013,** *117*, 19759-19770.
27. De Trizio, L.; Manna, L., Forging Colloidal Nanostructures via Cation Exchange Reactions. *Chem. Rev.* **2016,** *116*, 10852-10887.
28. Comin, A.; Manna, L., New Materials for Tunable Plasmonic Colloidal Nanocrystals. *Chem. Soc. Rev.* **2014,** *43*, 3957-3975.
29. Scotognella, F.; Valle, G.; Srimath Kandada, A.; Zavelani-Rossi, M.; Longhi, S.; Lanzani, G.; Tassone, F., Plasmonics in Heavily-Doped Semiconductor Nanocrystals. *Eur. Phys. J. B* **2013,** *86*, 1-13.
30. Kriegel, I.; Scotognella, F.; Manna, L., Plasmonic Doped Semiconductor Nanocrystals: Properties, Fabrication, Applications and Perspectives. *Phys. Rep.* **2017,** *674*, 1-52.
31. Schimpf, A. M.; Thakkar, N.; Gunthardt, C. E.; Masiello, D. J.; Gamelin, D. R., Charge-Tunable Quantum Plasmons in Colloidal Semiconductor Nanocrystals. *ACS Nano* **2014,** *8*, 1065-1072.

32. Schimpf, A. M.; Ochsenbein, S. T.; Buonsanti, R.; Milliron, D. J.; Gamelin, D. R., Comparison of Extra Electrons in Colloidal *n*-Type Al^{3+}-Doped and Photochemically Reduced ZnO Nanocrystals. *Chem. Commun.* **2012,** *48*, 9352-9354.
33. Wang, T.; Radovanovic, P. V., Free Electron Concentration in Colloidal Indium Tin Oxide Nanocrystals Determined by Their Size and Structure. *J. Phys. Chem. C* **2011,** *115*, 406-413.
34. Mendelsberg, R. J.; Garcia, G.; Li, H.; Manna, L.; Milliron, D. J., Understanding the Plasmon Resonance in Ensembles of Degenerately Doped Semiconductor Nanocrystals. *J. Phys. Chem. C* **2012,** *116*, 12226-12231.
35. Crockett, B. M.; Jansons, A. W.; Koskela, K. M.; Johnson, D. W.; Hutchison, J. E., Radial Dopant Placement for Tuning Plasmonic Properties in Metal Oxide Nanocrystals. *ACS Nano* **2017,** *11*, 7719-7728.
36. Schimpf, A. M.; Runnerstrom, E. L.; Lounis, S. D.; Milliron, D. J.; Gamelin, D. R., Redox Energies and Plasmon Resonance Energies of Photodoped In_2O_3 and Sn-doped In_2O_3 Nanocrystals. *J. Am. Chem. Soc.* **2015,** *137*, 518-524.
37. Carroll, G. M.; Schimpf, A. M.; Tsui, E. Y.; Gamelin, D. R., Redox Potentials of Colloidal *n*-Type ZnO Nanocrystals: Effects of Confinement, Electron Density, and Fermi-Level Pinning by Aldehyde Hydrogenation. *J. Am. Chem. Soc.* **2015,** *137*, 11163-11169.
38. Brozek, C. K.; Hartstein, K. H.; Gamelin, D. R., Potentiometric Titrations for Measuring the Capacitance of Colloidal Photodoped ZnO Nanocrystals. *J. Am. Chem. Soc.* **2016,** *138*, 10605-10610.
39. Liu, H.; Brozek, C. K.; Sun, S.; Lingerfelt, D. B.; Gamelin, D. R.; Li, X., A Hybrid Quantum-Classical Model of Electrostatics in Multiply Charged Quantum Dots. *J. Phys. Chem. C* **2017,** *121*, 26086-26095.
40. Tsui, E. Y.; Hartstein, K. H.; Gamelin, D. R., Selenium Redox Reactivity on Colloidal CdSe Quantum Dot Surfaces. *J. Am. Chem. Soc.* **2016,** *138*, 11105-11108.
41. Tsui, E. Y.; Carroll, G. M.; Miller, B.; Marchioro, A.; Gamelin, D. R., Extremely Slow Spontaneous Electron Trapping in Photodoped *n*-Type CdSe Nanocrystals. *Chem. Mater.* **2017,** *29*, 3754-3762.
42. Shimizu, K. T.; Neuhauser, R. G.; Leatherdale, C. A.; Empedocles, S. A.; Woo, W. K.; Bawendi, M. G., Blinking Statistics in Single Semiconductor Nanocrystal Quantum Dots. *Phys. Rev. B* **2001,** *63*, 205316.
43. Pelton, M.; Smith, G.; Scherer, N. F.; Marcus, R. A., Evidence for a Diffusion-Controlled Mechanism for Fluorescence Blinking of Colloidal Quantum Dots. *Proc. Natl. Acad. Sci.* **2007,** *104*, 14249.
44. Tang, J.; Marcus, R. A., Mechanisms of Fluorescence Blinking in Semiconductor Nanocrystal Quantum Dots. *J. Chem. Phys.* **2005,** *123*, 054704.
45. Carroll, G. M.; Tsui, E. Y.; Brozek, C. K.; Gamelin, D. R., Spectroelectrochemical Measurement of Surface Electrostatic Contributions to Colloidal CdSe Nanocrystal Redox Potentials. *Chem. Mater.* **2016,** *28*, 7912-7918.
46. Araujo, J.; Brozek, C. K.; Kroupa, D. M.; Gamelin, D. R., Degenerately *n*-Doped Colloidal PbSe Quantum Dots: Band Assignments and Electrostatic Effects. *Submitted* **2018**.
47. Hartstein, K. H.; Erickson, C. S.; Tsui, E. Y.; Marchioro, A.; Gamelin, D. R., Electron Stability and Negative-Tetron Luminescence in Free-Standing Colloidal *n*-Type CdSe/CdS Quantum Dots. *ACS Nano* **2017,** *11*, 10430-10438.

48. Jha, P. P.; Guyot-Sionnest, P., Photoluminescence Switching of Charged Quantum Dot Films. *J. Phys. Chem. C* **2007,** *111*, 15440-15445.

Chapter 2: Electron Stability and Negative-Tetron Luminescence in Free-Standing Colloidal *n*-Type CdSe/CdS Quantum Dots

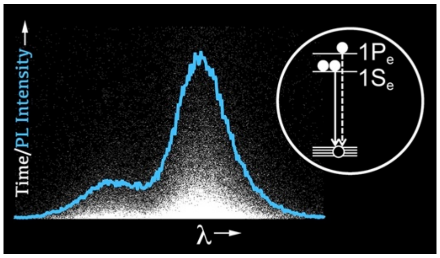

Reproduced with permission from:
Hartstein, K. H.; Erickson, C. S.; Tsui, E. Y.;
Marchioro, A.; Gamelin, D. R. *ACS Nano*
2017, *11*, 10430–10438.

2.1 Overview

We examine the effects of CdS shell growth on photochemical reduction of colloidal CdSe quantum dots (QDs) and describe the spectroscopic properties of the resulting *n*-type CdSe/CdS QDs. CdS shell growth greatly slows electron trapping. Because of this improvement, complete two-electron occupancy of the $1S_e$ conduction-band orbital is achieved in CdSe/CdS QDs and found to be much more stable than in past experiments. Simultaneous photoluminescence at two different energies is now observed from QDs possessing two excess conduction-band electrons, reflecting competing recombination of discretized $1S_e$ and $1P_e$ conduction-band electrons within photogenerated four-carrier negative tetrons (three electrons and one hole). Stable occupancy of the $1P_e$ level is not achievable under these conditions, and possible reasons are discussed. The stability and accessibility of these multi-electron configurations, and the facile spectroscopic detection of negative tetrons, both make photodoped core/shell QDs attractive for exploring the physical properties of free-standing heavily *n*-doped colloidal CdSe-based QDs.

2.2 Introduction

A fundamental understanding of the electronic structures of colloidal semiconductor quantum dots (QDs) is vital to the application of this class of materials in future technologies. Attractive due to their size-tunable physical properties and solution processability, free-standing colloidal

QDs suffer from surface defects that have presented long-standing barriers to many practical applications by limiting luminescence quantum yields, affecting Fermi levels, and ultimately impacting performance in various QD-based devices. Surface modification is commonly employed to mitigate the influence of surface traps, most often in the form of passivating small-molecule surface ligation or shell overgrowth. Through judicious selection of the core and shell parameters, the latter can also be used to strategically tune the material's electronic structure for enhancement of target functional properties. For example, the CdSe/CdS core/shell heterostructure has long attracted interest because of its quasi-type II band alignment, in which conduction-band electrons (e^-_{CB}) delocalize throughout the heterostructure but valence-band holes (h^+_{VB}) localize at the CdSe core.[1-10] This spatial separation of charge carriers prolongs exciton radiative lifetimes, slows Auger recombination, enhances photocatalysis, suppresses luminescence intermittency ("blinking"), and eliminates some non-radiative surface-recombination pathways.

Electronic doping is a powerful approach for studying the electronic structures of semiconductor nanocrystals.[11] Among the various methods for introducing excess delocalized charge carriers, photodoping has proven particularly useful for achieving reversible and quantifiable tuning of electron occupancies in free-standing oxide and chalcogenide QDs.[11-21] Here, we use photodoping to incorporate excess e^-_{CB} into colloidal CdSe/CdS core/shell QDs with various shell thicknesses. We show that the excess conduction-band electrons become increasingly stable at room temperature with increasing CdS shell thickness. This stability allows detailed chemical and spectroscopic characterization of the resulting *n*-doped core/shell QDs in the absence of electrodes, excess reductant, or other potential perturbations. In QDs containing two extra e^-_{CB}, we observe separate photoluminescence (PL) bands from recombination of discretized $1S_e$ and $1P_e$ electrons, as well as corresponding dynamic signatures of four-carrier negative tetrons (three e_{CB}^- and one h_{VB}^+). Discrete $1S_e$ and $1P_e$ PL bands have been observed in other CdSe-based QDs under electrochemical bias,[22,23] and the dynamics of negative tetrons have been described for CdSe/CdS QDs.[21,24] Here, we quantify these two phenomena together in conjunction with chemical titration analysis of the extent of *n*-doping to demonstrate the relationship between them. The findings presented here improve our understanding of electronic materials relevant to various QD optoelectronic technologies and point to the use of photodoped *n*-type CdSe/CdS core/shell QDs for future fundamental electronic-structure studies of multi-electron QDs.

2.3 Results & analysis

2.3.1 Photodoping, electron stability, and electron titration. Figure 2.1 shows TEM images of a representative series of CdSe/*x*CdS core/shell QDs prepared from the same CdSe cores but with different CdS shell thicknesses of x = 2, 4, and 7 monolayers. The average QD diameter increases with increasing shell thickness, as does the nanocrystal faceting, and a small increase in the size distribution is also observed.

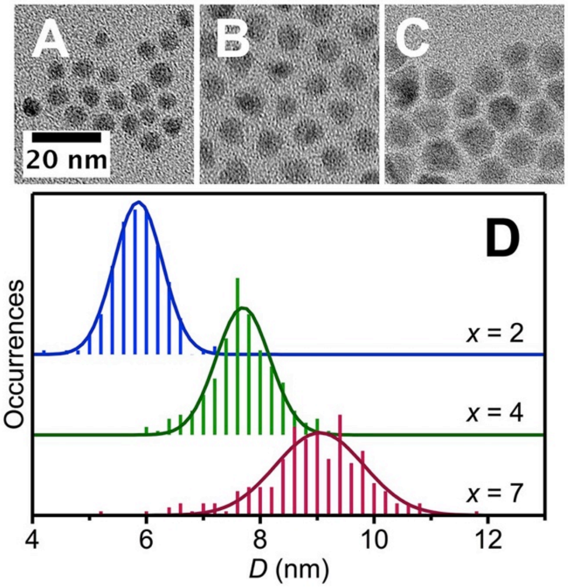

Figure 2.1. (**A**,**B**,**C**) TEM images of representative CdSe/*x*CdS QDs with $x = 2, 4$, and 7, respectively, grown on $d = 4.3$ nm CdSe cores. (**D**) Size histograms for each core/shell sample, based on analysis of more than 200 QDs each. The reported numbers of CdS shell monolayers (x) are calculated from the average TEM diameters by assuming each monolayer has a thickness of 0.35 nm.[25]

Core/shell QDs were reduced photochemically following the approach described in detail previously,[13,18] in which Li[BEt$_3$H] pre-reduces the QD surfaces followed by photoexcitation and hole capture. Figure 2.2 plots normalized absorption and continuous-wave photoluminescence (CW PL) spectra of as-prepared (solid) and maximally photodoped (dashed) CdSe/*x*CdS QDs with increasing shell thickness (top to bottom). The combination of large valence-band offset and small conduction-band offset between CdSe and CdS leaves holes largely confined to the CdSe volumes but permits delocalization of electrons throughout the entire heterostructure volumes,[26] resulting in a redshift in absorption and PL energies of the as-prepared QDs with increasing CdS shell thickness. The PL quantum yield (QY) of the as-prepared QDs also increases, from ~3% at $x = 0$ to ~73% at $x = 7$. Resonant photoexcitation of the CdSe feature still leads to photodoping (see Appendix A), demonstrating hole capture at the surface despite confinement to the CdSe core.

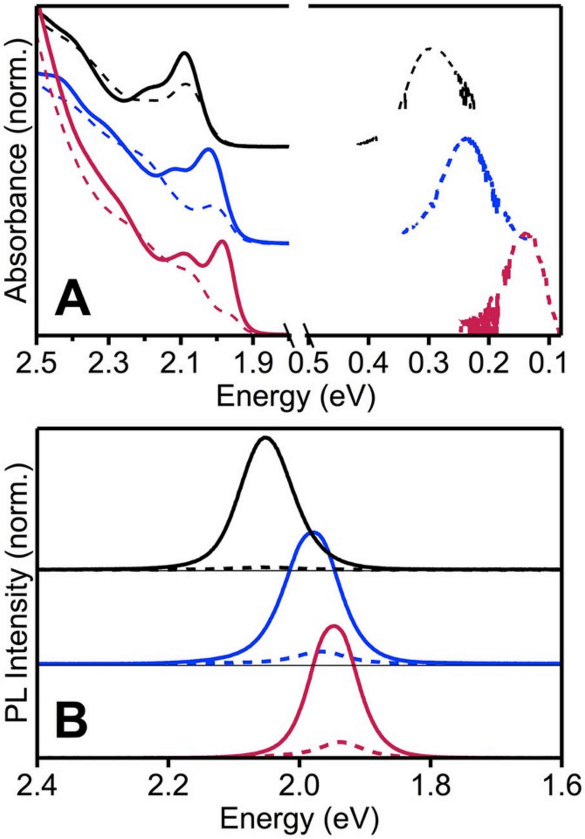

Figure 2.2. (**A**) Visible and infrared ($1S_e$-$1P_e$) electronic absorption and (**B**) visible CW PL spectra of as-prepared (solid) and maximally photodoped (dashed) CdSe/*x*CdS QDs with x = 0, 2, and 7 monolayers of CdS shell (from top to bottom) deposited on d = 4.3 nm CdSe QD cores. Major solvent peaks have been removed from the IR spectra for clarity. With increasing shell thickness, $\langle n_{\mathrm{max}} \rangle$ increases. CW PL intensity is still observed at $\langle n_{\mathrm{max}} \rangle$ for the shelled samples.

Concomitant with these changes, the maximum extent of photodoping that can be achieved also increases with increasing shell thickness, as gauged by the bleach of the first excitonic absorption peak ($1S_h$-$1S_e$). In the core CdSe QDs (x = 0), this absorbance is reduced by only ~35% before further photoexcitation no longer generates additional $1S_h$-$1S_e$ bleach, whereas in the largest CdSe/CdS QDs (x = 7), the first exciton is bleached by ~90% at maximum photodoping. The average number of excess e^-_{CB} per QD ($\langle n \rangle$) can be quantified by analyzing the extent of this bleach using the relationship $\langle n \rangle = |(2\Delta A/A_0)|$.[13,16,18,20] At maximum photodoping, we define $\langle n \rangle = \langle n_{\mathrm{max}} \rangle$. The CdSe QD cores without any shell reach only $\langle n_{\mathrm{max}} \rangle \sim 0.7$, but depositing just two monolayers of CdS shell increases $\langle n_{\mathrm{max}} \rangle$ to 1.6, and at 7 shell monolayers $\langle n_{\mathrm{max}} \rangle = 1.8$. We have previously shown that $\langle n_{\mathrm{max}} \rangle$ in CdSe QDs reflects the steady-state balance between photoreduction and electron trapping, and that increases in $\langle n_{\mathrm{max}} \rangle$ correlate with stabilization of the CB-edge potential to reduce the number of mid-gap electron traps.[20,27] We have also shown that even though mid-gap electron traps below the Fermi level are filled by photodoping, new mid-gap traps appear spontaneously on long time scales because of trap-state fluctuations.[20] Following these observations, the trend of increasing $\langle n_{\mathrm{max}} \rangle$ with CdS shell growth is attributed to: (1) reduction of the number of mid-gap surface electron traps through physical passivation, and (2) shifting of the conduction-band edge to more positive redox potentials relative to the electron-trap-state distribution through relaxation of electron quantum confinement.[20] With these two effects, e^-_{CB} have access to fewer mid-gap surface traps after CdS shell growth, leading to lower electron-trapping rates (*vide infra*) and hence greater values of $\langle n_{\mathrm{max}} \rangle$.

In the unshelled ($x = 0$) CdSe QDs, the CW PL is almost completely quenched at $\langle n_{\mathrm{max}} \rangle$ due to efficient Auger recombination. Statistically, each thin-shelled ($x = 2$) CdSe/CdS QD contains at least one e^-_{CB} at $\langle n_{\mathrm{max}} \rangle \sim 1.6$, and yet considerable PL intensity remains. The thick-shelled ($x = 7$) QDs also still luminesce even at $\langle n_{\mathrm{max}} \rangle \sim 1.8$. The remaining CW PL intensity is attributed to the reduced non-radiative Auger decay rate of negative trions in these QDs, due to the combination of relaxed quantum confinement[14] and increased spatial separation between charge carriers[8] with increasing CdS shell thickness.

The fluctuations described above cause new mid-gap electron traps to appear spontaneously over very long time scales, causing slow electron trapping even under rigorously anaerobic conditions.[18,20] This slow trapping is manifested as an extremely slow recovery of excitonic absorption after photodoping.[20] Detailed studies have demonstrated that this trapping follows unimolecular reaction kinetics and hence cannot be attributed to the trivial scenario of diffusive oxidants in solution.[20] Figure 2.3 summarizes the slow anaerobic absorption recovery observed for photodoped CdSe/xCdS QDs (x = 2, 4, 7). The data are plotted as the normalized first-excitonic absorption bleach ($-\Delta A/A_0$) *vs* time. Fitting these data yields the electron decay time constants (τ_D) plotted in the inset of Figure 2.3. These data show that increasing the CdS shell thickness reduces the rate of electron trapping markedly. For example, $\tau_D \sim 15$ min when $x = 2$, but increases to several hours for $x = 7$. Photodoped CdSe/7CdS QDs are thus remarkably stable as free-standing colloidal *n*-type nanocrystals.

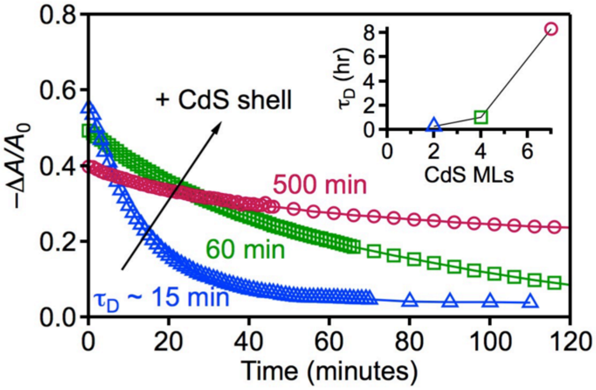

Figure 2.3. Anaerobic e^-_{CB} decay kinetics for CdSe/*x*CdS QDs with $x = 2$ (**Δ**), 4 (□), and 7 (**O**) monolayers, measured in solution at room temperature. The data points represent the normalized absorption at the maximum of the first excitonic absorption transition ($1S_h$-$1S_e$) for each sample. The solid lines show exponential fits to the data, which yield the electron decay time constants (τ_D) shown. Because the history of the QDs can affect the electron trapping rates,[20] these samples were prepared and handled under identical conditions for these measurements (see Experimental Methods). The small differences in $\langle n \rangle$ at $t = 0$ reflect sample handling and do not impact the primary conclusions drawn from these data. Inset: Plot of τ_D *vs* CdS shell thickness.

The high stability of these excess conduction-band electrons enables the use of chemical titration as an independent measure of $\langle n \rangle$.[13] Previous attempts to titrate large ($d = 7.0$ nm), maximally photodoped CdSe QDs were complicated by the presence of additional trapped electrons, presumably at surface sites.[13] Figure 2.4 shows electronic absorption spectra of maximally photodoped CdSe/7CdS QDs collected during titration with the outer-sphere chemical oxidant, $[FeCp^*_2][BAr^F_4]$. With each aliquot of oxidant, the absorption recovers partially. The inset plots $-\Delta A/A_0$ *vs* added equivalents of $[FeCp^*_2]^+$ and reveals a linear dependence of the absorption recovery on added oxidant. The intercept of these data with the *x* axis indicates $\langle n \rangle \sim 2$. This result is consistent with the spectroscopic estimate of $\langle n \rangle = 1.8$ for the same sample. The linearity of these titration data shows that all titratable electrons contribute equally to the absorption bleach, within experimental uncertainty. These data show that few if any electrons reside on the surfaces of these CdSe/7CdS QDs, consistent with nearly complete elimination of mid-gap electron traps as discussed above.

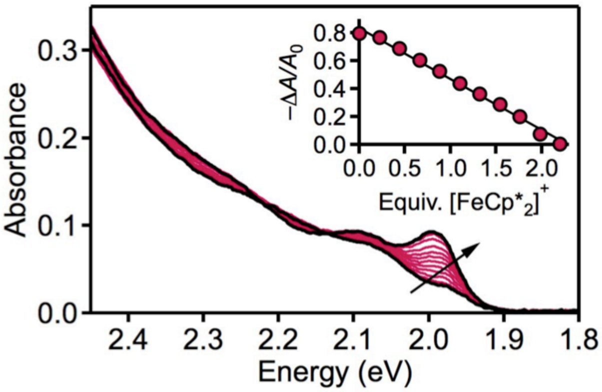

Figure 2.4. Absorption spectra of maximally photodoped CdSe/7CdS QDs collected during titration with [FeCp$^*_2$][BAr$^F_4$]. Inset: Normalized absorption bleach at the first excitonic maximum *vs* added [FeCp$^*_2$]$^+$ equivalents. The titration demonstrates that the maximally photodoped QDs contain an average of $\langle n \rangle \sim 2$.

2.3.2 Negative-tetron luminescence. Figure 2.5 shows a more detailed view of the absorption and PL changes that accompany photodoping of one representative sample of CdSe/2CdS QDs. Spectra are plotted for these QDs photodoped to $\langle n \rangle$ = 0.0, 0.4, and 1.6. In addition to the increasing bleach of the $1S_e$-$1S_h$ absorption feature with increasing $\langle n \rangle$, the main PL peak (ascribed to radiative $1S_e$-$1S_h$ recombination) red-shifts with photodoping, *e.g.*, by ~5 meV at $\langle n \rangle$ = 0.4, consistent with emission contributions from negative trions.[28] At a value of $\langle n \rangle$ = 1.6, this main feature has shifted by ~25 meV, and a second higher-energy PL band appears. This additional PL feature has been observed in CdSe and CdSe/CdS QD films held under an applied potential, and was assigned to emission involving higher-energy $1P_e$ electrons.[22,23]

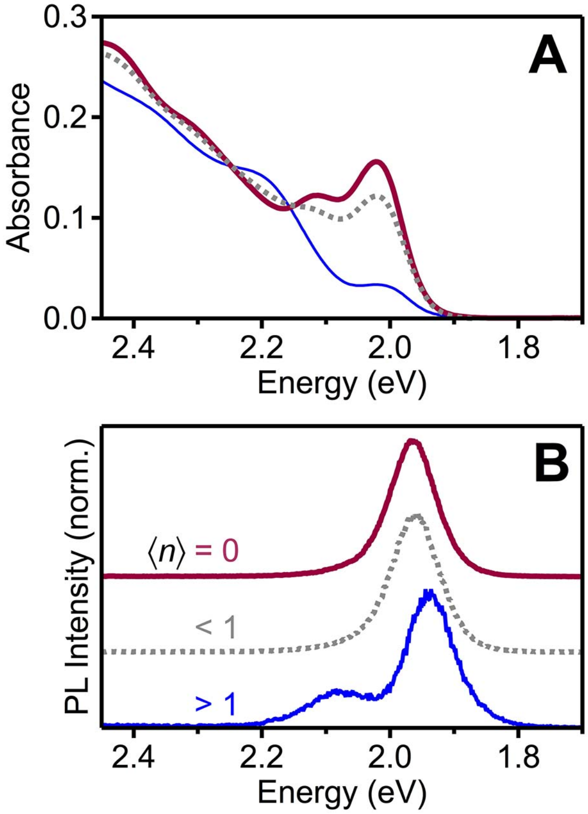

Figure 2.5. (**A**) Absorption of CdSe/2CdS QDs measured at $\langle n \rangle = 0$ (thick solid), $\langle n \rangle = 0.4$ (dashed) and $\langle n_{\text{max}} \rangle = 1.6$ (thin solid). (**B**) PL spectra of the samples from panel A. At $\langle n \rangle > 1$, a second higher energy PL peak is observed.

Figure 2.6A plots PL spectra for a series of CdSe/xCdS QDs ($x = 0, 2, 7$) collected after photodoping to $\langle n_{\text{max}} \rangle$ in each case. All three spectra show evidence of an upper PL band. $\langle n_{\text{max}} \rangle$ is only 0.7 for the $x = 0$ sample, so the $1P_e$ orbital is essentially unoccupied at steady state (see Appendix A). Moreover, these unshelled CdSe QDs exhibit negligible CW PL at $\langle n_{\text{max}} \rangle$ (Figure 2.2). Nonetheless, their PL spectrum can be obtained by integrating just the first 800 ps of their time-resolved PL, and a small higher-energy PL band is then observed. PL spectra of the CdSe/2CdS QDs were discussed in Figure 2.5 and show a well-resolved higher-energy band at high photodoping levels. For the CdSe/7CdS QDs, the PL is much stronger and the upper PL band is again observed. In this sample, the two bands are closer in energy because of relaxed quantum confinement, and they partially overlap.

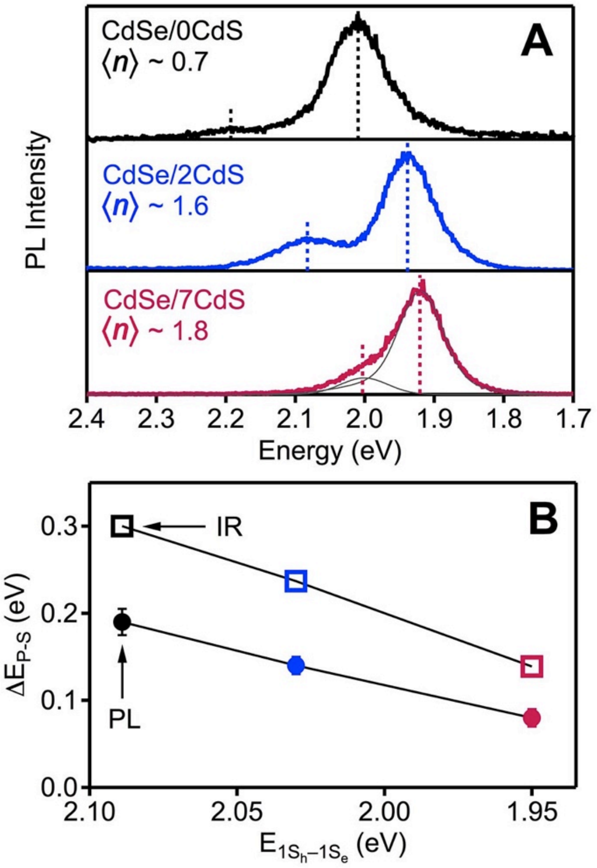

Figure 2.6. (**A**) PL spectra for maximally photodoped CdSe/*x*CdS QDs, where *x* = 0, 2, and 7 monolayers. Values of $\langle n \rangle$ are indicated on each spectrum. The dotted lines indicate the $1S_e$ and $1P_e$ emission energies in each spectrum. (**B**) ΔE_{P-S} values determined from IR intraband absorption (Figure 2.2A) and visible PL (panel A of this figure), plotted *vs* the energy of the first excitonic absorption feature ($E_{1S_h-1S_e}$). ΔE_{P-S}(IR) and ΔE_{P-S}(PL) both decrease with decreasing quantum confinement, and the difference between the two reflects the additional Coulomb interactions probed by the PL measurement. Error bars on ΔE_{P-S}(PL) values reflect estimated uncertainties from the peak fitting. ΔE_{P-S}(IR) error bars are smaller than the data points themselves.

Figure 2.6B plots the energy difference between the two PL peaks in Figure 2.6A (ΔE_{P-S}(PL)) *vs* the energy of the first excitonic absorption maximum ($E_{1S_h-1S_e}$) for these three samples, along with the energy difference between $1S_e$ and $1P_e$ one-electron states within the conduction band, as probed by intra-band absorption in the infrared ($\Delta E_{P\text{-}S}$(IR), Figure 2.2A). Both energies decrease with decreasing electron confinement upon increasing the CdS shell thickness, but $\Delta E_{P\text{-}S}$(PL) is consistently smaller than $\Delta E_{P\text{-}S}$(IR). The difference between $\Delta E_{P\text{-}S}$(PL) and $\Delta E_{P\text{-}S}$(IR) reflects the additional Coulomb interactions present in the initial and final states of the luminescence transitions that are not present in the IR excited states. This correlation thus supports the assignment of this upper PL band to recombination involving $1P_e$ electrons in QDs containing multiple excess conduction-band electrons. We note that although the trend in Figure 2.3 would suggest even greater e^-_{CB} stability with increasing CdS shell thickness, the data in Figure 2.6 show that the upper PL band becomes increasingly obscured by the lower PL band with increasing CdS shell thickness. For this reason, CdSe/*x*CdS QDs with even thicker CdS shells than $x = 7$ were not explored in this study.

Figure 2.7A shows a streak-camera image describing the PL decay dynamics of the CdSe/2CdS QDs from Figure 2.5 possessing $\langle n \rangle = \langle n_{\text{max}} \rangle = 1.6$. The integrated $1S_e$ and $1P_e$ PL intensities are plotted *vs* time in Figure 2.7B. Although similar, the decay dynamics for the two features do differ slightly. This difference is attributable to the presence of discrete subsets of QDs with $n = 1$ and $n = 2$ within this $\langle n \rangle = 1.6$ ensemble. Nonetheless, these results confirm that both luminescence features seen in Figure 2.5B ($\langle n \rangle = 1.6$) derive from the same excited state.

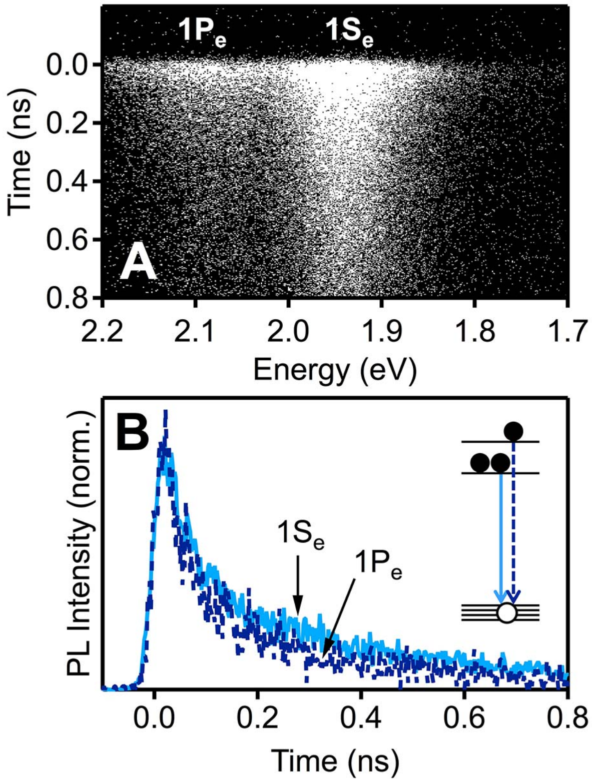

Figure 2.7. (A) Time-resolved PL streak image maximally-photodoped ($\langle n \rangle$ = 1.6) CdSe/2CdS QDs (λ_{exc} = 405 nm, E_{exc} = 3.06 eV). **(B)** Decay dynamics for $1S_e$ (solid, integrated from 1.92-1.95 eV) and $1P_e$ (dashed, 2.07-2.12 eV) electrons in CdSe/2CdS, highlighting their very similar kinetics.

To explore the emission of these heavily *n*-doped QDs more systematically, we measured room-temperature PL decay dynamics of the CdSe/7CdS QDs at various values of $\langle n \rangle$. Figure 2.8 plots absorption spectra and PL decay curves of these CdSe/7CdS QDs poised at $\langle n \rangle = 0, 0.5$, and 1.8. The as-prepared QDs ($\langle n \rangle$ = 0) exhibit purely excitonic emission and their PL decay can be fit to a single exponential with a time constant τ_X = 35 ns (see Appendix A for complete fit). When *n*-type carriers are introduced, PL is enhanced at short times due to the greater radiative rate of the negative trion. Faster decay of the PL is also observed, consistent with a combination of this increased radiative rate and the introduction of non-radiative trion Auger recombination. At $\langle n \rangle$ = 0.5, the PL decay is biexponential, reflecting a superposition of negative trion recombination (τ_{X^-} = 2.6 ns) and neutral exciton recombination (τ_X) from the presence of both *n*-doped and undoped QDs in this ensemble. The value of τ_{X^-} = 2.6 ns is consistent with that predicted from the reported size dependence of τ_{X^-} in photodoped *n*-type CdSe QDs[14] using the *effective* QD diameter, as determined by the energy of the first excitonic absorption feature (see Appendix A).

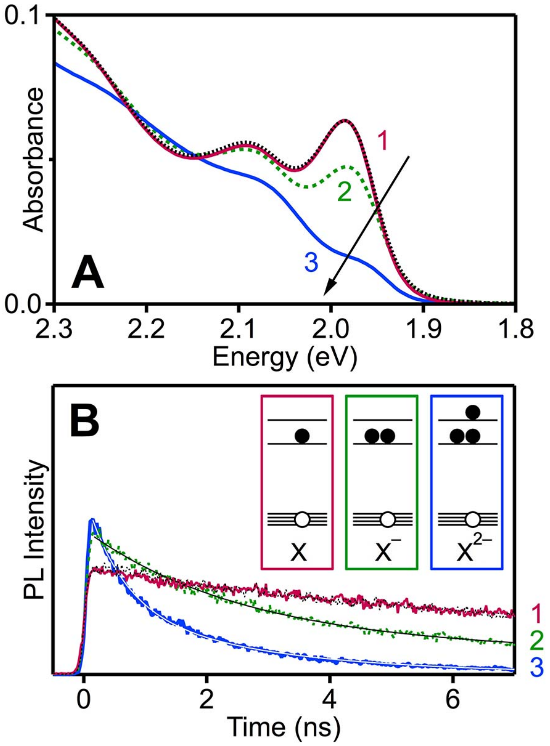

Figure 2.8. (**A**) Absorption spectra collected at three stages of photodoping for CdSe/7CdS QDs: (1) $\langle n \rangle = 0$, (2) $\langle n \rangle = 0.5$, and (3) $\langle n \rangle = 1.8$. The black dotted trace shows the spectrum collected after QD reoxidation to $\langle n \rangle = 0$ and is indistinguishable from the initial trace, demonstrating complete sample recovery. (**B**) PL decay curves corresponding to (1), (2), and (3) from panel A (λ_{exc} = 405 nm, 3.06 eV). The amplitude of the reoxidized curve (dotted) has been reduced (×0.84) for clarity to account for mild sample brightening upon reoxidation. Thin solid traces illustrate biexponential fits for $\langle n \rangle > 0$ as described in the main text. Inset: Schematics illustrating the three relevant multicarrier configurations observed in panels A and B: neutral exciton, negative trion, and negative tetron (from left to right).

The PL decay is also biexponential at $\langle n \rangle = 1.8$. Here, neutral exciton emission is completely absent because every QD possesses at least one excess e_{CB}^{-}. Negative trion decay (with τ_{X^-}) is still observed, and in addition a faster process is observed with a decay constant of $\tau \approx 600$ ps, or roughly $\frac{1}{4}\tau_{\mathrm{X}^-}$. This faster component is interpreted as reflecting PL from QDs with $\langle n \rangle = 2$ that have been photoexcited, thus containing four band-like charge carriers (three e_{CB}^{-} and one h_{VB}^{+}) in their luminescent excited state, *i.e.*, a negative tetron (X^{2-}). The inset to Figure 2.8 illustrates carrier configurations relevant to each of the traces in panels A and B. Trace 1 includes only neutral excitons (X), trace 2 includes X and negative trions (X^-), and trace 3 includes X^- and X^{2-}. Upon reoxidation by air, both the absorption spectrum and PL dynamics return to their original values, being indistinguishable from those of the as-prepared QDs prior to photodoping. A small (~19% relative) enhancement in overall PL quantum yield is observed after reoxidation, attributed to surface restructuring induced by this reduction/oxidation cycle.

Figure 2.9 summarizes these findings. Figure 2.9A plots the fractional contributions from each of the carrier configurations to the PL dynamics *vs* $\langle n \rangle$ for the same CdSe/7CdS QDs, deduced from global fitting of a more extensive series of PL decay curves (see Appendix A and Experimental methods). As described above, at values of $\langle n \rangle = 0$, the PL is entirely attributable to neutral X. In the regime $0 < \langle n \rangle < 1$, the decay is biexponential with components corresponding to τ_{X} and τ_{X^-}. At $\langle n \rangle > 1$, a third component ($\tau_{\mathrm{X}^{2-}}$) is introduced.

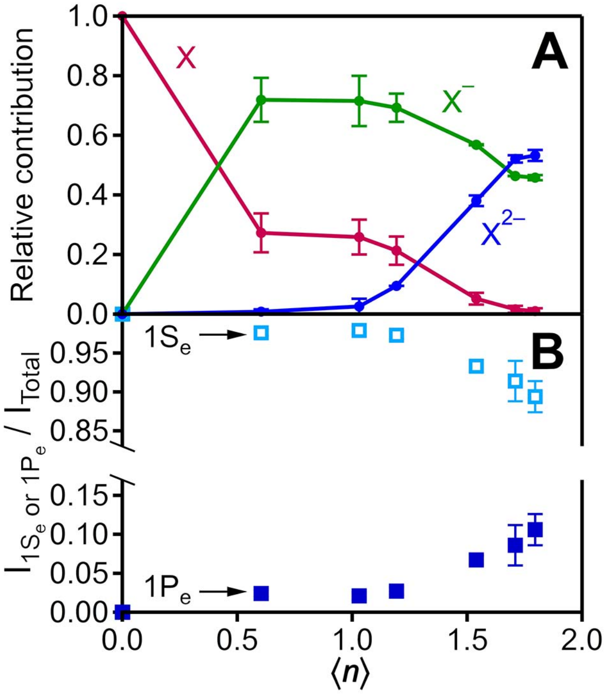

Figure 2.9. (**A**) Relative amplitudes of PL decay components arising from neutral excitons (X), negative trions (X^{-}), and negative tetrons (X^{2-}) in *n*-doped CdSe/7CdS QDs plotted *vs* $\langle n \rangle$, obtained from fitting of PL decay curves collected for each value of $\langle n \rangle$. (**B**) Intensities of PL peaks assigned to recombination of discrete $1S_e$ and $1P_e$ electrons in *n*-doped CdSe/7CdS QDs plotted *vs* $\langle n \rangle$, determined by analysis of PL spectra collected for each value of $\langle n \rangle$ (see Experimental methods and Appendix A for details).

Similarly, Figure 2.9B plots the fractional $1S_e$ and $1P_e$ emission intensities *vs* $\langle n \rangle$ extracted from PL spectral fitting (see Appendix A). At $\langle n \rangle < 1$, the $1P_e$ emission is absent within experimental uncertainty, but when $\langle n \rangle > 1$, the $1P_e$ emission appears and increases in intensity. The relative intensity from the $1S_e$ emission is inversely correlated with that from the $1P_e$ emission, decreasing only at $\langle n \rangle > 1$. Overall, the PL QY decreases with increasing $\langle n \rangle$ (see Appedix A). The $1S_e$ data plotted in Figure 2.9B compare well to the sum of X and X^{-} decay amplitudes plotted in Figure 2.9A, whereas the $1P_e$ data in Figure 2.9B show the same trend as seen for the X^{2-} decay amplitudes in Figure 2.9A.

The data in Figure 2.9 show that tetron luminescence, which can only appear when $n = 2$ in a given QD prior to photoexcitation, turns on rather abruptly at $\langle n \rangle > 1$. Our prior studies have demonstrated diffusion-limited inter-QD electron transfer following such photodoping.[16,29,30] Because of this rapid electron transfer, there is Fermi level equilibration within the ensemble of QDs such that the electron distributions among QDs are not determined by Poissonian photoexcitation statistics but rather by $\langle n \rangle$ and the ensemble's distributions in QD band-edge potentials and multi-electron configurational energies. The abrupt appearance of tetron luminescence at $\langle n \rangle > 1$ in Figure 2.9 thus reflects the tendency of the added electrons to distribute rather evenly across the ensemble of QDs, regardless of where they were initially generated.

From these PL decay dynamics, it is also possible to estimate radiative rate constants (k_r), non-radiative Auger rate constants (k_A), and PL quantum yields (QY) for the X, X^-, and X^{2-} electronic configurations of these QDs. Following prior analysis of multistate blinking in CdSe/CdS QDs, these parameters can be quantified using equations 2.1–2.3.[8,24] Here, β is a carrier overlap factor that relates the radiative recombination rate of a charged exciton to that of the neutral exciton, and i denotes the carrier configuration. Table 2.1 summarizes the values of these quantities determined from the dynamics measured for the CdSe/7CdS QDs (Figure 2.8 and Appendix A). Statistically, $\tau_A^{X^{2-}}$ should decay 3× faster than $\tau_A^{X^-}$ because of the increased number of possible recombination pairings, consistent with the factor of ~4 measured experimentally. Different radiative and non-radiative transition probabilities can be anticipated for recombination involving $1S_e$ and $1P_e$ electrons, which will cause deviations from simple statistics. The values in Table 2.1 were obtained by using the integrated PL decay curves to estimate QYs at different values of $\langle n \rangle$ relative to the QY at $\langle n \rangle = 0$, which was measured independently using an integrating sphere (see Appendix A).

$$k_{\mathrm{r}}^{i} = \beta^{i} k^{\mathrm{X}} \tag{2.1}$$

$$k^{i} = k_{\mathrm{r}}^{i} + k_{\mathrm{A}}^{i} = 1/\tau_{i} \tag{2.2}$$

$$\mathrm{QY}^{i} = \frac{k_{\mathrm{r}}^{i}}{k_{\mathrm{r}}^{i} + k_{\mathrm{A}}^{i}} \tag{2.3}$$

Table 2.1. Recombination parameters determined for various neutral and charged excitonic excited states of CdSe/7CdS QDs.

i	QY	τ_i (ns)	$1/k^{i}_{\mathrm{r}}$ (ns)	$1/k^{i}_{\mathrm{A}}$ (ns)	β^i
X	0.73[a]	35	35	–	1
X^-	0.11	2.6	23.6	2.9	1.48
X^{2-}	0.06	0.6	10	0.6	3.5

[a] Measured independently using an integrating sphere.

The β values determined here yield information about the Coulomb forces acting between carriers. The experimental β^{X^-} value is smaller than the statistical expectation ($\beta^{\mathrm{X}^-} = 2$) and it is also smaller than the value observed in CdSe QDs ($\beta^{\mathrm{X}^-} = 2.2$),[31] but it agrees well with the value measured for CdSe/CdS QDs overcoated with silica ($\beta^{\mathrm{X}^-} = 1.49$). This reduced value of β^{X^-} is consistent with diminished carrier overlap in these core/shell QDs because of proper core/shell band alignment for electron but not hole delocalization.[24] The value of $\beta^{\mathrm{X}^{2-}}$ in Table 2.1 is comparable to but slightly larger than that expected purely statistically ($\beta^{\mathrm{X}^{2-}} = 3$).

2.4 Discussion

The results and analysis presented above show that growth of CdS shells around colloidal CdSe QDs markedly improves the stability of excess conduction-band electrons added *via* photodoping. The resulting colloidal *n*-type QDs can be stabilized for hours in solution at room temperature and are thus amenable to investigation by various chemical and spectroscopic methods. Similar to unshelled CdSe QDs,[20] we find that the maximum number of conduction-band electrons that can be added to these core/shell QDs *via* photodoping, $\langle n_{\mathrm{max}} \rangle$, increases with increasing QD diameter across a well-controlled series of related QDs. For the present QDs, we can add as many as 2 excess electrons per QD *via* photodoping, but not more. This maximum is confirmed by direct chemical titration of the excess electrons. This value of $\langle n_{\mathrm{max}} \rangle$ is somewhat larger than we found for unshelled CdSe QDs ($\langle n_{\mathrm{max}} \rangle < \sim 1.6$[17,20]), but not dramatically so. The greatest contrast between shelled and unshelled CdSe QDs is in the long-term stability of these excess electrons.

An interesting question pertains to the precise origin of $\langle n_{\mathrm{max}} \rangle$, which remains unclear. We have previously demonstrated[17,20] that $\langle n_{\mathrm{max}} \rangle$ for (unshelled) CdSe QDs is not related to the specific orbital occupancies of the QDs in any way, because in some cases $\langle n_{\mathrm{max}} \rangle$ occurs at values well below 1, meaning many QDs within the ensemble actually possess no conduction-band electrons at maximum photodoping. Such data suggest an important role of surface traps in determining the most-negative Fermi level achievable during photodoping.[17,20] For the present CdSe/CdS QDs, $\langle n_{\mathrm{max}} \rangle$ reaches nearly 2 with the thickest of our CdS shells ($x = 7$), but we see no evidence for steady state occupancy of the $1P_e$ levels in either the PL spectra or the PL decay data. We hypothesize that such $1P_e$ electrons, which would be at least ~150-300 meV (variable with quantum confinement, Figure 2.2) less stable than the $1S_e$ electrons, trap at much faster rates than the $1S_e$ electrons even in these core/shell heterostructures because of a greater trap density of states at these potentials, and this rapid trapping precludes stable $1P_e$ occupancy. Maximum carrier densities are thus limited to $\langle N \rangle \sim 10^{19}$ cm^{-3} in these CdSe/CdS QDs, compared to an order of magnitude larger carrier densities found for photodoped metal-oxide (ZnO, In_2O_3, and related) nanocrystals.[12,32]

Previously, remote chemical dopants were also found to introduce no more than two excess electrons per QD into CdSe QDs.[13] Interestingly, even when electrons are introduced electrochemically, CdSe QD films still allow only partial filling of the $1P_e$ shell.[33] It is likely that both of these observations also reflect the accessibility of surface electron traps at the fairly negative potentials of the $1P_e$ electrons. During preparation of this manuscript, another study of the same *n*-type photodoping of CdSe/CdS QDs using $LiBEt_3H$ was published in which values as large as $\langle n \rangle = 6$ are reported.[21] It is conceivable that in these QDs the density of surface traps was diminished significantly compared to the other samples discussed above, allowing accumulation of many more electrons per QD before reaching the potentials of these traps. We note, however, that $\langle n \rangle$ values in this study were determined by analysis of the first exciton's absorption bleach under the assumption that distributions of excess electrons among QDs reflect the Poissonian QD photoexcitation statistics, without consideration of subsequent inter-QD electron transfer. Under this assumption, QDs with very large values of *n* coexist with QDs having no excess electrons, and much larger values of $\langle n \rangle$ are thus required to fully bleach the first excitonic absorption feature. Only the $1S_e$ electrons contribute to this bleach. Such a broad Poissonian distribution of electrons among QDs appears inconsistent with our previous observations of rapid inter-QD electron transfer,[16,29,30] the abrupt appearance of tetron PL when increasing from $\langle n \rangle < 1$ to $\langle n \rangle >$

1 (Figure 2.9), and the confirmation by direct chemical titration that a full bleach of the first excitonic absorption feature is achieved at $\langle n \rangle \sim 2$ (Figure 2.4).

More generally, the capability to incorporate multiple, robust *n*-type carriers into high-optical-quality colloidal CdSe QDs *via* photochemical reduction described here presents exciting opportunities to investigate the various physical properties of these materials containing excess electrons. For example, long-lived spin coherence has been demonstrated in a host of singly reduced semiconductor QDs generated as films on electrode surfaces.[34] In the case of the tetrons described here, the spin configuration reduces to that of a neutral exciton because the excess carriers form a paired singlet with zero spin. These negative tetrons may therefore prove of fundamental interest from the standpoint that the one unpaired electron occupies the $1P_e$ orbital rather than the $1S_e$ orbital, and spin-sensitive techniques such as time-resolved Faraday rotation or magneto-luminescence could thus be used to selectively probe specifically the $1P_e$ electron. Experiments on electrochemically reduced CdSe QDs do demonstrate a convergence of two *g* values in neutral QDs to a single resonance under negative bias,[35] attributed to suppression of excitonic precession and demonstrating feasibility of such measurements on *n*-doped QDs. Stable photodoping may also help advance the understanding of dopant-carrier magnetic-exchange interactions involving impurity spin centers in colloidal CdSe QDs. For example, photodoping of $Zn_{1-x}Mn_xO$ QDs was shown to induce long-range carrier-mediated Mn^{2+}-Mn^{2+} exchange coupling[36] and modify Mn^{2+} spin-relaxation rates.[37] Similar experiments in $Cd_{1-x}Mn_xSe$ QDs could take advantage of the ability to retain excitonic PL in these doped QDs,[38,39] allowing use of PL and magneto-PL to probe such exchange interactions. All of these experiments will benefit from the ability to generate and stabilize excess charge carriers in high-optical-quality *n*-doped CdSe-based QDs.

2.5 Summary & conclusions

Colloidal CdSe/CdS core/shell QDs were photochemically reduced, incorporating up to two conduction-band electrons per QD. The maximum level of *n*-doping was shown to increase as a function of shell thickness, reflecting suppression of surface electron trapping. CdS shelling enhances carrier stability in colloidal CdSe QDs, with excess electrons stable on timescales of hours in solution at room temperature, which in turn enables accurate quantification of the number of excess charge carriers per QD *via* direct chemical titration. Discrete emission bands involving recombination of $1S_e$ and $1P_e$ electrons are observed at values of $\langle n \rangle > 1$, both decaying with similar rate constants, indicating formation of four-carrier negative tetrons. Analysis of the PL decay dynamics confirms this assignment. These results highlight the exceptional control afforded by photodoping for incorporating excess conduction-band electrons into freestanding colloidal CdSe/CdS QDs and suggest opportunities for development of nanomaterials with tailored electronic configurations relevant to future applications in optoelectronics, photoredox chemistry, and other technologies.

2.6 Experimental methods

2.6.1 General considerations. Unless stated otherwise, all syntheses and sample preparations were performed using standard Schlenk techniques under a dinitrogen atmosphere, or in a nitrogen-filled glovebox with anhydrous solvents.

2.6.2 Chemicals. Cadmium oxide (CdO; 99.99+%), 1-octadecene (ODE; 90%), oleic acid (OA; 90%), hexadecylamine (HDA; 90%), trioctylphosphine oxide (TOPO; 99%), selenium metal (Se; 99.99+%), and 1-octanethiol (OT; >98.5%) were purchased from Sigma-Aldrich. Trioctylphosphine (TOP; 97%) was purchased from Strem. All chemicals were used as received.

2.6.3 Quantum dot synthesis. Colloidal CdSe QDs were synthesized using a hot-injection procedure adapted from ref [40]. In a 100-mL 3-neck round bottom flask, a stirred solution of 150 mg of CdO, 12g of ODE, and 1g of OA was degassed under vacuum at 110°C for 1 hour. The solution was then heated to ~280°C under N_2 until the red solution turned clear and colorless. The solution was allowed to cool to 100°C and was then placed under vacuum for 1 hour to remove O_2 produced by forming the $Cd(oleate)_2$. 2g of HDA and 2g of TOPO were then added to the flask under an overpressure of N_2, followed by 30 min of vacuum and 3 purge cycles with N_2. After purging the system, the flask was heated to 300°C under N_2. In a separate 25-mL flask, 190 mg of Se was dissolved in 4 mL of TOP and then rapidly injected into the hot $Cd(oleate)_2$ solution. After 5 min, the heating mantle was removed and the cooled solution of QDs was purified by flocculation with ethanol and methanol followed by resuspension in toluene.

CdS shells were grown onto the CdSe cores using a procedure adapted from ref [7]. For a typical shell growth, a 0.16 M $Cd(oleate)_2$ solution in ODE and a 0.20 M solution of OT in ODE were separately injected at 2.5 mL/hour to a degassed solution containing 200 nmol of CdSe cores in 4g of ODE and 2g of HDA at 200°C. Once the injection was started, the temperature of the solution was raised to 300°C and held there until the injection was complete. The total volume of each solution injected was varied depending on the desired shell thickness, while the volumes for the two shell precursor solutions were kept equal. After the injection was complete, the solution was cooled to room temperature and the QDs purified by flocculation with ethanol and methanol followed by resuspension in toluene.

2.6.4 Physical characterization. Transmission electron miscroscope (TEM) images were obtained using a FEI Tecnai G2 F20 operating at 200 kV. Quantum yields were measured on colloidal QD suspensions by exciting samples with a Xe lamp coupled to a monochromator (λ_{exc}

= 450 nm) and detecting in an external quantum-efficiency integrating sphere (Hamamatsu C9920-12). All spectroscopic measurements were performed at room temperature on suspensions of colloidal QDs in toluene. Absorption spectra were measured in a Cary 500 (Varian) spectrophotometer. QD concentrations were determined using the absorption intensity at the first excitonic peak and a calibration curve for CdSe QDs.[41] For infrared (IR) absorption measurements, QDs were mixed with excess $LiBEt_3H$ in the dark in a nitrogen-filled glovebox, and the solution loaded into an air-free IR cell with either CaF_2 (CdSe/0CdS and CdSe/2CdS in toluene) or KBr (CdSe/7CdS in cyclohexane) windows separated by a 100 μm Teflon spacer. Measurements were collected on an FTIR spectrometer (ThermoScientific Nicolet-8700) with a HgCdTe detector. Continuous-wave PL spectra were measured by exciting the sample with a 5 mW 405 nm laser and detecting using an OceanOptics 2000+ spectrometer. Time-resolved PL measurements were performed using the frequency-doubled output of a Ti:sapphire laser at a 200-kHz repetition rate (405 nm, 150 fs pulse, 1.2–1.5 nJ/pulse). Decay curves were measured using a monochromator and streak camera with an instrument response function of ~15 ps.

2.6.5 Photodoping. Photodoping was performed following the method introduced in ref. [13]. QDs were dried and resuspended in anhydrous toluene in a nitrogen-filled glovebox prior to photodoping experiments. Samples were diluted to the desired concentration (generally ~100 nM for PL experiments), and 50–1000 equivalents of $LiBEt_3H$ (typically ~0.01 M in toluene) were added. Samples were irradiated with a 5 mW 405 nm laser to achieve desired level of photodoping. To achieve maximal photodoping, $LiBEt_3H$ was added in small increments to mitigate sample scattering and etching.

2.6.6 Quantification of $\langle n \rangle$. A solution of CdSe/7CdS QDs in toluene was prepared in a nitrogen-filled glovebox and measured in a 1-cm pathlength quartz cuvette. Spectra were collected using an OceanOptics 2000+ spectrophotometer with an absorption attachment. ~200 equivalents of $LiBEt_3H$ were added, and photodoping was performed using the OceanOptics light source for photoexcitation until no additional bleach was observed over the course of 30 sec. These excess electrons were then quantified *via* titration by addition of 10-μL aliquots of 9 μM $[FeCp^*_2][BAr^F_4]$ in THF. The light source was switched off during titration to avoid *in situ* photodoping between spectral collections. The titration took less than 10 min to complete, and thus anaerobic recovery for this thick-shelled sample was negligible over the course of the titration.

2.6.7 Anaerobic recovery. A series of QD samples was photodoped with careful attention paid to minimize differences in sample handling. The samples were prepared with the same optical density at their respective first absorption peak maxima in a solution of 30 μM $LiBEt_3H$ in toluene. Each was prepared anaerobically in a quartz cuvette equipped with a magnetic stir bar and sealed with a Teflon stopper. A photolysis lamp paired with a monochromator was tuned to selectively photoexcite each sample at its respective first excitonic absorption feature, and the light was focused onto the cuvette, which was set to stir inside the Cary spectrophotometer sample cavity. The power of the photolysis light was the same for all samples (0.5 mW), and each sample was irradiated for a total of 30 min. After 30 min, the lamp was switched off, and absorption scans were intermittently collected to monitor the rate of anaerobic recovery.

2.6.8 Spectral analysis. Absorption spectra at different values of $\langle n \rangle$ were fit to a sum of four Gaussians using a global fitting procedure. Widths were fixed, but energies and intensities were allowed to float to reflect the extent of photodoping and electron accumulation. For analysis of the PL spectra, the spectrum of neutral ($\langle n \rangle = 0$) CdSe/7CdS QDs was fitted. Upon photodoping and with increasing $\langle n \rangle$, this band was allowed to shift to lower energy as a new fixed-width

Gaussian feature (ascribed to emission involving recombination of $1P_e$ electrons) gained intensity at 2.01 eV. For PL decay analysis, global tri-exponential fitting of the PL decay curves collected for the CdSe/7CdS QD sample at various photodoping levels yielded the fitted values of τ corresponding to X, X^-, and X^{2-} listed in Table 2.1, and the fitted X, X^-, and X^{2-} amplitudes plotted *vs* $\langle n \rangle$ in Figure 2.9A.

2.7 References

1. Peng, X.; Schlamp, M. C.; Kadavanich, A. V.; Alivisatos, A. P., Epitaxial Growth of Highly Luminescent CdSe/CdS Core/Shell Nanocrystals with Photostability and Electronic Accessibility. *J. Am. Chem. Soc.* **1997,** *119*, 7019-7029.
2. Li, J. J.; Wang, Y. A.; Guo, W.; Keay, J. C.; Mishima, T. D.; Johnson, M. B.; Peng, X., Large-Scale Synthesis of Nearly Monodisperse CdSe/CdS Core/Shell Nanocrystals Using Air-Stable Reagents *via* Successive Ion Layer Adsorption and Reaction. *J. Am. Chem. Soc.* **2003,** *125*, 12567-12575.
3. Mahler, B.; Spinicelli, P.; Buil, S.; Quelin, X.; Hermier, J.-P.; Dubertret, B., Towards Non-Blinking Colloidal Quantum Dots. *Nat. Mater.* **2008,** *7*, 659-664.
4. Chen, Y.; Vela, J.; Htoon, H.; Casson, J. L.; Werder, D. J.; Bussian, D. A.; Klimov, V. I.; Hollingsworth, J. A., “Giant” Multishell CdSe Nanocrystal Quantum Dots with Suppressed Blinking. *J. Am. Chem. Soc.* **2008,** *130*, 5026-5027.
5. Malko, A. V.; Park, Y.-S.; Sampat, S.; Galland, C.; Vela, J.; Chen, Y.; Hollingsworth, J. A.; Klimov, V. I.; Htoon, H., Pump-Intensity- and Shell-Thickness-Dependent Evolution of Photoluminescence Blinking in Individual Core/Shell CdSe/CdS Nanocrystals. *Nano Lett.* **2011,** *11*, 5213-5218.
6. Galland, C.; Ghosh, Y.; Steinbrück, A.; Hollingsworth, J. A.; Htoon, H.; Klimov, V. I., Lifetime Blinking in Nonblinking Nanocrystal Quantum Dots. *Nat. Commun.* **2012,** *3*, 908.
7. Chen, O.; Zhao, J.; Chauhan, V. P.; Cui, J.; Wong, C.; Harris, D. K.; Wei, H.; Han, H.-S.; Fukumura, D.; Jain, R. K.; Bawendi, M. G., Compact High-Quality CdSe–CdS Core–Shell Nanocrystals with Narrow Emission Linewidths and Suppressed Blinking. *Nat. Mater.* **2013,** *12*, 445-451.
8. Park, Y.-S.; Bae, W. K.; Pietryga, J. M.; Klimov, V. I., Auger Recombination of Biexcitons and Negative and Positive Trions in Individual Quantum Dots. *ACS Nano* **2014,** *8*, 7288-7296.
9. Rabouw, F. T.; Vaxenburg, R.; Bakulin, A. A.; Dijk-Moes, R. J. A. v.; Bakker, H. J.; Rodina, A.; Lifshitz, E.; Efros, A. L.; Koenderink, A. F.; Vanmaekelbergh, D., Dynamics of Intraband and Interband Auger Processes in Colloidal Core–Shell Quantum Dots. *ACS Nano* **2015,** *9*, 10366-10376.
10. Ehrat, F.; Simon, T.; Stolarczyk, J. K.; Feldmann, J., Size Effects on Photocatalytic H_2 Generation with CdSe/CdS Core-Shell Nanocrystals. *Z. Phys. Chem.* **2015,** *229*, 205-219.
11. Schimpf, A. M.; Knowles, K. E.; Carroll, G. M.; Gamelin, D. R., Electronic Doping and Redox Potential Tuning in Colloidal Semiconductor Nanocrystals. *Acc. Chem. Res.* **2015,** *48*, 1929-1937.

12. Schimpf, A. M.; Gunthardt, C. E.; Rinehart, J. D.; Mayer, J. M.; Gamelin, D. R., Controlling Carrier Densities in Photochemically Reduced Colloidal ZnO Nanocrystals: Size Dependence and Role of the Hole Quencher. *J. Am. Chem. Soc.* **2013,** *135*, 16569-16577.
13. Rinehart, J. D.; Schimpf, A. M.; Weaver, A. L.; Cohn, A. W.; Gamelin, D. R., Photochemical Electronic Doping of Colloidal CdSe Nanocrystals. *J. Am. Chem. Soc.* **2013,** *135*, 18782-18785.
14. Cohn, A. W.; Rinehart, J. D.; Schimpf, A. M.; Weaver, A. L.; Gamelin, D. R., Size Dependence of Negative Trion Auger Recombination in Photodoped CdSe Nanocrystals. *Nano Lett.* **2014,** *14*, 353-358.
15. Schimpf, A. M.; Thakkar, N.; Gunthardt, C. E.; Masiello, D. J.; Gamelin, D. R., Charge-Tunable Quantum Plasmons in Colloidal Semiconductor Nanocrystals. *ACS Nano* **2014,** *8*, 1065-1072.
16. Carroll, G. M.; Brozek, C. K.; Hartstein, K. H.; Tsui, E. Y.; Gamelin, D. R., Potentiometric Measurements of Semiconductor Nanocrystal Redox Potentials. *J. Am. Chem. Soc.* **2016,** *138*, 4310-4313.
17. Carroll, G. M.; Tsui, E. Y.; Brozek, C. K.; Gamelin, D. R., Spectroelectrochemical Measurement of Surface Electrostatic Contributions to Colloidal CdSe Nanocrystal Redox Potentials. *Chem. Mater.* **2016,** *28*, 7912-7918.
18. Tsui, E. Y.; Hartstein, K. H.; Gamelin, D. R., Selenium Redox Reactivity on Colloidal CdSe Quantum Dot Surfaces. *J. Am. Chem. Soc.* **2016,** *138*, 11105-11108.
19. Brozek, C. K.; Hartstein, K. H.; Gamelin, D. R., Potentiometric Titrations for Measuring the Capacitance of Colloidal Photodoped ZnO Nanocrystals. *J. Am. Chem. Soc.* **2016,** *138*, 10605-10610.
20. Tsui, E. Y.; Carroll, G. M.; Miller, B.; Marchioro, A.; Gamelin, D. R., Extremely Slow Spontaneous Electron Trapping in Photodoped *n*-Type CdSe Nanocrystals. *Chem. Mater.* **2017,** *29*, 3754-3762.
21. Wu, K.; Lim, J.; Klimov, V. I., Superposition Principle in Auger Recombination of Charged and Neutral Multicarrier States in Semiconductor Quantum Dots. *ACS Nano* **2017,** *11*, 8437-8447.
22. Wang, C.; Wehrenberg, B. L.; Woo, C. Y.; Guyot-Sionnest, P., Light Emission and Amplification in Charged CdSe Quantum Dots. *J. Phys. Chem. B* **2004,** *108*, 9027-9031.
23. Jha, P. P.; Guyot-Sionnest, P., Photoluminescence Switching of Charged Quantum Dot Films. *J. Phys. Chem. C* **2007,** *111*, 15440-15445.
24. Sampat, S.; Karan, N. S.; Guo, T.; Htoon, H.; Hollingsworth, J. A.; Malko, A. V., Multistate Blinking and Scaling of Recombination Rates in Individual Silica-Coated CdSe/CdS Nanocrystals. *ACS Photonics* **2015,** *2*, 1505-1512.
25. Coropceanu, I.; Bawendi, M. G., Core/Shell Quantum Dot Based Luminescent Solar Concentrators with Reduced Reabsorption and Enhanced Efficiency. *Nano Lett.* **2014,** *14*, 4097-4101.
26. Steiner, D.; Dorfs, D.; Banin, U.; Della Sala, F.; Manna, L.; Millo, O., Determination of Band Offsets in Heterostructured Colloidal Nanorods Using Scanning Tunneling Spectroscopy. *Nano Lett.* **2008,** *8*, 2954-2958.
27. Carroll, G. M.; Tsui, E. Y.; Brozek, C. K.; Gamelin, D. R., Spectroelectrochemical Measurement of Surface Electrostatic Contributions to Colloidal CdSe Nanocrystal Redox Potentials. *Chem. Mater.* **2016,** *28*, 7912-7918.

28. Saba, M.; Aresti, M.; Quochi, F.; Marceddu, M.; Loi, M. A.; Huang, J.; Talapin, D. V.; Mura, A.; Bongiovanni, G., Light-Induced Charged and Trap States in Colloidal Nanocrystals Detected by Variable Pulse Rate Photoluminescence Spectroscopy. *ACS Nano* **2013,** *7*, 229-238.
29. Hayoun, R.; Whitaker, K. M.; Gamelin, D. R.; Mayer, J. M., Electron Transfer Between Colloidal ZnO Nanocrystals. *J. Am. Chem. Soc.* **2011,** *133*, 4228-4231.
30. Cohn, A. W.; Janßen, N.; Mayer, J. M.; Gamelin, D. R., Photocharging ZnO Nanocrystals: Picosecond Hole Capture, Electron Accumulation, and Auger Recombination. *J. Phys. Chem. C* **2012,** *116*, 20633-20642.
31. Jha, P. P.; Guyot-Sionnest, P., Trion Decay in Colloidal Quantum Dots. *ACS Nano* **2009,** *3*, 1011-1015.
32. Schimpf, A. M.; Runnerstrom, E. L.; Lounis, S. D.; Milliron, D. J.; Gamelin, D. R., Redox Energies and Plasmon Resonance Energies of Photodoped In_2O_3 and Sn-doped In_2O_3 Nanocrystals. *J. Am. Chem. Soc.* **2015,** *137*, 518-524.
33. Yu, D.; Wang, C.; Guyot-Sionnest, P., *n*-Type Conducting CdSe Nanocrystal Solids. *Science* **2003,** *300*, 1277-1280.
34. Kalevich, V. K.; Merkulov, I. A.; Shiryaev, A. Y.; Kavokin, K. V.; Ikezawa, M.; Okuno, T.; Brunkov, P. N.; Zhukov, A. E.; Ustinov, V. M.; Masumoto, Y., Optical Spin Polarization and Exchange Interaction in Doubly Charged InAs Self-Assembled Quantum Dots. *Phys. Rev. B* **2005,** *72*, 045325.
35. Stern, N. P.; Poggio, M.; Bartl, M. H.; Hu, E. L.; Stucky, G. D.; Awschalom, D. D., Spin Dynamics in Electrochemically Charged CdSe Quantum Dots. *Phys. Rev. B* **2005,** *72*, 161303.
36. Ochsenbein, S. T.; Feng, Y.; Whitaker, K. M.; Badaeva, E.; Liu, W. K.; Li, X.; Gamelin, D. R., Charge-Controlled Magnetism in Colloidal Doped Semiconductor Nanocrystals. *Nat. Nanotechnol.* **2009,** *4*, 681-687.
37. Schimpf, A. M.; Rinehart, J. D.; Ochsenbein, S. T.; Gamelin, D. R., Charge-State Control of Mn^{2+} Spin Relaxation Dynamics in Colloidal *n*−Type $Zn_{1-x}Mn_xO$ Nanocrystals. *J. Phys. Chem. Lett.* **2015,** *6*, 1748-1753.
38. Beaulac, R.; Archer, P. I.; Ochsenbein, S. T.; Gamelin, D. R., Mn^{2+}-Doped CdSe Quantum Dots: New Inorganic Materials for Spin-Electronics and Spin-Photonics. *Adv. Funct. Mater.* **2008,** *18*, 3873-3891.
39. Nelson, H. D.; Bradshaw, L. R.; Barrows, C. J.; Vlaskin, V. A.; Gamelin, D. R., Picosecond Dynamics of Excitonic Magnetic Polarons in Colloidal Diffusion-Doped $Cd_{1-x}Mn_xSe$ Quantum Dots. *ACS Nano* **2015,** *9*, 11177-11191.
40. Qu, L.; Peng, X., Control of Photoluminescence Properties of CdSe Nanocrystals in Growth. *J. Am. Chem. Soc.* **2002,** *124*, 2049-2055.
41. Yu, W. W.; Qu, L.; Guo, W.; Peng, X., Experimental Determination of the Extinction Coefficient of CdTe, CdSe, and CdS Nanocrystals. *Chem. Mater.* **2003,** *15*, 2854-2860.

Chapter 3: Copper-Coupled Electron Transfer in Colloidal Plasmonic Copper-Sulfide Nanocrystals Probed by *In Situ* Spectroelectrochemistry

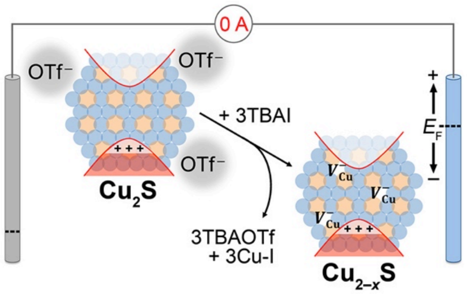

Reproduced with permission from:
Hartstein, K. H.; Brozek, C. K.;
Hinterding, S. O. M.; Gamelin, D. R.
J. Am. Chem. Soc. **2018**, *140*, 3434–3442.

3.1 Overview

Copper-sulfide nanocrystals can accommodate considerable densities of delocalized valence-band holes, introducing localized surface plasmon resonances (LSPRs) attractive for infrared plasmonic applications. Chemical control over nanocrystal shape, composition, and charge-carrier densities further broadens their scope of potential properties and applications. Although a great deal of control over LSPRs in these materials has been demonstrated, structural complexities have inhibited detailed descriptions of the microscopic chemical processes that transform them from nearly intrinsic to degenerately doped semiconductors. A comprehensive understanding of these transformations will facilitate use of these materials in emerging technologies. Here, we apply spectroelectrochemical potentiometry as a quantitative *in situ* probe of copper-sulfide nanocrystal Fermi-level energies (E_F) during redox reactions that switch their LSPR bands on and off. We demonstrate spectroscopically indistinguishable LSPR bands in low-chalcocite copper-sulfide nanocrystals with and without lattice cation vacancies and show that cation vacancies are much more effective than surface anions at stabilizing excess free carriers. The appearance of the LSPR band, the shift in E_F, and the change in crystal structure upon nanocrystal oxidation are all fully reversible upon addition of outer-sphere reductants. These measurements further allow quantitative comparison of the coupled and stepwise oxidation/cation-vacancy-formation reactions associated with LSPRs in copper-sulfide nanocrystals, highlighting fundamental thermodynamic considerations relevant to technologies that rely on reversible or low-driving-force plasmon generation in semiconductor nanostructures.

3.2 Introduction

Colloidal semiconductor nanocrystals possessing excess delocalized charged carriers are garnering considerable attention in fundamental science and for applications in a wide range of emerging technologies, from photothermal therapies and sensing to catalysis, photodetection, and smart windows.[1-5] Localized surface plasmon resonances (LSPRs) are observed in heavily doped semi-metallic semiconductor nanocrystals at lower energies than in metals, expanding the energy range accessible to plasmonic technologies into the infrared.[6-14] These materials are also attractive because of the tunability of their carrier concentrations, and hence of their associated spectral properties. Carrier concentrations can be tuned *via* tunable dopant incorporation and activation.[3,15-18] Perhaps even more interestingly, it can also be achieved post-synthetically *via* redox manipulation.[3,10,19-28] The capability to tune carrier densities from ~0 to ~10^{21} cm^{-3}, in many cases reversibly, introduces considerable opportunity for unique applications of plasmonic semiconductor nanostructures as plasmonic switches and biological sensors.

Among plasmonic semiconductor nanocrystals, copper-sulfide and related chalcogenide nanocrystals are unusual in that their plasmons derive from excess holes rather than excess electrons. These charge carriers are easily introduced *via* oxidation in air or using a variety of common oxidants.[2,8,29-34] In bulk, binary copper chalcogenides are typically *p*-type and have widely tunable carrier densities, stoichiometries, and crystal structures. Similarly, in copper-sulfide nanocrystals, *p* doping is generally associated with lattice cation-vacancy formation, such that the charge of each excess delocalized hole is compensated by the loss of one lattice Cu^+ to form a cation-deficient crystal lattice ($Cu_{2-x}S$). A variety of redox reagents have been explored for introducing charge carriers into Cu_2S nanocrystals,[2] and to date, most descriptions of these chemistries invoke a cation-vacancy charge-compensation mechanism.[13] The equilibrium constant for conversion from stoichiometric Cu_2S to cation-deficient $Cu_{2-x}S$ depends not only on the change in this lattice but also on the stability of the copper-containing reaction product,[2] yet little is known about the thermodynamics of the microscopic transformations in these nanocrystals.

Spectroelectrochemistry has recently proven useful for investigating optical changes correlated with redox changes in copper-sulfide nanocrystal films.[35-38] Thin-film spectroelectrochemistry has long served as a powerful tool for investigating the electronic structures and photophysics of nanocrystals possessing excess charge carriers. Recent spectroelectrochemical results have also highlighted large (hundreds of millivolts) shifts in onset potentials for oxidation or reduction of identical nanocrystals depending on inter-nanocrystal spacing and the number of nanocrystal layers on the electrode surface.[39] These shifts ultimately reflect changes in the efficacy of electrolyte diffusion into such films.[39] Importantly, because of such effects, the redox potential measured for a given nanocrystal film is a property of the film itself, and can be substantially different from the potential associated with the same redox reaction involving the free-standing nanocrystals in solution, or the same nanocrystals in a more porous architecture. To circumvent this issue, we have recently demonstrated the use of nanocrystal potentiometry as a powerful approach to probing the redox properties of free-standing colloidal semiconductor nanocrystals.[40-42] Potentiometry measures the Fermi level (E_F) of a colloidal nanocrystal ensemble without current flow, allowing retention of the native nanocrystal surface chemistry and enabling *in situ* monitoring of chemical redox manipulations. Here, we apply spectroelectrochemical potentiometry as a probe of E_F in free-standing colloidal copper-sulfide nanocrystals, monitoring nanocrystal redox reactions using both inner- and outer-sphere redox reagents. These measurements allow quantitative determination of the potential changes that turn on or turn off the nanocrystal LSPRs. With this approach, we demonstrate that valence-band oxidation can be decoupled from cation-vacancy formation, but at significant thermodynamic cost. Analysis of these data allows quantitative comparison of the influence of different charge-carrier-compensation motifs (cation vacancies *vs* surface anions) on carrier stability in plasmonic copper-sulfide nanocrystals. This understanding in turn provides guidelines for identifying conditions under which nanocrystal LSPRs can be modulated at minimal thermodynamic (energy) cost.

3.3 Results & analysis

Figure 3.1 presents structural characterization data for the nanocrystals used in this study. Figure 3.1A shows a TEM image and size histogram for d = 5.4 nm nanocrystals used for potentiometric measurements. Figure 3.1B illustrates that, as prepared, these and a sample of larger ($d \sim 12$ nm) nanocrystals both reference to stoichiometric low-chalcocite Cu_2S. The larger nanocrystals are useful for analysis of XRD peak shifts.

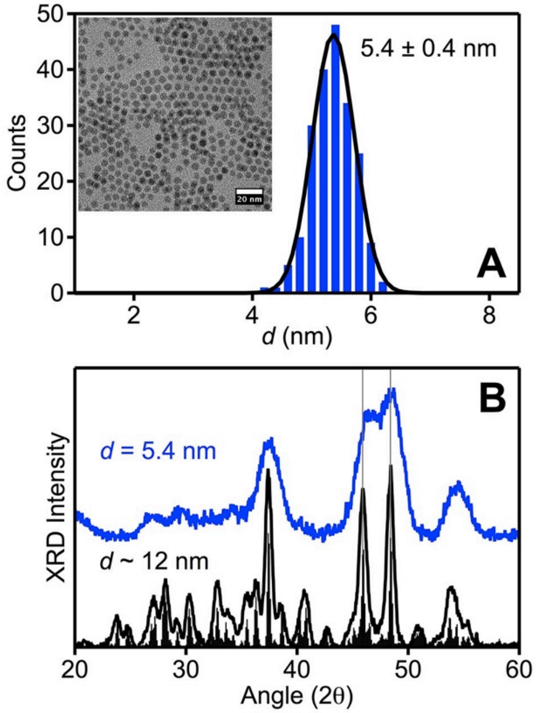

Figure 3.1. (**A**) TEM image (inset) and size histogram of a sample of Cu_2S nanocrystals used for potentiometry measurements. The size histogram was generated by counting >200 nanocrystals. The length of the scale bar is 20 nm. (**B**) XRD data for the $d = 5.4$ nm Cu_2S nanocrystals from panel A, as well as for a sample of $d \sim 12$ nm Cu_2S nanocrystals. The vertical lines indicate the (110) and (103) reflections at 45.9° and 48.4°, respectively, and are consistent with stoichiometric low-chalcocite Cu_2S, the bulk pattern of which is shown for reference.

Figure 3.2 plots absorption spectra of the colloidal $d = 5.4$ nm Cu_2S nanocrystals from Figure 3.1 collected at various levels of oxidation after reaction with I_2. Consistent with previous reports,[2,43] reaction with I_2 generates a pronounced new absorption band in the near-infrared. Addition of more I_2 shifts this band to higher energies and increases its intensity. This near-infrared absorption is attributable to an LSPR stemming from the introduction of delocalized valence-band holes (h^{+}_{VB}) in these nanocrystals. In addition to generating this LSPR band, reaction with I_2 also bleaches the visible inter-band absorption somewhat, consistent with band-edge filling and the Burstein-Moss effect.

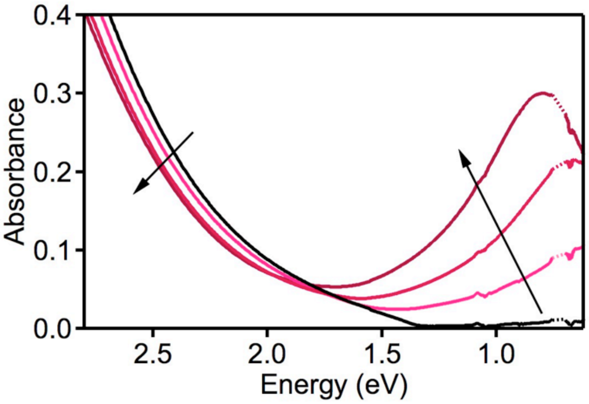

Figure 3.2. Absorption spectra of colloidal *d* = 5.4 nm copper-sulfide nanocrystals as-prepared (black) and at various levels of oxidation during reaction with I_2. The arrows indicate the direction of the spectral changes with increasing oxidation. An artifact at ~0.7 eV from imperfect solvent subtraction has been removed and replaced with dotted lines for clarity.

To probe this reaction in more detail, and to compare the results from different methods of nanocrystal oxidation, we performed spectroelectrochemical potentiometry measurements on the same nanocrystals. To highlight LSPR formation and changes to the inter-band absorption, differential absorption spectra are presented, obtained by subtracting the spectrum of the as-prepared nanocrystals from each of the other spectra. Figure 3.3 plots such differential absorption spectra of the colloidal $d = 5.4$ nm Cu_2S nanocrystals from Figures 3.1 and 3.2 in a 0.1 M $TBAPF_6$ THF electrolyte solution after addition of 260 equivalents of either FcOTf or ½I_2 (*i.e.*, 130 equivalents of I_2). Both oxidants cause a similar LSPR feature to emerge in the near-infrared. Overall, the data in Figure 3.3 demonstrate that the equimolar addition of either FcOTf or I_2 oxidizing equivalents to $d = 5.4$ nm Cu_2S nanocrystals generates essentially identical LSPR bands. The change in inter-band absorption is slightly greater following oxidation by I_2 than by FcOTf. From Drude analysis of the LSPR bands, we estimate that 260 equivalents of Fc^+ or ½I_2 both introduce ~130 h^+_{VB} per $d = 5.4$ nm nanocrystal, yielding an average carrier density of $\langle P \rangle \sim 1.5 \times 10^{21}$ cm^{-3}. This value of $\langle P \rangle$ is consistent with numbers reported elsewhere for Cu_2S

nanocrystals reacted with comparable amounts of I_2.[43] Although this precise value may have some associated uncertainty,[44] the data in Figure 3.3 demonstrate that both oxidants generate indistinguishable free-carrier densities.

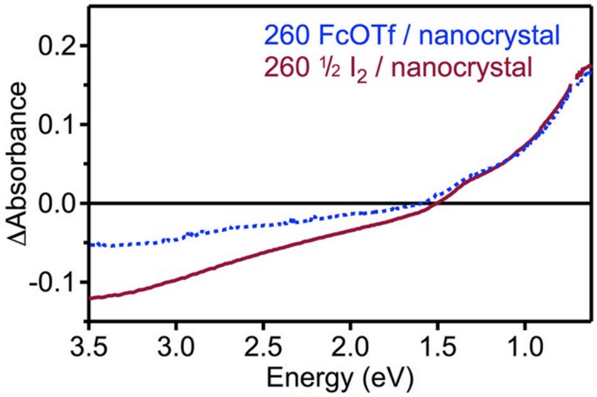

Figure 3.3. Differential absorption spectra of d = 5.4 nm copper-sulfide nanocrystals after addition of 260 equivalents of either Fc^+ (added as FcOTf, dashed) or $½I_2$ (thick solid). Upon oxidation, the onset of inter-band absorption blue shifts and a broad LSPR band emerges at low energy. An artifact at ~0.7 eV resulting from imperfect solvent subtraction was removed for clarity.

Concurrent with the spectroscopic measurements of Figure 3.3, we collected *in situ* potentiometric data to compare the potentials associated with the excess holes in these oxidized nanocrystals. Figure 3.4A plots the differential absorption at 1.0 eV *vs* time following injection of 260 equivalents of oxidant (FcOTf or $½I_2$) into the nanocrystal solution at $t = 0$. Figure 3.4B plots open-circuit potentials (V_{OC}) *vs* time measured simultaneously with the data in panel A. With both oxidants, the near-infrared absorption rapidly increases upon addition of the oxidant and then slowly drops over several minutes to converge to an equilibrium value, at which point the LSPR peak position and width become constant (see Appendix B for more extensive data). Simultaneously, V_{OC} rapidly shifts to a more positive value upon addition of the oxidant, and it also stabilizes at a new equilibrium potential (V_{eq}). This electrochemical potential can be equated with E_F of the nanocrystal solution,[40] and its rise reflects the incorporation of p-type carriers.[44]

Quantitatively, V_{eq} is nearly 300 mV more positive when using FcOTf as the oxidant than when using I_2, *i.e.*, the valence-band holes formed by oxidation with FcOTf are hundreds of mV *less* stable than those formed by oxidation with I_2 at the same free-carrier density $\langle P \rangle$. This difference indicates that despite generating effectively indistinguishable LSPRs, the two oxidants yield substantially different *p*-doped nanocrystals. The shaded boxes and error bars on the right side of Figure 3.4B summarize the results from multiple measurements, showing that the contrast between the two oxidants is significant and reproducible.

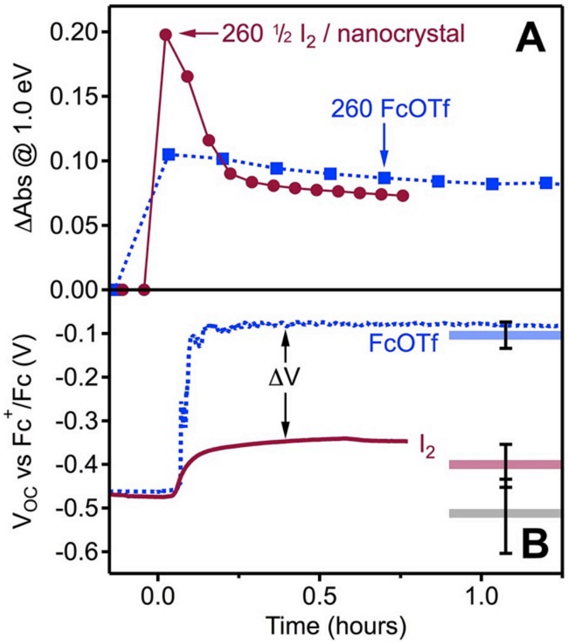

Figure 3.4. (**A**) Differential absorption intensity at 1.0 eV and (**B**) V_{OC} plotted *vs* time for d = 5.4 nm copper-sulfide nanocrystals oxidized with 260 equivalents of ½I_2 (solid) and FcOTf (dashed). Lines connecting experimental data points (symbols in panel A) provide visual guides. The two oxidants yield nanocrystals with similar LSPR absorption features (see Figure 3.2) but with V_{eq} values that differ by nearly 300 mV (indicated here by ΔV arrow). Shaded boxes and vertical error bars indicate the mean and standard deviation in V_{eq} from multiple measurements on nanocrystals prior to oxidation (20 measurements), and after addition of 260 equivalents of either Fc^+ (2 measurements with FcOTf, 3 with $FcBF_4$) or ½I_2 (3 measurements).

Structural characterization methods provide insight into this contrast in V_{eq} between nanocrystals oxidized by I_2 and FcOTf. For these structural measurements, larger nanocrystals were used than in the spectroelectrochemistry experiments of Figure 3.4 because their narrower XRD peak widths facilitate interpretation, but XRD data from the smaller nanocrystals of Figure 3.4 still show the same trends as described below (see Appendix B). Figure 3.5 presents XRD data collected for the $d \sim 12$ nm Cu_2S nanocrystals of Figure 3.1 as-prepared and following oxidation by $\frac{1}{2}I_2$ or FcOTf. These data show that I_2 oxidation shifts the (110) and (103) diffraction peaks of as-prepared low-chalcocite Cu_2S nanocrystals at 45.9° and 48.4° to wider angles, attributable to lattice contraction caused by cation-vacancy formation. Additionally, new peaks emerge that are attributable to zinc blende CuI (marshite). Parallel XPS measurements indicate that copper maintains its +1 oxidation state, and the I($3d_{5/2}$) binding energy suggests the presence of I^- (see Appendix B). These results agree well with a recent study of I_2-treated Cu_2S nanocrystals indicating formation of cation vacancies and CuI under similar reaction conditions.[43] Similar XRD shifts to wider angles have also been reported for Cu_2S nanocrystals exposed to dioxygen, again attributed to lattice contraction caused by cation vacancies.[38] In contrast with these results, the XRD data in Figure 3.5 for the nanocrystals oxidized using FcOTf do not show any detectable shift of the same diffraction peaks, and hence show no evidence of cation-vacancy formation. In this case, the data are consistent with retention of a stoichiometric Cu_2S lattice. When combined with the potentiometry data of Figure 3.4B, these XRD data thus suggest a positive correlation between cation-vacancy formation and the stability of valence-band holes in Cu_2S nanocrystals.

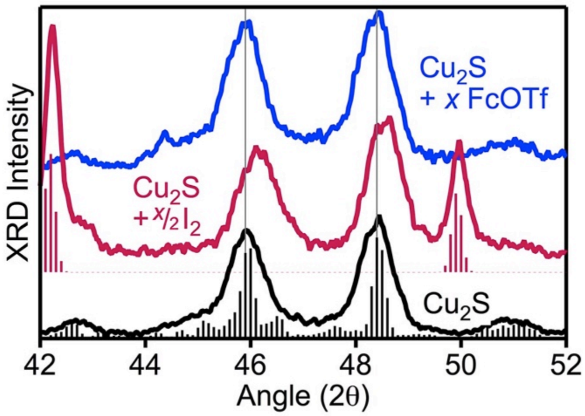

Figure 3.5. XRD of d ~ 12 nm copper-sulfide nanocrystals as prepared (bottom), and with equimolar additions of ½I$_2$ (middle) or FcOTf (top). The vertical dotted lines indicate the positions of the (110) and (103) lattice plane reflections (45.9° and 48.4°, respectively) in stoichiometric Cu$_2$S nanocrystals (reference shown as sticks). Shifting of these peaks to wider angles indicates a contraction of the nanocrystal lattice upon I$_2$ addition, along with zinc blende CuI formation (bulk pattern shown as sticks for reference). These changes are not observed upon addition of FcOTf. Oxidizing smaller (d = 5.4 nm) Cu$_2$S nanocrystals with I$_2$ also produces CuI, but the lattice contraction is obscured by broader peak widths. See Appendix B for complete XRD data.

The spectroelectrochemical and structural data indicate that although Cu$_2$S nanocrystals oxidized by FcOTf can incorporate valence-band holes, they do not form cation vacancies to stabilize these holes, likely because of unfavorable Cu$^+$ solvation thermodynamics under these conditions. We hypothesized that, in contrast with the FcOTf reaction, Cu-I bond formation provides the necessary driving force to induce cation-vacancy formation in reactions involving I$_2$. To test this hypothesis, we examined whether I$^-$ would promote expulsion of Cu$^+$ ions from *p*-type Cu$_2$S nanocrystals that had already been oxidized by FcOTf, thereby stabilizing their excess holes. Figure 3.6 presents spectroscopic, electrochemical, and XRD data collected for Cu$_2$S nanocrystals that were first oxidized with FcOTf and then exposed to tetrabutylammonium iodide (TBAI) as a source of I$^-$. The data in Figure 3.6A show that adding TBAI to *p*-type Cu$_2$S nanocrystals indeed drives V_{OC} more negative, corresponding to stabilization of $\mathrm{h}^+_{\mathrm{VB}}$. At ~950 equivalents of TBAI, E_F has been stabilized by nearly 300 mV without any detectable change to the LSPR band (Figure 3.6B, collected simultaneously). For reference, the values of V_{eq} determined in Figure 3.4 are marked in Figure 3.6A. The XRD data in the inset of Figure 3.6B demonstrate that adding I^- to *p*-doped nanocrystals formed by oxidation using FcOTf indeed induces a lattice contraction, analogous to the changes observed upon direct oxidation by I_2. CuI is also detected by XRD, but this crystallization takes time and shows an expanded lattice constant, suggesting the possibility that TBA^+ may also incorporate into the crystalline product when formed *via* this route. We note the absence of several diffraction features characteristic of low-chalcocite copper sulfide (*e.g.*, ~41°, see Appendix B) after stepwise oxidation and I^- addition, suggesting that this route yields a more ordered structure than direction oxidation by I_2. No structural changes were observed when TBAI was added to the Cu_2S nanocrystals without also adding FcOTf (see Appendix B). These results demonstrate that both valence-band holes and a suitable Cu^+-binding agent in solution are required to induce cation-vacancy formation. Although crystalline CuI is observed by XRD in some cases, its appearance is not immediate, and cation vacancies are observed even in the absence of this crystalline product, suggesting participation of a soluble Cu-I species that drives the cation-vacancy formation. It is noteworthy that the LSPR band remains unchanged despite the introduction of a high density of cation vacancies (Figure 3.6B); this observation implies that defect (vacancy) scattering makes no significant contribution to the ensemble LSPR band shape. Although the LSPR band remains unchanged, the inter-band absorption does shift somewhat upon TBAI addition, reminiscent of the difference between absorption spectra measured with FcOTf and $\frac{1}{2}I_2$ nanocrystal oxidation shown in Figure 3.3. This observation is consistent with a stoichiometry-dependent bandgap of the binary Cu-S system, in which smaller Cu:S ratios yield wider bandgaps.[6,9,29,45] Overall, these data demonstrate that the $Cu_{2-x}S$ nanocrystal product obtained by oxidation of Cu_2S nanocrystals using I_2 can equivalently be obtained by stepwise outer-sphere oxidation with Fc^+ followed by extraction of lattice Cu^+ using I^-. By separating these two reaction steps (valence-band oxidation and cation-vacancy formation), it is possible to conclude that cation vacancies stabilize the Fermi-level holes in these nanocrystals by ~300 mV.

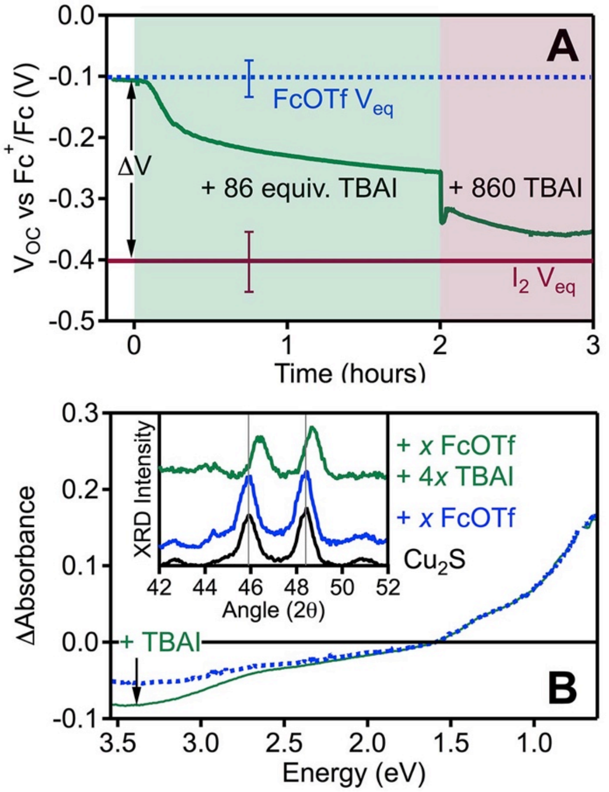

Figure 3.6. (**A**) V_{OC} *vs* time for *p*-doped d = 5.4 nm copper-sulfide nanocrystals formed by oxidation with FcOTf and subsequently treated with TBAI. TBAI was added at t = 0 and t = 2 hours in the quantities indicated. The horizontal lines indicate the V_{eq} values from Figure 4 for copper-sulfide nanocrystals oxidized with FcOTf (dashed) and with ½I_2 (solid). (**B**) Absorption spectra from the same experiment described in panel A, collected before TBAI addition (dashed) and t = 3 hours after TBAI addition (solid). The LSPR region remains unchanged despite the nearly 300 mV change in V_{OC} following TBAI addition. **Inset:** XRD data for d ~ 12 nm nanocrystals, showing no peak shift with FcOTf addition (data from Figure 3.5), and a significant lattice contraction with subsequent TBAI addition.

The chemical transformations accompanying nanocrystal oxidation by I_2 can also be reversed by adding the reductant $CoCp^*_2$. Figure 3.7A plots the differential absorption spectrum of $d = 5.4$ nm copper-sulfide nanocrystals collected after nanocrystal equilibration with added I_2 (solid, 520 oxidizing equivalents), along with spectra of the same oxidized sample collected after adding $CoCp^*_2$ in substoichiometric aliquots. The LSPR absorption decreases incrementally with each addition. Figure 3.7B plots the value of the differential absorption measured at 1.0 eV *vs* number of reducing equivalents ($CoCp^*_2$) per unit oxidizing equivalent (½I_2) and shows a smooth stepwise elimination of the LSPR with added reductant. Complete elimination of the LSPR is achieved at ~1.5 equivalents of $CoCp^*_2$ per ½I_2. Concomitantly, V_{eq} also steps negative with each addition (Figure 3.7C), reaching a final value nearly 500 mV more negative than measured for the oxidized nanocrystals. Figure 3.7D presents XRD data collected at key points in this reaction. These data show the characteristic peak shift upon Cu_2S nanocrystal oxidation with I_2, and show this peak subsequently return to its initial position following re-reduction using $CoCp^*_2$, without any discernible change to the nanocrystal size. The CuI diffraction peaks also disappear upon addition of $CoCp^*_2$. These data indicate that $CoCp^*_2$ both eliminates h^+_{VB} and drives Cu^+ back into the $Cu_{2-x}S$ lattice to reform Cu_2S nanocrystals. These results are supported by XPS measurements, which show that copper maintains its +1 oxidation state upon $CoCp^*_2$ addition, whereas the $I(3d_{5/2})$ peak shifts to an even lower binding energy, indicating that it remains reduced (I^-) but is likely associated with the cobalt ion of the $[CoCp^*_2]^+$ redox product (see Appendix B).

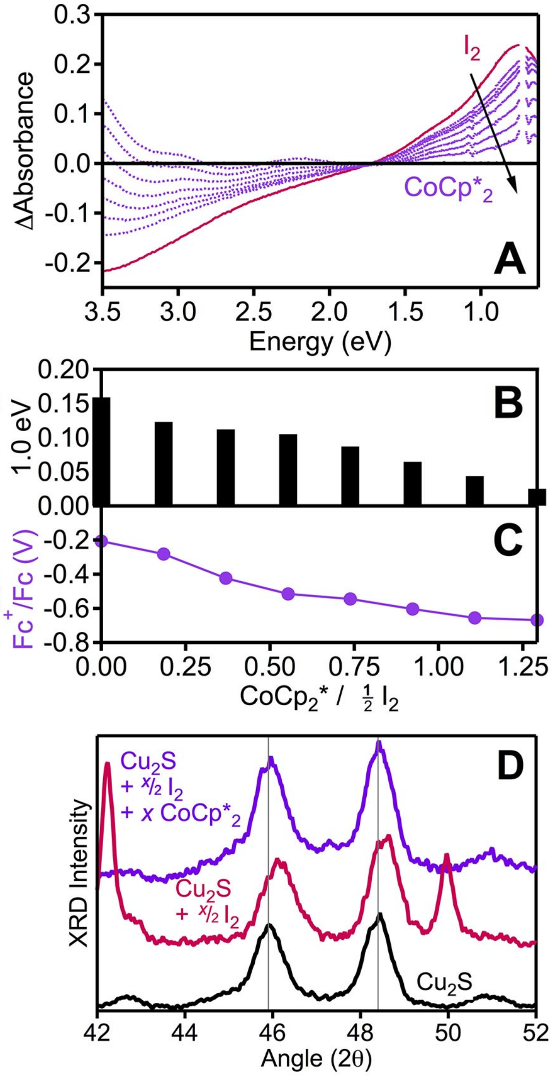

Figure 3.7. (**A**) Differential absorption spectra of d = 5.4 nm copper-sulfide nanocrystals reacted with 520 equivalents of $\frac{1}{2}I_2$ (solid) and after subsequent addition of sub-stoichiometric equivalents of $CoCp^*_2$ (dotted, recorded after equilibration). (**B**) Absorbance at 1.0 eV, plotted *vs* equivalents of $CoCp^*_2$ added. (**C**) V_{eq} measured after each addition of $CoCp^*_2$. (**D**) XRD data collected for a parallel reaction series using $d \sim 12$ nm nanocrystals, showing the results for as-prepared Cu_2S nanocrystals (bottom), the same nanocrystals oxidized using I_2 (middle, data from Figure 3.5), and the same nanocrystals subsequently reduced with $CoCp^*_2$ (top).

Eqs 3.1 and 3.2 summarize the chemistry involved in the oxidative and reductive transformations described above. Oxidation of Cu_2S nanocrystals by I_2 is described by eq 3.1, consistent with previous observations.[2,43] The subsequent reduction reaction illustrated in Figure 3.7 is described by eq 3.2. Here, beginning with the *p*-doped $Cu_{2-x}S$ nanocrystal and Cu-I products of eq 3.1, $CoCp^*_2$ addition generates $[CoCp^*_2]^+$, driving Cu-I dissociation and Cu^+ reentry into the $Cu_{2-x}S$ nanocrystals to re-form approximately stoichiometric Cu_2S nanocrystals. The liberated I^- is likely associated with the $[CoCp^*_2]^+$ redox product.

$$\mathrm{Cu_2S} + \tfrac{1}{2}x\mathrm{I_2} \rightarrow x\mathrm{h^+_{VB}}{:}\,\mathrm{Cu}_{2-x}\mathrm{S} + x[\mathrm{Cu{-}I}] \qquad (3.1)$$

$$\begin{aligned} &x\mathrm{h^+_{VB}}{:}\,\mathrm{Cu}_{2-x}\mathrm{S} + x[\mathrm{Cu{-}I}] + y\mathrm{CoCp^*_2} \rightarrow \\ &\qquad (x-y)\mathrm{h^+_{VB}}{:}\,\mathrm{Cu}_{2-(x-y)}\mathrm{S} + (x-y)[\mathrm{Cu{-}I}] + y[\mathrm{CoCp^*_2}]^+ + y[\mathrm{I}]^- \end{aligned} \qquad (3.2)$$

3.4 Discussion

Many oxidants have been explored for introducing excess charge carriers into colloidal copper-chalcogenide nanocrystals.[2,31] To date, most descriptions of these chemistries invoke a process like the generalized description given in eq 3.3, in which an oxidant Q oxidizes Cu_2S to introduce a valence-band hole and eject a Cu^+ ion, such that the charge of each delocalized hole is compensated by one lattice cation vacancy.[29,30,46] The oxidation by I_2 studied here (eq 3.1) is an example of such a reaction. The ejected Cu^+ cations are stabilized outside of the nanocrystal by association with anions, Q^-, *e.g.*, I^- in the I_2 reaction. In *lieu* of deciphering complicated x-ray diffraction patterns, the stoichiometry of the resulting cation-deficient $Cu_{2-x}S$ lattice is often then inferred by applying the Drude model to determine the carrier density from the LSPR band, and assuming eq 3.3.

$$\mathrm{Cu_2S} + x\mathrm{Q} \rightarrow x\mathrm{h^+_{VB}}{:}\,\mathrm{Cu}_{2-x}\mathrm{S} + x\mathrm{CuQ} \qquad (3.3)$$

The results presented here demonstrate, however, that indistinguishable LSPR bands can also be generated in Cu_2S nanocrystals under conditions that are unable to stabilize ejected Cu^+ ions. Eq 3.4 describes this scenario in a generalized form, where the excess $\mathrm{h^+_{VB}}$ are compensated not by cation vacancies but instead by surface anions, A^-. Copper-chalcogenide nanocrystals have generally been considered fundamentally unstable with respect to this type of capacitive oxidative charging,[13] and LSPRs in Cu_2S nanocrystals without cation vacancies have not been identified previously. The present demonstration of capacitive chemical oxidation of Cu_2S nanocrystals, as well as recent descriptions of capacitive electrochemical reduction of $Cu_{2-x}S$ nanocrystals,[36,37] represent growing evidence of tunable copper-sulfide nanocrystal LSPR bands decoupled from structural transformation.

$$\mathrm{Cu_2S} + x[\mathrm{Q^+}][\mathrm{A^-}] \rightarrow \ x(\mathrm{h^+_{VB}}, \mathrm{A^-})\colon \mathrm{Cu_2S} + x\mathrm{Q} \qquad (3.4)$$

The redox reactions and potentiometry measurements described here are all performed on free-standing colloidal nanocrystals, and hence are not subject to the well-documented influences of nanocrystal film formation. Consequently, these measurements offer unique quantitative insights into the differences between *p*-doped copper-sulfide nanocrystals formed *via* eq 3.3 and eq 3.4. Scheme 3.1 summarizes the nanocrystal reactions explored here. The *x*-axis denotes the nanocrystal carrier density $\langle P \rangle$ and the *y*-axis represents V_{eq}, or E_{F} of the solution. The as-prepared Cu_2S nanocrystals begin at the origin of this plot, with $\langle P \rangle \sim 0$ ($\leq \sim 10^{18}$ cm^{-3}, no evident LSPR) and an equilibrium E_{F}. Upon addition of 130 equivalents of I_2, $\mathrm{h^+_{VB}}$ are introduced, $\langle P \rangle$ increases to $>10^{21}$ cm^{-3}, and E_{F} becomes more positive by ~100 mV. In this scenario, $\mathrm{h^+_{VB}}$ charges are compensated by cation vacancies (V^-_{Cu}), and the Cu^+ ions that have left the nanocrystals complex with I^- in solution (eqs 3.1, 3.3).[43] Alternatively, following eq 3.4, oxidation of the same as-prepared Cu_2S nanocrystals by an equal number of FcOTf oxidizing equivalents introduces an equal carrier density $\langle P \rangle$, as evidenced by the indistinguishable LSPR bands for the two oxidation reactions, but the resulting $\mathrm{h^+_{VB}}$ are ~300 mV less stable than those introduced *via* I_2 oxidation. This difference in carrier stability is attributed to less-effective charge compensation by surface OTf^- anions than by lattice cation vacancies. Following oxidation of the nanocrystals by FcOTf, I^- addition induces cation-vacancy formation and stabilizes $\mathrm{h}^+_{\mathrm{VB}}$, resulting in *p*-doped $\mathrm{Cu}_{2-x}\mathrm{S}$ nanocrystals that are indistinguishable from those obtained *via* direct oxidation with I_2. The data thus demonstrate that the overall $\mathrm{Cu}_{2-x}\mathrm{S}$ nanocrystal chemical transformation is pathway independent and can be equivalently executed *via* sequential stepwise oxidation and cation-vacancy formation, or by coupling these steps in a single concerted copper-coupled electron-transfer reaction. Finally, addition of CoCp^*_2 to the $\mathrm{Cu}_{2-x}\mathrm{S}$ nanocrystals in the presence of the Cu-I side product reverses the changes induced by I_2 oxidation, eliminating $\langle P \rangle$, filling cation vacancies, and lowering E_F.

Scheme 3.1. Summary of redox control over carrier density $\langle P \rangle$, cation-vacancy concentration, and Fermi level (E_F) in copper-sulfide nanocrystals.

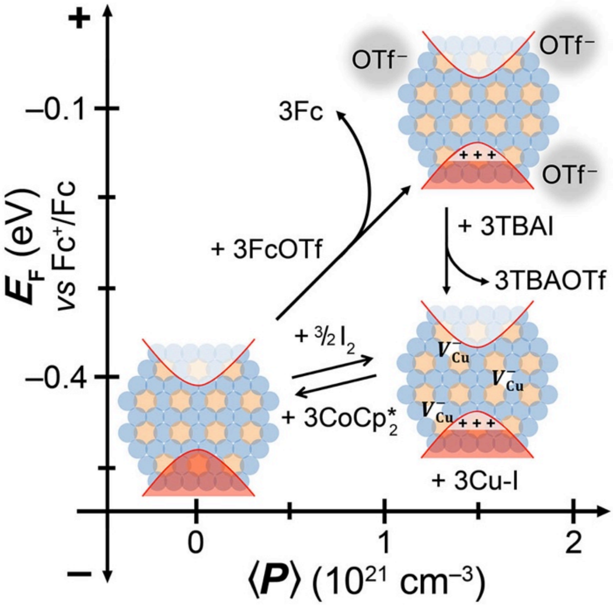

For a fixed carrier density of $\langle P \rangle \sim 1.5 \times 10^{21}$ cm^{-3}, we measure nearly 300 mV of Fermi-level stabilization by internal cation-vacancy formation relative to surface charge compensation. From this carrier density and eq 3.3, we can estimate that holes are stabilized by an average of

~2.3 mV per cation vacancy, assuming the Drude analysis of carrier density is reliable.[44] This value is consistent with those reported for Cu_2S nanocrystal arrays doped by thermal vacancy formation,[47] as well as those calculated for the transformation of stoichiometric $Cu_{32}S_{16}$ clusters into Cu^+-deficient $Cu_{30}S_{16}$ clusters.[45] The strong dependence of carrier stability on the mode of charge compensation observed here is also reminiscent of the markedly different stabilities of conduction-band electrons in *n*-type Al^{3+}:ZnO (defect doping) and photodoped ZnO (capacitive charging) nanocrystals, despite their nearly indistinguishable spectroscopic properties.[48] In both cases, internal charge compensation strongly stabilizes the excess free carriers.

Finally, it is interesting to note that Scheme 3.1 parallels one half of the well-known square schemes frequently invoked to describe proton-coupled electron-transfer (PCET) reactions in biological and synthetic systems. Such square schemes compile redox potentials and bond-dissociation free energies into a unified thermodynamic framework to quantify the impact of coupling or decoupling these two processes in a given overall reaction. In many instances, coupling proton- and electron-transfer (ET) processes avoids formation of high-energy intermediates encountered during stepwise reactions, reducing the overpotentials needed to drive the reaction at a given rate. The same principles govern electron-transfer and metal-ion-binding in so-called metal-ion-coupled electron-transfer (MCET) reactions.[49,50]

Mechanistically, the data presented here suggest that Cu_2S nanocrystal oxidation by I_2 proceeds *via* an MCET process, circumventing high-energy intermediates that would otherwise form along the stepwise reaction pathways. The stepwise and coupled pathways for the reaction of Cu_2S nanocrystals with I_2 are illustrated in the MCET square scheme of Scheme 3.2. From Scheme 3.1, stepwise oxidation (ET) followed by cation-vacancy formation (Cu^+-transfer) passes through a high-energy intermediate involving surface charge-carrier compensation, but eventually achieves the same thermodynamic endpoint as the direct MCET reaction. Similarly, the inability of I^- to induce cation vacancies in Cu_2S nanocrystals (or yield Cu-I) suggests a highly unfavorable equilibrium constant for this reaction in the absence of oxidizing equivalents, and hence a high-energy intermediate along the stepwise Cu^+-transfer/ET reaction pathway. Together, these results point to MCET as the thermodynamically favorable reaction trajectory. Furthermore, the difference in slopes for capacitive *vs* cation-vacancy-compensated charging shown in Scheme 3.1 also reflects the importance of redox-leveling by MCET, which allows injection of more carriers at any given potential. Lastly, the reverse reaction also appears to proceed along the MCET pathway when treated with an outer-sphere reductant in the presence of a Cu^+ source.

Scheme 3.2. Square scheme comparing direct copper metal-ion coupled electron transfer (MCET) with stepwise oxidation/vacancy-formation or vacancy-formation/oxidation reaction pathways in copper-sulfide nanocrystals.

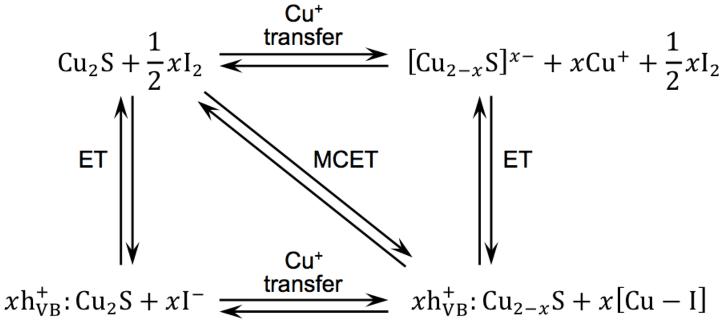

Whereas our potentiometry data yield free-carrier potentials associated with species in this square scheme, a complete thermodynamic description will additionally require knowledge of the bond-dissociation and lattice free energies involved, which at present remain uncharacterized under these conditions. Future studies will aim to quantify these parameters, motivated by the notion that a quantitative thermodynamic description of such nanocrystal reactions will enrich our understanding of this interesting chemistry and enable identification of conditions for executing such transformations at minimal driving force and hence with optimal energy efficiency, as in biological PCET. Identifying conditions that minimize the overpotentials required to drive such reactions is anticipated to be particularly relevant to tunable-plasmon technologies where reversibility and energy efficiency are paramount, for example in electrochemically driven plasmonic smart windows.

3.5 Summary & conclusions

Spectroelectrochemical potentiometry reveals and quantifies a fundamental difference between the stabilities of excess valence-band holes in colloidal copper-sulfide nanocrystals oxidized using I_2 or Fc^+. This difference reflects the different modes of charge-carrier compensation in these oxidized nanocrystals. Oxidation with I_2 yields *p*-type plasmonic $Cu_{2-x}S$ nanocrystals with h^+_{VB} charges compensated by cation vacancies, and forms Cu-I bonds as a reaction side-product. Alternatively, oxidation with FcOTf yields *p*-type plasmonic Cu_2S nanocrystals with h^+_{VB} charges compensated by OTf^- anions at the nanocrystal surfaces. Surface-compensated h^+_{VB} are hundreds of mV less stable than cation-vacancy-compensated h^+_{VB} at the same carrier density (~10^{21} cm^{-3}). Such surface-compensated holes can be stabilized by subsequent cation-vacancy formation if a suitable Cu^+-binding reagent is added. Here, stabilization was demonstrated by reacting *p*-type Cu_2S nanocrystals with I^-, which extracts Cu^+ to again form $Cu_{2-x}S$ nanocrystals, and forms Cu-I bonds as a side product. These chemical transformations are reversible: reduction using $CoCp^*_2$ not only eliminates h^+_{VB} *via* outer-sphere electron transfer but also induces dissociation of the Cu-I side-product and incorporation of that Cu^+ into the semiconductor crystallites to re-form approximately stoichiometric Cu_2S nanocrystals. Overall, these results demonstrate finely controlled chemical transformations that allow independent tuning of the carrier densities and Fermi levels in plasmonic semiconductor copper-chalcogenide nanocrystals. Beyond elucidating fundamental mechanistic aspects of these reactions, the capability to tune these two properties separately could have interesting ramifications for the use of redox-active nanocrystals in applications from electrochromism to photovoltaics.

3.6 Experimental Methods

3.6.1 General considerations. Unless otherwise specified, chemical syntheses and manipulations were performed using standard Schlenk techniques or a nitrogen-filled glovebox.

3.6.2 Chemicals. Ammonium diethyldithiocarbamate, copper acetylacetonate (97%), oleic acid (90%), dodecanthiol (≥98%), iodine (I_2, ≥99.99%), decamethylcobaltocene ($CoCp^*_2$), silver triflate (AgOTf, ≥99%), tetrabutylammonium hexafluorophosphate ($TBAPF_6$, 98%), and TBAI (98%) were purchased from Sigma-Aldrich. $TBAPF_6$ and TBAI were recrystallized prior to use. All other chemicals were used without further purification. Ferrocenium triflate (FcOTf) was prepared by reacting ferrocenium (Strem, 99%) and AgOTf in anhydrous THF and filtering through celite. Anydrous tetrahydrofuran (THF) and toluene were purified through columns of dried alumina, and anhydrous ethanol and acetonitrile (MeCN) were purchased from Acros.

3.6.3 Nanocrystal synthesis. Prepartion of stoichiometric Cu_2S nanocrystals was adapted from previously reported methods.[30] Briefly, 16 mL of oleic acid was degassed for 30 minutes at 110 °C, then cooled to room temperature, at which time 10 mL dodecanethiol was injected and 1.0 mmol ammonium diethyldithiocarbamate added under nitrogen overpressure. The reaction flask was heated under N_2 to 180 °C. In a separate flask, 1.3 mmol copper acetylacetonate and 4 mL oleic acid were degassed at least 30 minutes at 110 °C. 3.0 mL of this copper solution was injected into the other flask already at 180 °C and the temperature was maintained for 12 minutes. After cooling to room temperature, the nanocrystal solution was cannula transferred to a Schlenk flask for anaerobic purification *via* cycles of precipitation and resuspension with ethanol and toluene, respectively. Larger nanocrystals were synthesized by injecting only 1.0 mL of the copper solution and reacting at 180 °C for 15 minutes.

3.6.4 General characterization. Transmission electron miscroscope (TEM) images were obtained using a FEI Tecnai G2 F20 operating at 200 kV. Nanocrystal concentrations were determined using TEM in combination with inductively coupled plasma atomic emission spectroscopy (ICP-AES, PerkinElmer) of dried nanocrystals digested in ultrapure nitric acid. Absorption spectra were measured on Cary 500 and 5000 (Varian) spectrophotometers. Electron paramagnetic resonance (EPR) spectroscopy was measured on colloidal suspensions in toluene at room temperature on a Bruker EMX continuous wave X-band EPR spectrometer. XRD measurements were collected on a Bruker D8 Discover with a Cu anode x-ray source. XPS measurements were collected on a Surface Science Instruments S-Probe photoelectron spectrometer with a monochromatized Al Kα x-ray sources operating at 20 mA and 10 kV. Both XRD and XPS samples were prepared by maintaining the relative amounts of oxidant or reductant as in the spectroelectrochemical measurements, but more concentrated (no THF dilution) and without electrolyte to simplify analysis. Mixtures were dropcast onto silicon wafers and allowed to dry prior to measurement.

3.6.5 Potentiometry measurements. A custom air-free spectroelectrochemical cell was constructed with two 14/20 joints and three GL14 screw ports appended to the top of a quartz fluorescence cuvette. A glassy carbon working electrode, Pt wire counter electrode, and leakless Ag/AgCl reference electrode were inserted through open screw caps into each of the GL14 ports and secured with Viton o-rings. One 14/20 joint was sealed with a glass stopper and the other was capped with a rubber septum for oxidant and reductant injections. In a typical measurement, 50 μL of 50 μM $d = 5.4$ nm Cu_2S nanocrystals suspended in toluene were added to 9.0 mL of 0.1 M $TBAPF_6$ in THF. The suspension mixture was prepared and sealed in a N_2-filled glovebox. For spectroelectrochemical measurements, the cell was placed in a UV-vis-NIR spectrophotometer and connected to an Eco Chemie Autolab II or Gamry potentiostat held under galvanostatic control with $I = 0$ A. The nanocrystal solution was stirred continuously. After the open-circuit potential (V_{OC}) was allowed to equilibrate, oxidant or reductant was injected from a Hamilton gastight syringe through the septum, and absorption spectra were collected as needed. Solid I_2 and FcOTf (or $FcBF_4$) were each dissolved in THF (or MeCN) prior to experiments, and TBAI was dissolved in ethanol. All potentials are referenced to the $E_{1/2}$ of ferrocenium/ferrocene measured from cyclic voltammogram traces collected following potentiometry.

3.7 References

1. Vanmaekelbergh, D.; Liljeroth, P., Electron-Conducting Quantum Dot Solids: Novel Materials Based on Colloidal Semiconductor Nanocrystals. *Chem. Soc. Rev.* **2005,** *34*, 299-312.
2. Jain, P. K.; Manthiram, K.; Engel, J. H.; White, S. L.; Faucheaux, J. A.; Alivisatos, A. P., Doped Nanocrystals as Plasmonic Probes of Redox Chemistry. *Angew. Chem. Int. Ed.* **2013,** *52*, 13671-13675.

3. Schimpf, A. M.; Knowles, K. E.; Carroll, G. M.; Gamelin, D. R., Electronic Doping and Redox Potential Tuning in Colloidal Semiconductor Nanocrystals. *Acc. Chem. Res.* **2015,** *48*, 1929-1937.
4. Wang, Y.; Runnerstrom, E. L.; Milliron, D. J., Switchable Materials for Smart Windows. *Annu. Rev. Chem. Biomol. Eng.* **2016,** *7*, 283-304.
5. Lhuillier, E.; Guyot-Sionnest, P., Recent Progresses in Mid Infrared Nanocrystal Based Optoelectronics. *IEEE J. Sel. Top. Quant. Electr.* **2017,** *23*, 1-8.
6. Zhao, Y.; Burda, C., Development of Plasmonic Semiconductor Nanomaterials with Copper Chalcogenides for a Future with Sustainable Energy Materials. *Energy Environ. Sci.* **2012,** *5*, 5564-5576.
7. Routzahn, A. L.; White, S. L.; Fong, L.-K.; Jain, P. K., Plasmonics with Doped Quantum Dots. *Israel J. Chem.* **2012,** *52*, 983-991.
8. Scotognella, F.; Valle, G.; Srimath Kandada, A.; Zavelani-Rossi, M.; Longhi, S.; Lanzani, G.; Tassone, F., Plasmonics in Heavily-Doped Semiconductor Nanocrystals. *Eur. Phys. J. B* **2013,** *86*, 1-13.
9. Comin, A.; Manna, L., New Materials for Tunable Plasmonic Colloidal Nanocrystals. *Chem. Soc. Rev.* **2014,** *43*, 3957-3975.
10. Schimpf, A. M.; Thakkar, N.; Gunthardt, C. E.; Masiello, D. J.; Gamelin, D. R., Charge-Tunable Quantum Plasmons in Colloidal Semiconductor Nanocrystals. *ACS Nano* **2014,** *8*, 1065-1072.
11. van der Stam, W.; Berends, A. C.; de Mello Donega, C., Prospects of Colloidal Copper Chalcogenide Nanocrystals. *Chem. Phys. Chem.* **2016,** *17*, 559-581.
12. Agrawal, A.; Johns, R. W.; Milliron, D. J., Control of Localized Surface Plasmon Resonances in Metal Oxide Nanocrystals. *Annu. Rev. Mater. Res.* **2017,** *47*, 1-31.
13. Kriegel, I.; Scotognella, F.; Manna, L., Plasmonic Doped Semiconductor Nanocrystals: Properties, Fabrication, Applications and Perspectives. *Phys. Rep.* **2017,** *674*, 1-52.
14. Liu, Y.; Liu, M.; Swihart, M. T., Plasmonic Copper Sulfide-Based Materials: A Brief Introduction to Their Synthesis, Doping, Alloying, and Applications. *J. Phys. Chem. C* **2017,** *121*, 13435-13447.
15. Nütz, T.; zum Felde, U.; Haase, M., Wet-Chemical Synthesis of Doped Nanoparticles: Blue-Colored Colloids of *n*-Doped SnO_2:Sb. *J. Chem. Phys.* **1999,** *110*, 12142-12150.
16. Buonsanti, R.; Llordes, A.; Aloni, S.; Helms, B.; Milliron, D., Tunable Infrared Absorption and Visible Transparency of Colloidal Aluminum-Doped Zinc Oxide Nanocrystals. *Nano Lett.* **2011,** *11*, 4706-4716.
17. Fang, H.; Hegde, M.; Yin, P.; Radovanovic, P. V., Tuning Plasmon Resonance of In_2O_3 Nanocrystals Throughout the Mid-Infrared Region by Competition between Electron Activation and Trapping. *Chem. Mater.* **2017,** *29*, 4970-4979.
18. Pradhan, N.; Adhikari, S. D.; Nag, A.; Sarma, D. D., Luminescence, Plasmonic, and Magnetic Properties of Doped Semiconductor Nanocrystals. *Angew. Chem. Int. Ed.* **2017,** *56*, 7038-7054.
19. Haase, M.; Weller, H.; Henglein, A., Photochemistry and Radiation Chemistry of Colloidal Semiconductors. 23. Electron Storage on ZnO Particles and Size Quantization. *J. Phys. Chem.* **1988,** *92*, 482-487.
20. Shim, M.; Guyot-Sionnest, P., *n*-Type Colloidal Semiconductor Nanocrystals. *Nature* **2000,** *407*, 981-983.

21. Wood, A.; Giersig, M.; Mulvaney, P., Fermi Level Equilibration in Quantum Dot-Metal Nanojunctions. *J. Phys. Chem. B* **2001,** *105*, 8810-8815.
22. Wang, C.; Shim, M.; Guyot-Sionnest, P., Electrochromic Nanocrystal Quantum Dots. *Science* **2001,** *291*, 2390-2392.
23. Germeau, A.; Roest, A. L.; Vanmaekelbergh, D.; Allan, G.; Delerue, C.; Meulenkamp, E. A., Optical Transitions in Artificial Few-Electron Atoms Strongly Confined Inside ZnO Nanocrystals. *Phys. Rev. Lett.* **2003,** *90*, 097401.
24. Liu, W. K.; Whitaker, K. M.; Smith, A. L.; Kittilstved, K. R.; Robinson, B. H.; Gamelin, D. R., Room-Temperature Electron Spin Dynamics in Free-Standing ZnO Quantum Dots. *Phys. Rev. Lett.* **2007,** *98*, 186804.
25. Garcia, G.; Buonsanti, R.; Runnerstrom, E. L.; Mendelsberg, R. J.; Llordes, A.; Anders, A.; Richardson, T. J.; Milliron, D. J., Dynamically Modulating the Surface Plasmon Resonance of Doped Semiconductor Nanocrystals. *Nano Lett.* **2011,** *11*, 4415-4420.
26. Niezgoda, J. S.; Harrison, M. A.; McBride, J. R.; Rosenthal, S. J., Novel Synthesis of Chalcopyrite $Cu_xIn_yS_2$ Quantum Dots with Tunable Localized Surface Plasmon Resonances. *Chem. Mater.* **2012,** *24*, 3294-3297.
27. Palomaki, P. K. B.; Miller, E. M.; Neale, N. R., Control of Plasmonic and Interband Transitions in Colloidal Indium Nitride Nanocrystals. *J. Am. Chem. Soc.* **2013,** *135*, 14142-14150.
28. Liu, Z.; Beaulac, R., Nature of the Infrared Transition of Colloidal Indium Nitride Nanocrystals: Nonparabolicity Effects on the Plasmonic Behavior of Doped Semiconductor Nanomaterials. *Chem. Mater.* **2017,** *29*, 7507-7514.
29. Zhao, Y.; Pan, H.; Lou, Y.; Qiu, X.; Zhu, J.; Burda, C., Plasmonic $Cu_{2-x}S$ Nanocrystals: Optical and Structural Properties of Copper-Deficient Copper(I) Sulfides. *J. Am. Chem. Soc.* **2009,** *131*, 4253-4261.
30. Luther, J. M.; Jain, P. K.; Ewers, T.; Alivisatos, A. P., Localized Surface Plasmon Resonances Arising from Free Carriers in Doped Quantum Dots. *Nat. Mater.* **2011,** *10*, 361-366.
31. Dorfs, D.; Härtling, T.; Miszta, K.; Bigall, N. C.; Kim, M. R.; Genovese, A.; Falqui, A.; Povia, M.; Manna, L., Reversible Tunability of the Near-Infrared Valence Band Plasmon Resonance in $Cu_{2-x}Se$ Nanocrystals. *J. Am. Chem. Soc.* **2011,** *133*, 11175-11180.
32. Kriegel, I.; Jiang, C.; Rodríguez-Fernández, J.; Schaller, R. D.; Talapin, D. V.; da Como, E.; Feldmann, J., Tuning the Excitonic and Plasmonic Properties of Copper Chalcogenide Nanocrystals. *J. Am. Chem. Soc.* **2011,** *134*, 1583-1590.
33. Coughlan, C.; Ibáñez, M.; Dobrozhan, O.; Singh, A.; Cabot, A.; Ryan, K. M., Compound Copper Chalcogenide Nanocrystals. *Chem. Rev.* **2017,** *117*, 5865-6109.
34. Alam, R.; Labine, M.; Karwacki, C. J.; Kamat, P. V., Modulation of $Cu_{2-x}S$ Nanocrystal Plasmon Resonance through Reversible Photoinduced Electron Transfer. *ACS Nano* **2016,** *10*, 2880-2886.
35. Asami, K.; Nishi, H.; Tatsuma, T., Electrochemical Redox-Based Tuning of Near Infrared Localized Plasmons of CuS Nanoplates. *Nanoscale* **2016,** *8*, 14092-14096.
36. van der Stam, W.; Gudjonsdottir, S.; Evers, W. H.; Houtepen, A. J., Switching between Plasmonic and Fluorescent Copper Sulfide Nanocrystals. *J. Am. Chem. Soc.* **2017,** *139*, 13208-13217.

37. Llorente, V. B.; Dzhagan, V. M.; Gaponik, N.; Iglesias, R. A.; Zahn, D. R. T.; Lesnyak, V., Electrochemical Tuning of Localized Surface Plasmon Resonance in Copper Chalcogenide Nanocrystals. *J. Phys. Chem. C* **2017,** *121*, 18244-18253.
38. Vinokurov, K.; Elimelech, O.; Millo, O.; Banin, U., Copper Sulfide Nanocrystal Level Structure and Electrochemical Functionality towards Sensing Applications. *Chem. Phys. Chem.* **2016,** *17*, 675-680.
39. Boehme, S. C.; Wang, H.; Siebbeles, L. D. A.; Vanmaekelbergh, D.; Houtepen, A. J., Electrochemical Charging of CdSe Quantum Dot Films: Dependence on Void Size and Counterion Proximity. *ACS Nano* **2013,** *7*, 2500-2508.
40. Carroll, G. M.; Brozek, C. K.; Hartstein, K. H.; Tsui, E. Y.; Gamelin, D. R., Potentiometric Measurements of Semiconductor Nanocrystal Redox Potentials. *J. Am. Chem. Soc.* **2016,** *138*, 4310-4313.
41. Carroll, G. M.; Tsui, E. Y.; Brozek, C. K.; Gamelin, D. R., Spectroelectrochemical Measurement of Surface Electrostatic Contributions to Colloidal CdSe Nanocrystal Redox Potentials. *Chem. Mater.* **2016,** *28*, 7912-7918.
42. Brozek, C. K.; Hartstein, K. H.; Gamelin, D. R., Potentiometric Titrations for Measuring the Capacitance of Colloidal Photodoped ZnO Nanocrystals. *J. Am. Chem. Soc.* **2016,** *138*, 10605-10610.
43. Elimelech, O.; Liu, J.; Plonka, A. M.; Frenkel, A. I.; Banin, U., Size Dependence of Doping *via* Vacancy Formation in Copper Sulfide Nanocrystals. *Angew. Chem. Int. Ed.* **2017,** *56*, 10335-10340.
44. We note that using the Nernst equation, the value of V_{eq} in Figure 3.4B for the reaction with Fc^+ indicates essentially complete (~98%) reduction of Fc^+ to Fc in this reaction. Similarly, no detectable I_2 absorption remains at the end of the reaction with I_2, suggesting essentially complete consumption of I_2. When combined with the carrier densities estimated from the Drude analysis, however, these results would imply only ~50% conversion of added oxidizing equivalents into valence-band holes, with the remaining 50% lost to some unidentified reductant. Such a scenario appears improbable, given that these two very different oxidants both yield identical nanocrystal carrier densities when added in the same amount. This discrepancy could conceivably come from a factor-of-two error in the carrier densities estimated from the Drude analysis of the LSPR band. For example, in small ZnO nanocrystals the same Drude analysis overestimates carrier densities by up to a factor of four because it neglects quantum-size effects (ref 10). The Drude analysis also relies on knowledge of the carrier effective mass, m^*, which is typically assumed to be the same in nanocrystals as in bulk; recent spectroscopic measurements have suggested that m^* may be greater in copper-chalcogenide nanocrystals than in their bulk counterparts (ref 51), however. At present, we are unable to conclude whether half of all added oxidizing equivalents are consumed elswhere or the actual nanocrystal carrier densities are two times greater than estimated by the Drude analysis.
45. Lukashev, P.; Lambrecht, W. R. L.; Kotani, T.; van Schilfgaarde, M., Electronic and Crystal Structure of $Cu_{2-x}S$: Full-Potential Electronic Structure Calculations. *Phys. Rev. B* **2007,** *76*, 195202.
46. Xie, Y.; Riedinger, A.; Prato, M.; Casu, A.; Genovese, A.; Guardia, P.; Sottini, S.; Sangregorio, C.; Miszta, K.; Ghosh, S.; Pellegrino, T.; Manna, L., Copper Sulfide Nanocrystals with Tunable Composition by Reduction of Covellite Nanocrystals with Cu^+ Ions. *J. Am. Chem. Soc.* **2013,** *135*, 17630-17637.

47. Bekenstein, Y.; Vinokurov, K.; Keren-Zur, S.; Hadar, I.; Schilt, Y.; Raviv, U.; Millo, O.; Banin, U., Thermal Doping by Vacancy Formation in Copper Sulfide Nanocrystal Arrays. *Nano Lett.* **2014,** *14*, 1349-1353.
48. Schimpf, A. M.; Ochsenbein, S. T.; Buonsanti, R.; Milliron, D. J.; Gamelin, D. R., Comparison of Extra Electrons in Colloidal *n*-Type Al^{3+}-Doped and Photochemically Reduced ZnO Nanocrystals. *Chem. Commun.* **2012,** *48*, 9352-9354.
49. Fukuzumi, S.; Ohkubo, K., Metal Ion-Coupled and Decoupled Electron Transfer. *Coord. Chem. Rev.* **2010,** *254*, 372-385.
50. Fukuzumi, S.; Ohkubo, K.; Morimoto, Y., Mechanisms of Metal Ion-Coupled Electron Transfer. *Phys. Chem. Chem. Phys.* **2012,** *14*, 8472-8484.
51. Hartstein, K. H.; Schimpf, A. M.; Salvador, M.; Gamelin, D. R. Cyclotron Splittings in the Plasmon Resonances of Electronically Doped Semiconductor Nanocrystals Probed by Magnetic Circular Dichroism Spectroscopy. *J. Phys. Chem. Lett.* **2017**, *8,* 1831-1836.

Chapter 4: Cyclotron Splittings in the Plasmon Resonances of Degenerately Doped Semiconductor Nanocrystals Probed by Magnetic Circular Dichroism Spectroscopy

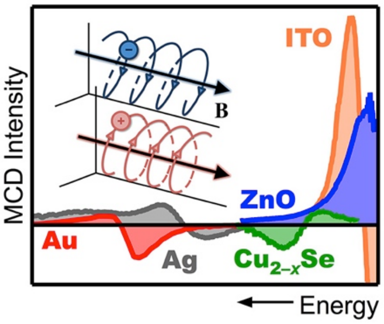

Reproduced with permission from:
Hartstein, K. H.; Schimpf, A. M.; Salvador, M.; Gamelin, D. R. *J. Phys. Chem. Lett.* **2017**, *8*, 1831–1836.

4.1 Overview

A fundamental understanding of the rich electronic structures of electronically doped semiconductor nanocrystals is vital for assessing the utility of these materials for future applications from solar cells to redox catalysis. Here, we examine the use of magnetic circular dichroism (MCD) spectroscopy to probe the infrared localized surface plasmon resonances of *p*-$Cu_{2-x}Se$, *n*-ZnO, and tin-doped In_2O_3 (*n*-ITO) nanocrystals. We demonstrate that the MCD spectra of these nanocrystals can be analyzed by invoking classical cyclotron motions of their excess charge carriers, with experimental MCD signs conveying the carrier types (*n* or *p*) and experimental MCD intensities conveying the cyclotron splitting magnitudes. The experimental cyclotron splittings can then be used to quantify carrier effective masses (m^*), with results that agree with bulk in most cases. MCD spectroscopy thus offers a unique measure of m^* in free-standing colloidal semiconductor nanocrystals, raising new opportunities to investigate the influence of various other synthetic or environmental parameters on this fundamentally important electronic property.

4.2 Introduction

Materials that display strong coupling between their electronic properties and external magnetic fields are attractive for many potential computing and data storage technologies.[1] When combined with optical read or write capabilities, such materials introduce mechanisms for magnetic control of photons, such as in Faraday optical isolators used in optical telecommunications, and they may additionally enable sophisticated spin-photonic information processing technologies based on information transfer between photon and spin degrees of freedom. Degenerately doped colloidal semiconductor nanocrystals (*i.e.*, those possessing excess band-like charge carriers) represent an emerging class of electronic materials,[2] displaying tunable infrared (IR) localized surface plasmon resonances (LSPRs),[3,4] solution processability, and a variety of unusual spectroscopic, photophysical, chemical, and electronic characteristics.[2,4-18] Because of these diverse properties, degenerately doped semiconductor nanocrystals are attracting broad interest for both fundamental and applied sciences.[3,4,19] The same properties also make these nanocrystals unusual new materials for fundamental magneto-optical investigations.

In bulk or 2-D materials, application of an external magnetic field can induce cyclotron motion of free charge carriers, and narrow transitions among Landau levels (cyclotron resonances) can be detected whose energies reveal the carrier effective masses, m^*. In nanocrystals, surface scattering can severely broaden such transitions, making them no longer resolvable. Indeed, colloidal semiconductor nanocrystals are typically small enough that their scattering frequencies rival or exceed their cyclotron frequencies at common laboratory magnetic fields, *i.e.*, carriers cannot complete a cyclotron orbit without scattering. For example, the classical cylotron radius in a colloidal *n*-ZnO nanocrystal, with typical radii of $r \sim 1.5 - 4.0$ nm, is estimated to be $r_c \sim 10$ nm at a magnetic-field strength of 1 T (see Appendix C). Scattering thus obscures the cyclotron resonances of degenerately doped colloidal semiconductor nanocrystals.

As a difference technique, magnetic circular dichroism (MCD) spectroscopy can facilitate detection of small magnetic splittings that are difficult to observe by more standard linear methods. For example, this technique has long served as a powerful probe of excitonic Zeeman splittings in colloidal doped semiconductor nanocrystals.[20] Here, we examine the MCD spectroscopy of a series of colloidal plasmonic nanomaterials, with emphasis on colloidal degenerately doped semiconductor nanocrystals. We demonstrate that analysis of the LSPR MCD spectra of p-$Cu_{2-x}Se$, n-ZnO, and n-$Sn^{4+}:In_2O_3$ (ITO) nanocrystals, as well as of plasmonic Au and Ag nanoparticles, within a classical cyclotron model allows quantification of their free-carrier effective masses m^*, thereby providing a uniquely direct experimental measure of this important electronic parameter in colloidal nanostructures.

4.3 Results & discussion

We have recently reported phenomenological observations of strong, temperature-independent (non-Curie) MCD intensities arising from the near-infrared (NIR) bands of colloidal *n*-type ZnO and ITO semiconductor nanocrystals,[21,22] but to date there has been no clear interpretation of this anomalous MCD response, nor has there been any systematic investigation of degenerately doped semiconductor nanocrystals by magneto-optical techniques in general. Figure 4.1 summarizes all IR MCD spectra of heavily doped colloidal semiconductor nanocrystals collected to date (see Experimental methods). To our knowledge, LSPR MCD spectra have not been reported previously for any nanocrystalline or bulk p-$Cu_{2-x}Se$ samples. MCD spectra of *n*-ZnO and *n*-ITO nanocrystals were reported in our previous descriptions of the redox chemistries of these two materials,[21,22] but could not be analyzed. In Figure 4.1, these spectra are all compared quantitatively, with the *y*-axis describing the dichroism per unit Tesla. For comparison, the MCD spectra of Au nanoparticles (reproduced from ref. 23) and Ag nanoprisms (collected here, see Appendix C) are also included. Additional MCD data are provided in Appendix C.

Although each of these nanostructures displays a unique MCD spectrum, all are characterized by a derivative-shaped MCD signal centered close to the maximum of the corresponding absorption feature (Figure 4.1, inset). Furthermore, the *n*-ZnO, *n*-ITO, Ag, and Au spectra all show negative leading-edge MCD intensities, whereas the *p*-$Cu_{2-x}Se$ nanocrystal MCD signal has a sign that is inverted relative to all of the other spectra in Figure 4.1. We note that each of these nanostructures is pseudo-spherical except the Ag nanoparticles, which are prismatic, and the *p*-$Cu_{2-x}Se$ nanocrystals, which are thin hexagonal (or pseudo-cylindrical) nanoplatelets with diameter ~16.9 nm and an estimated thickness of ~2–4 nm[24,25] (see Appendix C).

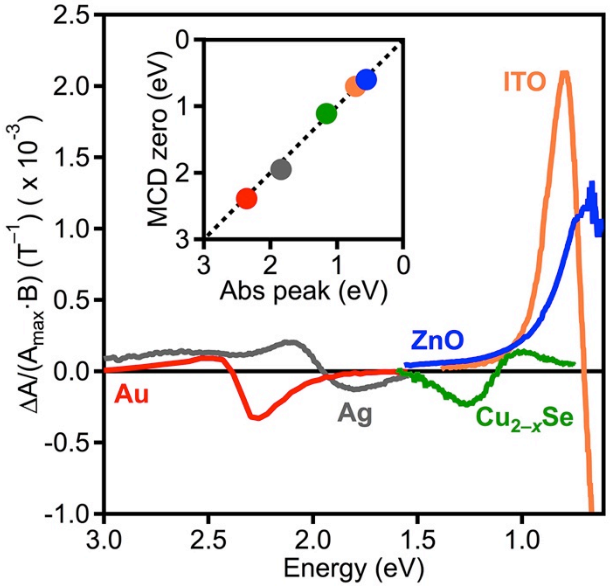

Figure 4.1. MCD spectra in the free-carrier absorption regions of *n*-ZnO (d = 3.1 nm, <N> ~ 1.4 × 10^{20} cm^{-3}), *n*-ITO (d = 5.5 nm, <N> ~ 6 × 10^{20} cm^{-3}), *p*-$Cu_{2-x}Se$ (platelets, d = 16.9 nm, <P> ~ 2 × 10^{21} cm^{-3}) nanocrystals and the LSPR regions of Ag (prisms, d ~ 50 nm) and Au (d = 12.8 nm) nanoparticles, plotted as $\Delta A/A_{max}$ per unit Tesla. All data were collected at room temperature except *n*-ITO, which was measured at 1.6 K but has been shown to be temperature independent.[22] Data below ~0.6 eV were not recorded because of instrumental limitations. Spectra of *n*-ZnO nanocrystals,[21] *n*-ITO nanocrystals,[22] and Au nanoparticles[23] are reproduced from previous reports. Carrier densities in *n*-ZnO and *n*-ITO were determined experimentally by chemical titration as reported previously,[21,22] and in *p*-$Cu_{2-x}Se$ were estimated from the LSPR spectrum and bulk effective masses, assuming Drude behavior. Inset: MCD crossover energies plotted *vs* absorption peak energies. The dotted line is a guide to the eye with a slope of 1, showing that these energies track one another.

To interpret these LSPR MCD spectra, we consider the action of the external magnetic and electric fields on free carriers within these nanocrystals.[23,26,27] Classically, a carrier of charge q experiences Lorentz forces when exposed to external electric (**E**) and magnetic (**B**) fields, as described by eq 4.1 and illustrated schematically in Figure 4.2.

$$\mathbf{F} = \mathbf{F_E} + \mathbf{F_B} = q\mathbf{E} + q(\mathbf{v} \times \mathbf{B}) \tag{4.1}$$

Circularly polarized light (σ^+ and σ^-) introduces an electric Lorentz force ($\mathbf{F_E}$) that induces circular charge motion at an angular frequency equal to that of the incoming light, with opposite circular polarizations inducing charge motion in opposite directions. At zero applied magnetic field, these two circular excitation modes have equal resonance frequencies, ω_0. In the presence of an applied magnetic field co-linear with the light-propagation axis, however, charge traveling with velocity **v** will experience a magnetic Lorentz force ($\mathbf{F_B}$) that induces motion perpendicular to both **v** and **B**, and hence in the plane of **E**. $\mathbf{F_B}$ either supports or opposes $\mathbf{F_E}$, thus shifting the circular excitation resonance to either higher or lower frequency, depending on the relative directions of $\mathbf{F_B}$ and $\mathbf{F_E}$. Within this model, two separate circular excitation resonances are therefore anticipated in a magnetic field,[28] at frequencies ($\omega_{\mathrm{B}}^{\pm}$) defined by the classical cyclotron conditions described in eq 4.2.

$$\omega_{\mathrm{B}}^{\pm} = \omega_0 \pm \frac{qB}{2m^*} = \omega_0 \pm \frac{\omega_{\mathrm{c}}}{2} \tag{4.2}$$

Here, B is a scalar representing the intensity of the magnetic field, m^* is the effective mass of the mobile charge carrier, and ω_{c} is the carrier's classical cyclotron frequency. Because one of these resonances is selective for σ^+ light and the other for σ^- light, MCD spectra show a derivative-shaped response centered at ω_0 whose intensity is a function of $\omega_{\mathrm{c}} = qB/m^*$ and the absorption bandshape.

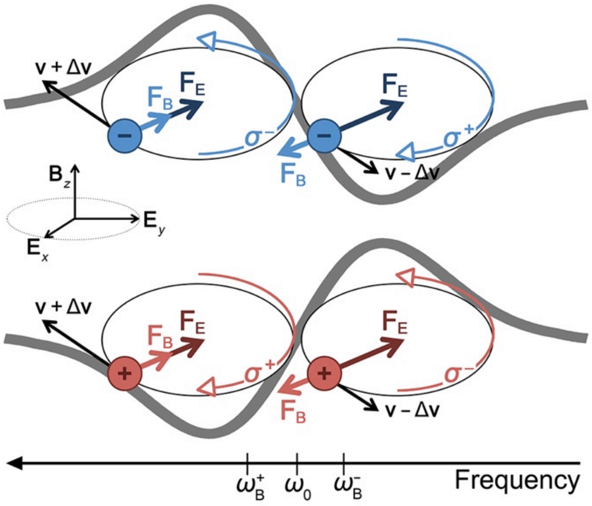

Figure 4.2. Classical depiction of cyclotron-derived MCD signals for *n*-type (e^-) and *p*-type (h^+) charge carriers. Quadrants demonstrate the effects of σ^+ and σ^- light (curved arrows) on the respective charge carriers as specified. Elliptical paths indicate the classical motion of the charge carrier traveling with velocity $\mathbf{v} \pm \Delta\mathbf{v}$ in the *xy* plane as induced by the electric and magnetic components of the electromagnetic Lorentz forces (arrows labeled $\mathbf{F_E}$ and $\mathbf{F_B}$, respectively). Force vectors pointing in the same (opposite) direction indicate ω_B shifted to higher (lower) angular frequency relative to ω_0. Taking the difference between these modes according to the convention $\Delta A = A_L - A_R$ yields a derivative-shaped MCD signal (grey curves) whose intensity reflects the magnitude of ω_c and whose sign reflects the sign of q.

With opposite signs of q in eq 4.2, conduction-band electrons (e^-_{CB}) and valence-band holes (h^+_{VB}) subjected to identical electric fields will move in opposite directions. Alternatively, $\mathbf{F_B}$ acts in the same direction regardless of the charge's sign, because the direction of **v** also reverses with a change in the charge's sign, analogous to Hall-effect experiments in which e^-_{CB} and h^+_{VB} travel in opposite directions.[29] If $\mathbf{F_E}$ and $\mathbf{F_B}$ point in the same direction when $q > 0$, then they will oppose one another when $q < 0$ under identical external conditions, and *vice versa*. Overall, eq 4.2 therefore indicates that the *sign* of q dictates the sign of the derivative-shaped MCD response in this model, as illustrated in Figure 4.2. This aspect of the model is confirmed experimentally in Figure 4.1 by the MCD sign inversion between *n*-type (ZnO, ITO) and *p*-type ($Cu_{2-x}Se$) IR

MCD signals. Interestingly, the LSPRs of Ag and Au nanoparticles show *negative* MCD features at lowest energy, indicative of *negatively* charged mobile carriers (electrons) in these nanoparticles. This result is consistent with Hall-effect measurements on both Ag and Au films, which show electrons as the mobile charge carriers.[30] These results lend credence to the hypothesis that the MCD intensities associated with the LSPRs of degenerately doped semiconductor nanocrystals derive from cyclotron splittings.

As noted previously,[21,22] a peculiar characteristic of the MCD spectra of *n*-ZnO and *n*-ITO nanocrystals is that their LSPR MCD intensities are temperature independent from room temperature down to liquid-helium temperatures, and they increase linearly with increasing magnetic field at all temperatures, *i.e.*, they show no indication of magnetic saturation. These MCD spectra thus show none of the signatures of ground-state Curie paramagnetism, even though the same *n*-ZnO nanocrystals in particular show a pronounced $g \approx 1.96$ electron paramagnetic resonance (EPR) signal in their ground state, whose intensity is temperature dependent.[18,31] Similar temperature independence has been observed[32] in the MCD intensities of Au nanoparticles.[33] We also find the LSPR MCD intensities of Ag nanoparticles to be independent of temperature (see Appendix C), and Ag nanoparticle LSPR MCD intensities have been reported to exhibit a linear field dependence at low temperature.[35] These two properties (temperature independence and non-saturation) thus appear to be characteristic of the LSPR MCD of free carriers in metallic or, as shown here, semi-metallic systems. Again, these results are consistent with interpretation of the LSPR MCD signals of degenerately doped semiconductor nanocrystals as dominated by cyclotron splittings.

To test more quantitatively the applicability of the cyclotron splitting model for interpretation of the LSPR MCD intensities of *n*-ZnO, *n*-ITO, and *p*-$Cu_{2-x}Se$ nanocrystals, the MCD spectra shown in Figure 4.1 were simulated to extract values of ω_c. Although LSPR band shapes of many metal nanoparticles and doped semiconductor nanocrystals have been successfully modeled,[23,36] any discrepancy between calculated and experimental LSPR band shapes would translate into large artifacts in MCD spectra simulated from these band shapes because differences are amplified in this technique. We therefore simulate our MCD spectra using the experimental LSPR linear absorption spectra as input, applying the rigid-shift approximation, *i.e.*, the assumption that the σ^+ and σ^- LSPR band shapes are independent of magnetic field within our experimental field range. We then generate simulated MCD spectra by splitting the zero-field absorption profiles into two components, with one shifted to higher energy (ω_{B}^{+}) and the other shifted to lower (ω_{B}^{-}) energy and taking the difference between them in accordance with the signs established in Figure 4.2. In this way, the experimental MCD spectra of the doped nanocrystals can be simulated by least squares fitting with ω_c as the only adjustable variable (see Appendix C). Figure 4.3 shows simulated MCD spectra (dashed) of the *n*-ZnO, *n*-ITO, and *p*-$\mathrm{Cu}_{2-x}\mathrm{Se}$ nanocrystals from Figure 4.1, in comparison with the experimental LSPR absorption and MCD spectra (solid), all plotted on quantitative intensity scales.

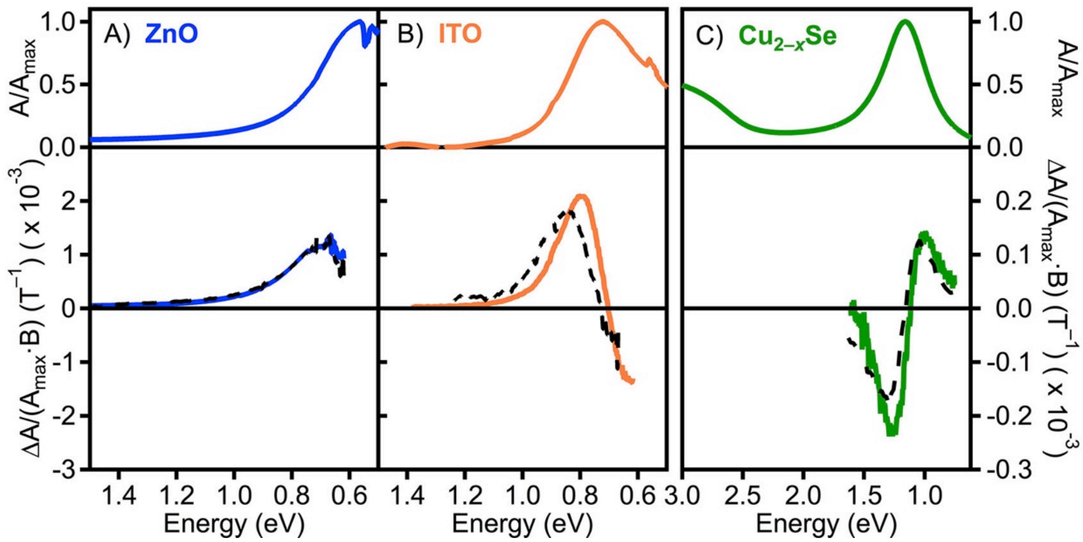

Figure 4.3. Simulated MCD spectra (dashed) of (**A**) *n*-ZnO, (**B**) *n*-ITO, and (**C**) *p*-$Cu_{2-x}Se$ nanocrystals, plotted in comparison with the corresponding experimental absorption and MCD spectra from Figure 4.1 (solid). All data were collected at room temperature except the *n*-ITO MCD spectrum (1.6 K), which shows no temperature dependence.[22] Note that the MCD spectra in panels (A) and (B) are plotted on a scale that is one order of magnitude greater than that used for panel (C). Panels (A) and (B) also have different *x* axes from panel (C).

Figure 4.4 plots values of $\hbar\omega_c/B$ obtained from this analysis *vs* literature (bulk) m^* values[36-44] for the same semiconductors. The dashed curve in Figure 4.4 plots $\hbar\omega_c/B$ as a function of m^* as predicted by eq 4.2 for a classical cyclotron. The error bars on the *x*-axis reflect the range of (bulk) m^* values found in literature, and those on the *y*-axis indicate a margin of ±20% of the integrated least-squares fitting residuals (see Appendix C), except for the *p*-$Cu_{2-x}Se$ nanocrystal error bars, which represent the uncertainty estimated from MCD measurements on multiple samples. Note that the *y*-axis uncertainties are generally smaller than those of the *x*-axis. The experimental LSPR splitting energies for all of these colloidal semiconductor nanocrystals determined by analysis of these MCD spectra agree remarkably well with the splittings predicted based on the classical cyclotron description and the corresponding literature bulk values of m^*.

For context, in addition to data for the three doped semiconductor nanocrystals, we also plot in Figure 4.4 the value obtained from the same analysis of the MCD spectrum of the Ag nanoparticles shown in Figure 4.1, a data point from analysis of the literature MCD spectrum of Au nanoparticles (Figure 4.1),[23] and yet another data point obtained from literature Faraday rotation measurements of 2-D monolayers of *p*-type graphene.[45] Despite an order of magnitude range in literature m^*, the MCD splittings of all of these materials map onto the same universal cyclotron-splitting curve predicted by eq 4.2, validating application of this classical cyclotron model across the entire series of nanomaterials.

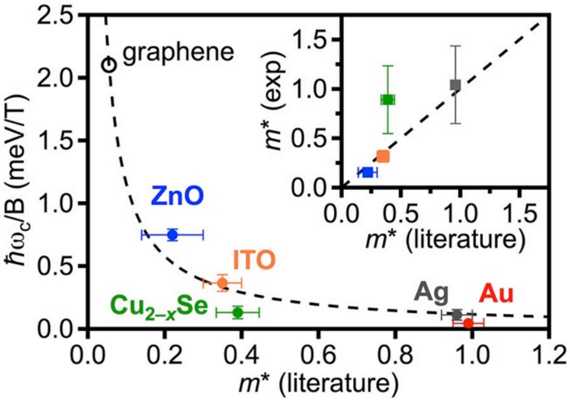

Figure 4.4. Experimental field-normalized cyclotron splitting energies ($\hbar\omega_c/B$) plotted *vs* literature (bulk) carrier effective masses (m^*) for *p*-$Cu_{2-x}Se$, *n*-ZnO, and *n*-ITO nanocrystals and Au, Ag nanoparticles, as obtained from analysis of MCD intensities. The open circle represents the result for *p*-type monolayer graphene ($<P> \sim 8 \times 10^{12}$ cm^{-2}) obtained from Faraday rotation measurements.[45] The dashed curve shows the trend for free carriers predicted by eq 4.2. Inset: Experimental m^* values for *p*-$Cu_{2-x}Se$, *n*-ZnO, *n*-ITO, and Ag nanocrystals determined by MCD spectroscopy using eq 4.2, plotted as a function of literature (bulk) m^* values.[36-44] The dashed line has a slope of unity.

We note that $\hbar\omega_c/B$ for the p-Cu$_{2-x}$Se nanocrystals estimated from this MCD analysis appears to be slightly smaller than expected from the values of m^* reported for bulk non-stoichiometric Cu$_{2-x}$Se,[37,38] their difference being beyond our estimated experimental uncertainty range. The inset to Figure 4.4 replots the same data now as m^*(MCD) *vs* m^*(lit), using the conversion $m^* = qB/\omega_c$. This plot highlights the finding that m^*(MCD) for the p-Cu$_{2-x}$Se nanocrystals is approximately a factor of two greater than anticipated. At this time, it is unclear whether this discrepancy is real and m^* is truly greater in the Cu$_{2-x}$Se nanocrystals than in bulk, or if it comes from some yet-unidentified source of error. Prior nanocrystal literature is also not uniformly in agreement on the question of m^* in such nanocrystals. For example, a recent report[46] has suggested partial localization (and greater m^*) of excess holes in non-stoichiometric colloidal Cu$_{2-x}$E (E = S, Se, Te) nanocrystals, based on a very weak dependence of their LSPR line shapes and positions on nanocrystal shape. At the same time, distinct in- and out-of-plane LSPR modes have been identified in colloidal Cu$_{2-x}$S nanodisks,[47] with relative energies tunable *via* crystal aspect ratio as might be expected from bulk-like m^* values.[48] TEM images (see Appendix C) show that our p-Cu$_{2-x}$Se nanocrystals are also disk-like. Moreover, it is known that various compositional and structural parameters can impact m^* even in bulk p-Cu$_{2-x}$Se. For example, m^* in bulk Cu$_{2-x}$Se depends upon carrier density, reaching values in excess of $m^* = 1$ in stoichiometric Cu$_2$Se,[38] and m^* may itself be anisotropic in this material. Such variations in m^* for Cu$_{2-x}$Se nanocrystals are not independently known. Reflectance measurements on bulk Cu$_{2-x}$Se films suggest a temperature-dependence of m^* at T > 300 K, attributed to the complex valence-band structure and potential polymorphic transitions,[38] but this temperature dependence was not observed in LSPR dephasing experiments on colloidal Cu$_{2-x}$Se nanocrystals.[49] In our observations, the MCD intensities of our p-Cu$_{2-x}$Se nanocrystals are temperature independent and linearly dependent on magnetic field at all experimental temperatures (see Appendix C), consistent with a constant value of m^* under these conditions. In light of the existing literature discrepancies for this complex material, the conclusion here that MCD spectroscopy of plasmonic nanocrystals can provide a direct measure of m^* suggests that a more focused follow-up investigation specifically addressing the size, shape, and carrier-density dependence of m^* in $Cu_{2-x}E$ nanocrystals using MCD spectroscopy may be feasible and informative. Such experiments are presently being initiated.

Finally, it is noteworthy that the experimental cyclotron splittings of the heavily doped *n*-ZnO nanocrystals ($\hbar\omega_c \approx 0.8$ meV @ 1 T) obtained from the LSPR MCD analysis are much larger than the ground-state splittings for the same conduction-band electrons measured by EPR spectroscopy (~0.1 meV @ 1 T, from $\hbar\omega = g\mu_B B$ and $g \approx 1.96$[31,50]). This observation emphasizes the role of MCD spectroscopy as an excited-state technique in this instance, and highlights the existence of considerable orbital angular momentum in the IR excited states of degenerately doped colloidal semiconductor nanocrystals.

4.4 Summary & conclusions

In summary, IR MCD spectroscopy of degenerately doped semiconductor nanocrystals reveals magneto-optical splittings consistent with classical cyclotron motion of the excess charge carriers within these nanocrystals. Due to surface scattering, the cyclotron splittings are much smaller than the associated LSPR band widths and hence are not observable by linear absorption spectroscopy, but they are readily detected and quantified using MCD spectroscopy. A series of *n*- and *p*-doped semiconductor nanocrystals has been analyzed that all show derivative-shaped IR MCD signals but with signs that reflect the charges of their excess carriers. Quantitative analysis of the IR MCD intensities has allowed estimation of m^* values for the excess charge carriers in these nanocrystals, and we find them to be mostly consistent with literature bulk values for these same materials. These findings illustrate the power of MCD spectroscopy as a spectroscopic probe of excess charge carriers in doped semiconductor nanocrystals, allowing quantitative evaluation of key electronic properties of these materials relevant to both fundamental and applied sciences.

4.5 Experimental methods

4.5.1 Chemicals. Copper (I) chloride (CuCl; ≥99.995%), selenium powder (Se; >99.99%), octadecene (ODE; 90%), and oleylamine (OAm; 70%) were purchased from Sigma-Aldrich and used without further purification.

4.5.2 $Cu_{2-x}Se$ nanocrystal synthesis. Colloidal $Cu_{2-x}Se$ nanocrystals were synthesized using standard Schlenk techniques according to a literature procedure.[1] Briefly, 1.2 mmol Se was dispersed in 9 mL ODE and 6 mL OAm. In a separate flask, 1.2 mmol CuCl was dispersed in 3 mL ODE and 2 mL OAm. Both flasks were evacuated at 120 °C for one hour, after which the Se solution was heated rapidly under nitrogen to 310 °C and the Cu solution swiftly injected, causing the temperature to drop. The temperature recovered and the nanocrystals were grown for 20 minutes before cooling to room temperature. The resulting $Cu_{2-x}Se$ nanocrystals were precipitated with ethanol, collected by centrifugation, and the pellet re-suspended in toluene. TEM images of the $Cu_{2-x}Se$ nanocrystals investigated show faceted structures with average $d \sim 17$ nm.

4.5.3 Ag nanoparticle synthesis. Ag nanoparticles were prepared as detailed previously.[2,3] The preparation resulted in nanoprisms with edge lengths of $d \sim 50$ nm.

4.5.4 Physical characterization. Transmission electron miscroscope (TEM) images were obtained using a FEI Tecnai G2 F20 operating at 200 kV. Absorption spectra for both films and solution samples were collected at room temperature on a Cary 500 (Varian) spectrometer. Note that all of the semiconductor nanocrystals analyzed here, as well as the Au nanoparticles,[4] are sufficiently small that extinction spectra can be equated with absorption spectra, but this approximation may not hold rigorously for the Ag nanoparticles examined here ($d \sim 50$ nm), where scattering may also contribute to extinction.[5] For simplicity, we refer to all such data as absorption spectra here. MCD spectra were collected in the Faraday configuration using an Aviv 40DS spectropolarimeter and a Teledyne-Judson InGaAs NIR detector. MCD spectra on nanocrystal solutions were measured in a 1 mm pathlength quartz cuvette at room temperature using a 1.5 T electromagnet. Higher field (up to 6 T) MCD spectra were collected on nanocrystal films using a high-field superconducting magneto-optical cryostat (Cryo-Industries SMC-1659 OVT). For film preparation, semiconductor nanocrystals were mixed with poly (lauryl methacrylate) in toluene, sandwiched between two quartz discs, and heated at 75−90°C for several hours to dry and set films. All MCD spectra are represented according to the sign convention outlined in Piepho and Schatz,[6] such that $\Delta A = A_L - A_R$, where A_L and A_R are the absorption of left (σ^-) and right (σ^+) circularly polarized light. MCD spectra are reported as $\Delta A/A_{max}$ per unit Tesla, where A_{max} is the absorption band's maximum absorbance measured at zero field. In principle, experimental MCD intensities are subject to suppression due to depolarization *via* light scattering. Depolarization was therefore experimentally verified to be <10% for all films (n-ZnO, n-ITO, Ag, and low-temperature p-$Cu_{2-x}Se$) and negligible for all solution samples (p-$Cu_{2-x}Se$) examined here. Depolarization was measured by comparing the CD signal of a chiral molecule placed before and after the sample.

4.5.5 MCD spectral simulations. MCD experimental data were simulated by using the experimental LSPR linear absorption lineshapes as input, because any discrepancy between experiment and simulation would be enhanced in the MCD due the heightened sensitivity of this technique. Thus the linear absorption band was duplicated, and the two bands shifted by equal amounts to higher and lower energies according to the rigid-shift approximation. This anaylsis assumes that σ^+ and σ^- LSPR band shapes are independent of magnetic field within our experimental range. MCD spectra are generated by taking the difference between the shifted bands in compliance with the sign convention defined in Figure 4.2. A least squares fitting analysis was applied to determine the best fits to the experimental data. The result of this analysis for *n*-ZnO, *n*-ITO, and *p*-Cu_{2-x}Se nanocrystals is shown in Appendix C.

4.6 References

1. Armelles, G.; Cebollada, A.; Garcia-Martin, A.; Gonzalez, M. U., Magnetoplasmonics: Combining Magnetic and Plasmonic Functionalities. *Adv. Opt. Mater.* **2013,** *1*, 10-35.
2. Schimpf, A. M.; Knowles, K. E.; Carroll, G. M.; Gamelin, D. R., Electronic Doping and Redox Potential Tuning in Colloidal Semiconductor Nanocrystals. *Acc. Chem. Res.* **2015,** *48*, 1929-1937.
3. Routzahn, A. L.; White, S. L.; Fong, L.-K.; Jain, P. K., Plasmonics with Doped Quantum Dots. *Israel J. Chem.* **2012,** *52*, 983-991.
4. Scotognella, F.; Valle, G.; Srimath Kandada, A.; Zavelani-Rossi, M.; Longhi, S.; Lanzani, G.; Tassone, F., Plasmonics in Heavily-Doped Semiconductor Nanocrystals. *Eur. Phys. J. B* **2013,** *86*, 1-13.
5. Shim, M.; Guyot-Sionnest, P., Organic-Capped ZnO nanocrystals: Synthesis and *n*-Type Character. *J. Am. Chem. Soc.* **2001,** *123*, 11651-11654.
6. Shim, M.; Wang, C.; Guyot-Sionnest, P., Charge-Tunable Optical Properties in Colloidal Semiconductor Nanocrystals. *J. Phys. Chem. B* **2001,** *105*, 2369-2373.
7. Wehrenberg, B. L.; Guyot-Sionnest, P., Electron and Hole Injection in PbSe Quantum Dot Films. *J. Am. Chem. Soc.* **2003,** *125*, 7806-7807.
8. Liu, W. K.; Whitaker, K. M.; Kittilstved, K. R.; Gamelin, D. R., Stable Photogenerated Carriers in Magnetic Semiconductor Nanocrystals. *J. Am. Chem. Soc.* **2006,** *128*, 3910-3911.
9. Guyot-Sionnest, P., Charging Colloidal Quantum Dots by Electrochemistry. *Microchim. Acta* **2008,** *160*, 309-314.

10. Kanehara, M.; Koike, H.; Yoshinaga, T.; Teranishi, T., Indium Tin Oxide Nanoparticles with Compositionally Tunable Surface Plasmon Resonance Frequencies in the Near-IR Region. *J. Am. Chem. Soc.* **2009,** *131*, 17736-17737.
11. Wang, T.; Radovanovic, P. V., Free Electron Concentration in Colloidal Indium Tin Oxide Nanocrystals Determined by Their Size and Structure. *J. Phys. Chem. C* **2011,** *115*, 406-413.
12. Cohn, A. W.; Janßen, N.; Mayer, J. M.; Gamelin, D. R., Photocharging ZnO Nanocrystals: Picosecond Hole Capture, Electron Accumulation, and Auger Recombination. *J. Phys. Chem. C* **2012,** *116*, 20633-20642.
13. Manthiram, K.; Alivisatos, A., Tunable Localized Surface Plasmon Resonances in Tungsten Oxide Nanocrystals. *J. Am. Chem. Soc.* **2012,** *134*, 3995-3998.
14. De Trizio, L.; Buonsanti, R.; Schimpf, A. M.; Llordes, A.; Gamelin, D. R.; Simonutti, R.; Milliron, D. J., Nb-Doped Colloidal TiO_2 Nanocrystals with Tunable Infrared Absorption. *Chem. Mater.* **2013,** *25*, 3383-3390.
15. Koh, W.-K.; Koposov, A. Y.; Stewart, J. T.; Pal, B. N.; Robel, I.; Pietryga, J. M.; Klimov, V. I., Heavily Doped *n*-Type PbSe and PbS Nanocrystals Using Ground-State Charge Transfer from Cobaltocene. *Sci. Rep.* **2013,** *3*, 1-8.
16. Palomaki, P. K. B.; Miller, E. M.; Neale, N. R., Control of Plasmonic and Interband Transitions in Colloidal Indium Nitride Nanocrystals. *J. Am. Chem. Soc.* **2013,** *135*, 14142-14150.
17. Rinehart, J. D.; Schimpf, A. M.; Weaver, A. L.; Cohn, A. W.; Gamelin, D. R., Photochemical Electronic Doping of Colloidal CdSe Nanocrystals. *J. Am. Chem. Soc.* **2013,** *135*, 18782-18785.
18. Schimpf, A. M.; Gunthardt, C. E.; Rinehart, J. D.; Mayer, J. M.; Gamelin, D. R., Controlling Carrier Densities in Photochemically Reduced Colloidal ZnO Nanocrystals: Size Dependence and Role of the Hole Quencher. *J. Am. Chem. Soc.* **2013,** *135*, 16569-16577.
19. Comin, A.; Manna, L., New Materials for Tunable Plasmonic Colloidal Nanocrystals. *Chem. Soc. Rev.* **2014,** *43*, 3957-3975.
20. Beaulac, R.; Ochsenbein, S. T.; Gamelin, D. R., Colloidal Transition-Metal-Doped Quantum Dots. In *Nanocrystal Quantum Dots, 2nd ed.*, CRC Press: Boca Raton, FL, **2010**; pp 397-453.
21. Schimpf, A. M.; Thakkar, N.; Gunthardt, C. E.; Masiello, D. J.; Gamelin, D. R., Charge-Tunable Quantum Plasmons in Colloidal Semiconductor Nanocrystals. *ACS Nano* **2014,** *8*, 1065-1072.
22. Schimpf, A. M.; Runnerstrom, E. L.; Lounis, S. D.; Milliron, D. J.; Gamelin, D. R., Redox Energies and Plasmon Resonance Energies of Photodoped In_2O_3 and Sn-doped In_2O_3 Nanocrystals. *J. Am. Chem. Soc.* **2015,** *137*, 518-524.
23. Pineider, F.; Campo, G.; Bonanni, V.; de Julián Fernández, C.; Mattei, G.; Caneschi, A.; Gatteschi, D.; Sangregorio, C., Circular Magnetoplasmonic Modes in Gold Nanoparticles. *Nano Lett.* **2013,** *13*, 4785-4789.
24. van der Stam, W.; Akkerman, Q. A.; Ke, X.; van Huis, M. A.; Bals, S.; de Mello Donega, C., Solution-Processable Ultrathin Size- and Shape-Controlled Colloidal $Cu_{2-x}S$ Nanosheets. *Chem. Mater.* **2015,** *27*, 283-291.
25. Lesnyak, V.; George, C.; Genovese, A.; Prato, M.; Casu, A.; Ayyappan, S.; Scarpellini, A.; Manna, L., Alloyed Copper Chalcogenide Nanoplatelets via Partial Cation Exchange Reactions. *ACS Nano* **2014,** *8*, 8407-8418.

26. Ishikawa, Y.; Yao, H., Surface Magnetoplasmons in Silver Nanoparticles: Apparent Magnetic-Field Enhancement Manifested by Simultaneous Deconvolution of UV–Vis Absorption and MCD Spectra. *Chem. Phys. Lett.* **2014,** *609*, 93-97.
27. Yao, H.; Shiratsu, T., Individual and Collective Modes of Surface Magnetoplasmon in Thiolate-Protected Silver Nanoparticles Studied by MCD Spectroscopy. *Nanoscale* **2016,** *8*, 11264-11274.
28. Weick, G.; Weinmann, D., Lifetime of the Surface Magnetoplasmons in Metallic Nanoparticles. *Phys. Rev. B* **2011,** *83*, 1-10.
29. Kasap, S., *Principles of Electronic Materials and Devices*. 2nd ed.; McGraw-Hill: New York, NY, 2002.
30. Omar, M. A., *Elementary Solid State Physics: Principles and Applications*. Addison-Wesley Publishing Company, Inc.: Philippines, **1975**.
31. Liu, W. K.; Whitaker, K. M.; Smith, A. L.; Kittilstved, K. R.; Robinson, B. H.; Gamelin, D. R., Room-Temperature Electron Spin Dynamics in Free-Standing ZnO Quantum Dots. *Phys. Rev. Lett.* **2007,** *98*, 186804.
32. Zaitoun, M. A.; Mason, W. R.; Lin, C. T., Magnetic Circular Dichroism Spectra for Colloidal Gold Nanoparticles in Xerogels at 5.5 K. *J. Phys. Chem. B* **2001,** *105*, 6780-6784.
33. The authors of ref 32 describe this behavior in Au nanoparticles as arising from an A-term MCD mechanism, whereas the authors of ref 23 describe it as magnetoplasmonic in origin. There is no obvious conflict between these two descriptions, given eq 4.2 and the definition of MCD A-terms as arising from magnetic-field-induced excited-state splittings (ref 34), regardless of the specific origins of those splittings.
34. Piepho, S. B.; Schatz, G. C., *Group Theory in Spectroscopy with Applications to Magnetic Circular Dichroism*. Wiley: New York, **1983**.
35. Artemyev, M.; Krutokhvostov, R.; Melnikau, D.; Oleinikov, V.; Sukhanova, A.; Nabiev, I., Low-Field Magnetic Circular Dichroism in Silver and Gold Colloidal Nanoparticles of Different Sizes, Shapes, and Aggregation States. *Proc. SPIE* **2012,** *8457*, 845729.
36. Lounis, S. D.; Runnerstrom, E. L.; Bergerud, A.; Nordlund, D.; Milliron, D. J., Influence of Dopant Distribution on the Plasmonic Properties of Indium Tin Oxide Nanocrystals. *J. Am. Chem. Soc.* **2014,** *136*, 7110-7116.
37. Mansour, B. A.; Demian, S. E.; Zayed, H. A., Determination of the Effective Mass for Highly Degenerate Copper Selenide from Reflectivity Measurements. *J. Mater. Sci.-Mater. El.* **1992,** *3*, 249-252.
38. Gorbachev, V. V.; Putilin, I. M., Some Parameters of Band Structure in Copper Selenide and Telluride. *Phys. Stat. Sol. A* **1973,** *16*, 553-559.
39. Madelung, O., *Semiconductors: Data Handbook*. 3rd ed.; Springer: New York, 2004.
40. Preissler, N.; Bierwagen, O.; Ramu, A. T.; Speck, J. S., Electrical Transport, Electrothermal Transport, and Effective Electron Mass in Single-Crystalline In_2O_3 films. *Phys. Rev. B* **2013,** *88*, 1-10.
41. Solieman, A.; Aegerter, M. A., Modeling of Optical and Electrical Properties of In_2O_3:Sn Coatings Made by Various Techniques. *Thin Solid Films* **2006,** *502*, 205-211.
42. Morkoç, H.; Özgür, Ü., General Properties of ZnO. In *Zinc Oxide*, Wiley-VCH Verlag GmbH & Co. KGaA: 2009; pp 1-76.
43. Johnson, P. B.; Christy, R. W., Optical Constants of the Noble Metals. *Phys. Rev. B* **1972,** *6*, 4370-4379.

44. Edwards, P. P.; Porch, A.; Jones, M. O.; Morgan, D. V.; Perks, R. M., Basic Materials Physics of Transparent Conducting Oxides. *Dalton Transactions* **2004**, 2995-3002.
45. Crassee, I.; Orlita, M.; Potemski, M.; Walter, A. L.; Ostler, M.; Seyller, T.; Gaponenko, I.; Chen, J.; Kuzmenko, A. B., Intrinsic Terahertz Plasmons and Magnetoplasmons in Large Scale Monolayer Graphene. *Nano Lett.* **2012,** *12*, 2470-2474.
46. Kriegel, I.; Rodríguez-Fernández, J.; Wisnet, A.; Zhang, H.; Waurisch, C.; Eychmüller, A.; Dubavik, A.; Govorov, A. O.; Feldmann, J., Shedding Light on Vacancy-Doped Copper Chalcogenides: Shape-Controlled Synthesis, Optical Properties, and Modeling of Copper Telluride Nanocrystals with Near-Infrared Plasmon Resonances. *ACS Nano* **2013,** *7*, 4367-4377.
47. Hsu, S.-W.; On, K.; Tao, A. R., Localized Surface Plasmon Resonances of Anisotropic Semiconductor Nanocrystals. *J. Am. Chem. Soc.* **2011,** *133*, 19072-19075.
48. Hsu, S.-W.; Bryks, W.; Tao, A. R., Effects of Carrier Density and Shape on the Localized Surface Plasmon Resonances of $Cu_{2-x}S$ Nanodisks. *Chem. Mater.* **2012,** *24*, 3765-3771.
49. Scotognella, F.; Della Valle, G.; Srimath Kandada, A. R.; Dorfs, D.; Zavelani-Rossi, M.; Conforti, M.; Miszta, K.; Comin, A.; Korobchevskaya, K.; Lanzani, G.; Manna, L.; Tassone, F., Plasmon Dynamics in Colloidal $Cu_{2-x}Se$ Nanocrystals. *Nano Lett.* **2011,** *11*, 4711-4717.
50. Whitaker, K. M.; Ochsenbein, S. T.; Polinger, V. Z.; Gamelin, D. R., Electron Confinement Effects in the EPR Spectra of Colloidal *n*-Type ZnO Quantum Dots. *J. Phys. Chem. C* **2008,** *112*, 14331-14335.

Appendix A: *Supplementary Information for Chapter 2* Electron Stability and Negative-Tetron Luminescence in Free-Standing Colloidal *n*-Type CdSe/CdS Quantum Dots

Reproduced with permission from:

Hartstein, K. H.; Erickson, C. S.; Tsui, E. Y.; Marchioro, A.; Gamelin, D. R. *ACS Nano* **2017**, *11*, 10430–10438. Copyright 2017 American Chemical Society.

A.1 Continuous-wave absorption and PL measurements

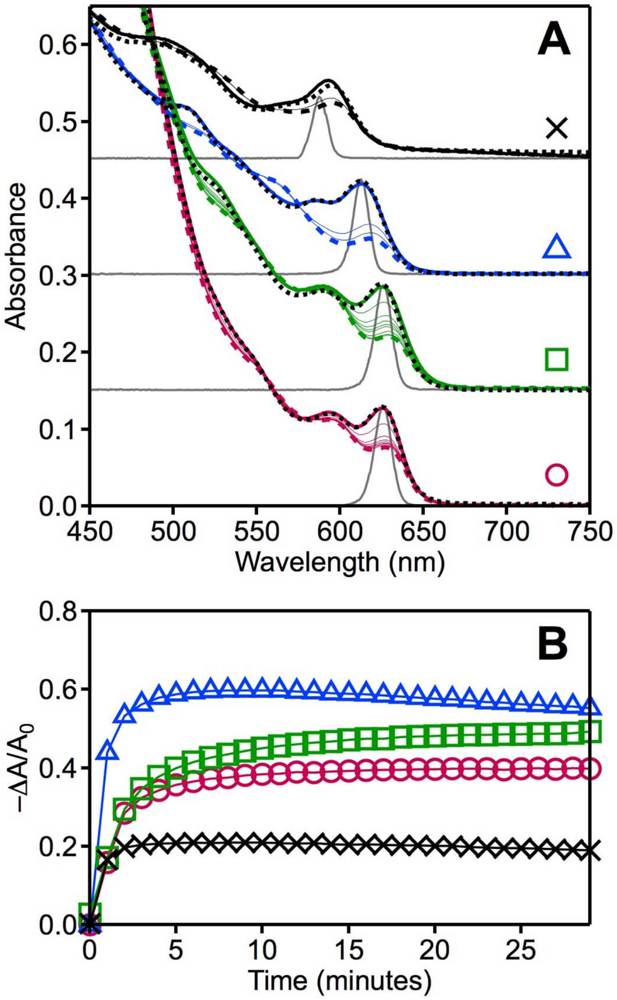

Figure A.1. Resonant photodoping of core/shell nanocrystals. (**A**) Absorption of CdSe/*x*CdS QDs with *x* = 0, 2, 4, and 7 monolayers collected during photodoping using resonant photoeexcitation, in preparation to measure anaerobic recovery kinetics. The gray traces show the spectral profile of the lamp used to photoexcite each respective sample. (**B**) Kinetics of photodoping for the samples shown in panel A, collected under resonant photodoping conditions.

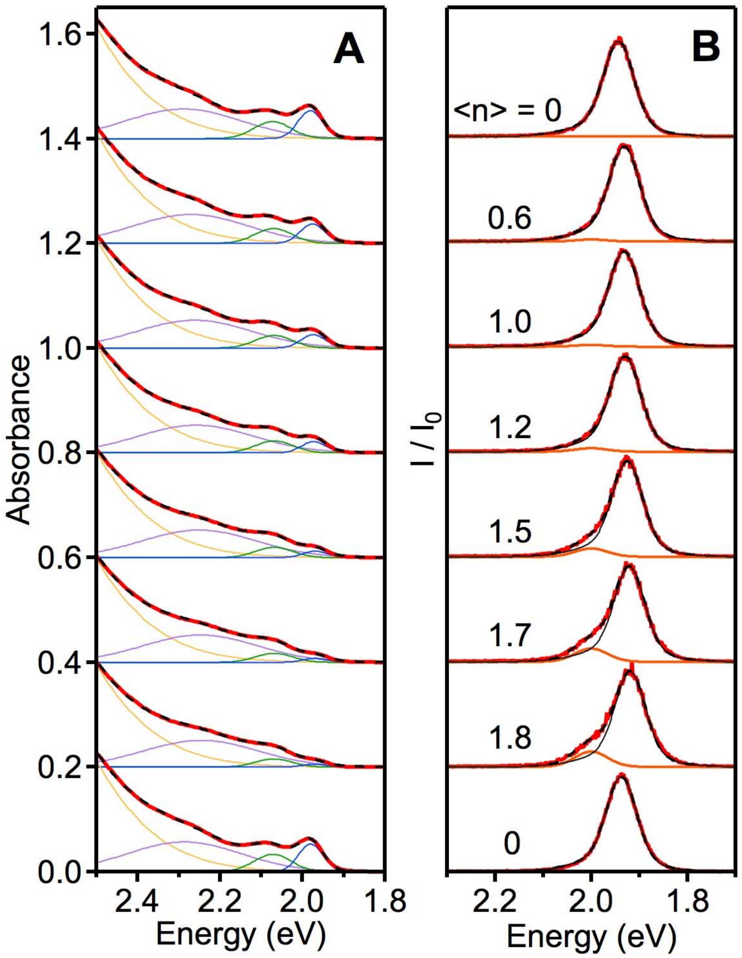

Figure A.2. Global fitting analysis to absorption and PL during photodoping. (**A**) Absorption and (**B**) normalized PL intensity integrated over the first 8 ns of emission for CdSe/7CdS QDs with increasing carrier density (top to bottom). Bottom spectra show samples after reoxidation. Comparing experimental data (red solid) with global fitting components (colored Gaussians) and complete analysis (black dashed) allows extraction of $\langle n \rangle$ values and relative $1P_e$ emission intensities.

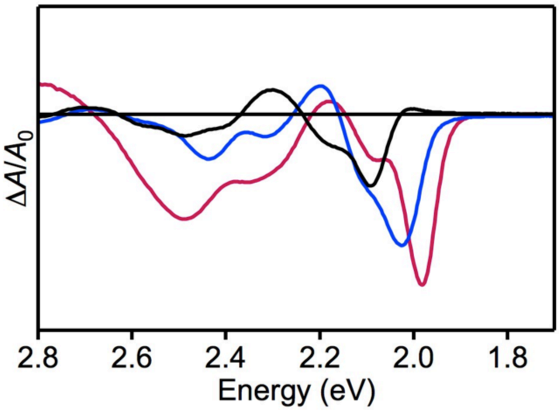

Figure A.3. Excitonic bleach with varying shell thickness. Normalized differential absorption spectra for CdSe/*x*CdS samples from main text where *x* = 0, 2, and 7, respectively. Spectra for all samples demonstrate clear bleaches of $1S_h$-$1S_e$ and $2S_h$-$1S_e$ electronic absorption transitions.

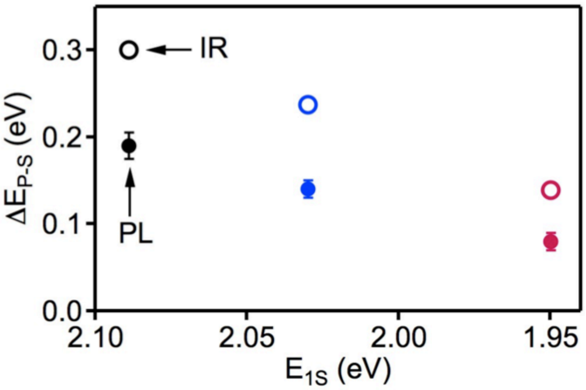

Figure A.4. $\Delta E_{P\text{-}S}$(IR) and $\Delta E_{P\text{-}S}$(PL). $\Delta E_{P\text{-}S}$(IR) and $\Delta E_{P\text{-}S}$(PL) plotted *vs* E_{1S} measured by absorption for CdSe/*x*CdS where *x* = 0, 2, and 7. Error bars in PL measurements reflect the uncertainty from multipeak fitting, and error bars in IR data points are smaller than the markers on the plot.

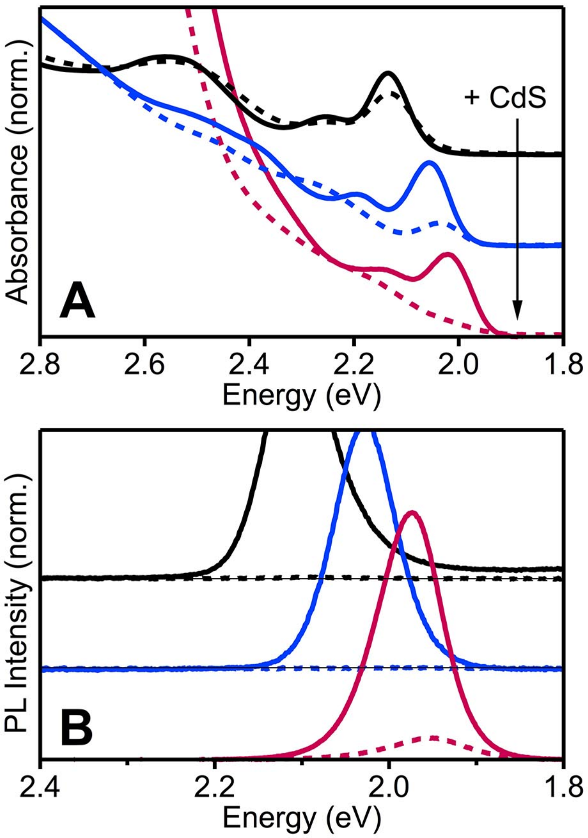

Figure A.5. Photodoping additional sample set. (A) Absorption and (B) PL of an alternate set of as-prepared (solid) and maximally photodoped (dashed) CdSe/*x*CdS QDs with $x = 0$, 3, and 9 monolayers of CdS shell deposited on $d = 3.8$ nm CdSe cores.

A.2 Time-resolved PL measurements

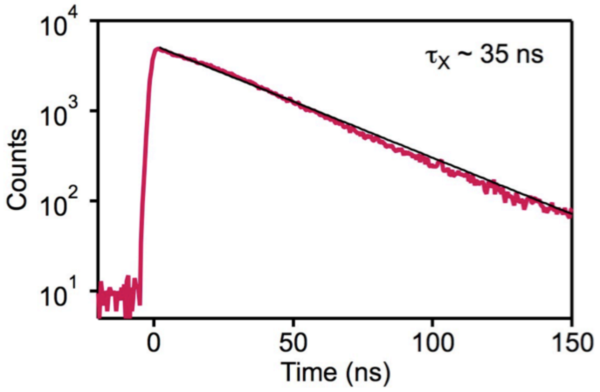

Figure A.6. Time-resolved PL dynamics of undoped QDs. Semi-log representation of dynamics from as-prepared CdSe/7CdS QDs, fit to a mono-exponential decay (thin solid line).

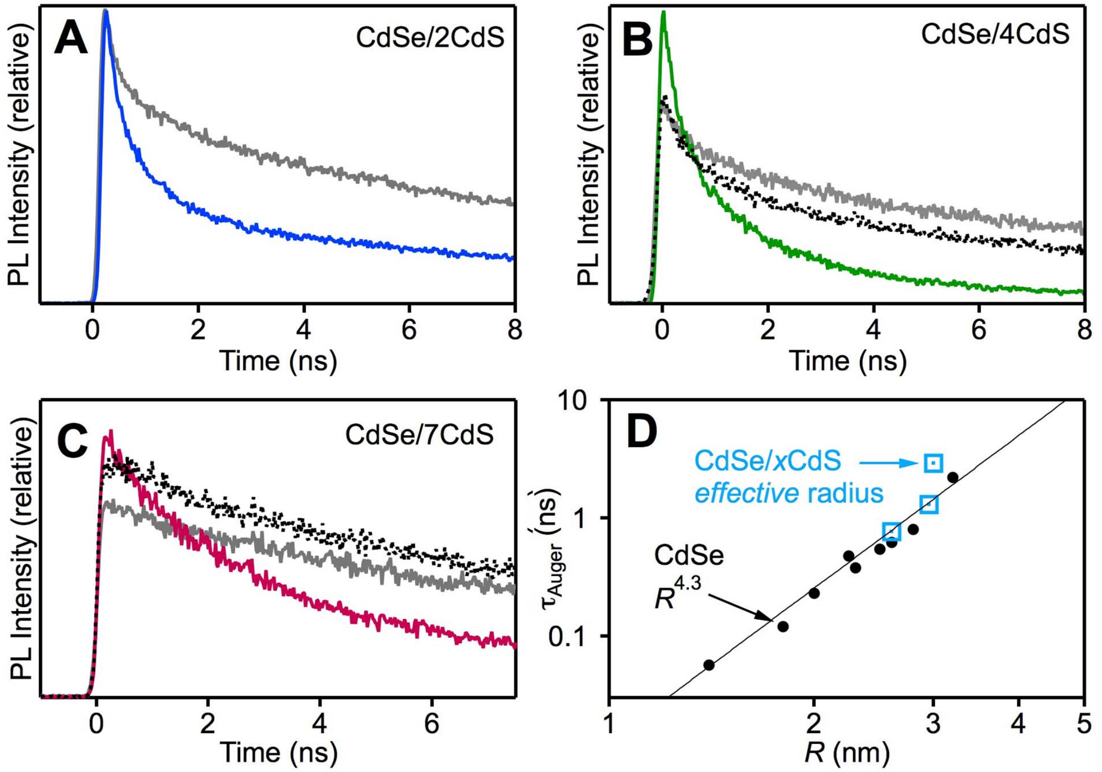

Figure A.7. TRPL of X⁻ Auger recombination. (A-C) Transient decay traces for as-prepared ($\langle n \rangle = 0$, grey), photodoped ($\langle n \rangle < 1$, colored), and reoxidized ($\langle n \rangle = 0$, dotted) CdSe/*x*CdS QDs. (D) τ_A^{X-} for CdSe/*x*CdS plotted *vs* effective radius (⊡) determined from the energy of the first excitonic absorption feature. CdSe data (•) are reproduced from Ref. 1.

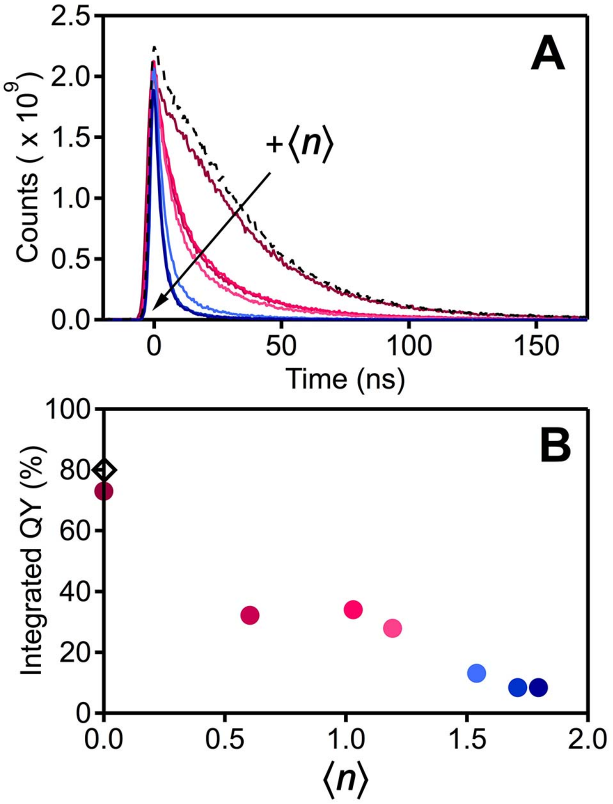

Figure A.8. TRPL and QY with varied $\langle n \rangle$. (A) PL decay traces of CdSe/7CdS QDs photodoped to various values of $\langle n \rangle$. (B) QY *vs* $\langle n \rangle$, quantified by integrating traces in panel A and adjusting relative to $\langle n \rangle = 0$ value of 73% as measured in integrating sphere.

A.3 Electron orbital occupancy

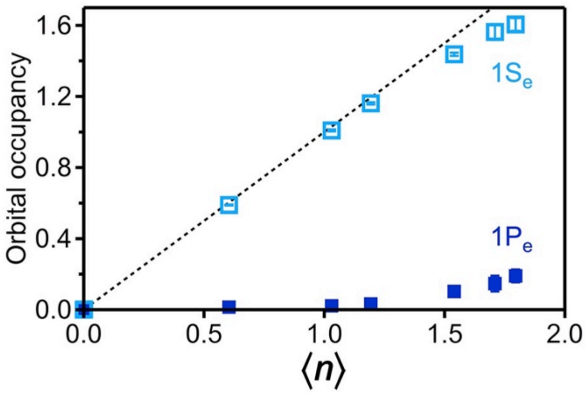

Figure A.9. Orbital occupancy. Occupancy of 1S and 1P electron orbitals in CdSe/7CdS QDs plotted *vs* $\langle n \rangle$, as determined from relative PL intensities extracted from global fitting analysis. The dashed line has a slope of unity and highlights deviation of $1S_e$ occupancy from total $\langle n \rangle$ at values of $\langle n \rangle > 1$.

A.4 References

1. Cohn, A. W.; Rinehart, J. D.; Schimpf, A. M.; Weaver, A. L.; Gamelin, D. R. Size Dependence of Negative Trion Auger Recombination in Photodoped CdSe Nanocrystals. *Nano Lett*. **2013**, *14*, 353-358.

Appendix B: *Supplementary Information for Chapter 3*
Copper-Coupled Electron Transfer in Colloidal Plasmonic Copper-Sulfide Nanocrystals Probed by *In Situ* Spectroelectrochemistry

Reproduced with permission from:

Hartstein, K. H.; Brozek, C. K.; Hinterding, S. O. M.; Gamelin, D. R. *J. Am. Chem. Soc*. **2018**, *140*, 3434–3442. Copyright 2018 American Chemical Society.

B.1 Absorption spectra of copper-sulfide nanocrystals treated with various oxidants

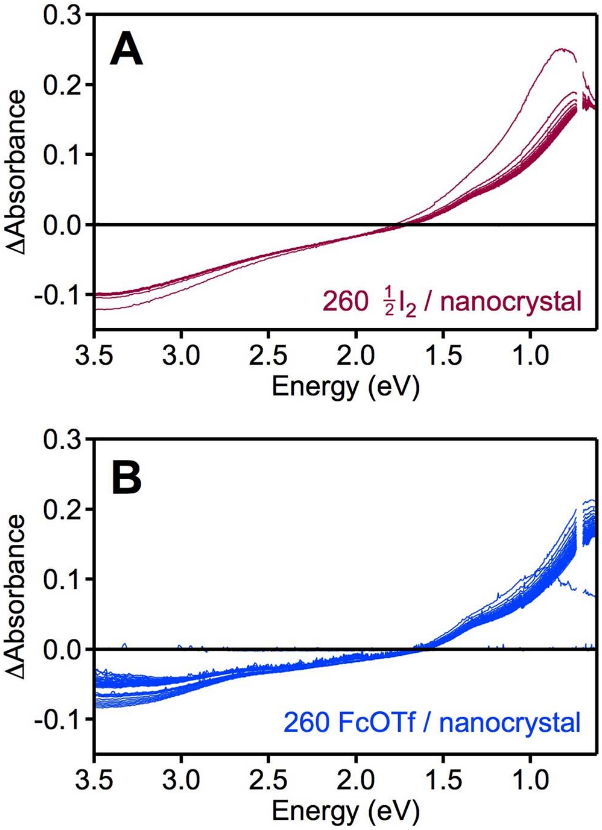

Figure B.1. Differential absorption spectra collected during potentiometry. Complete set of differential absorption spectra for d = 5.4 nm copper-sulfide nanocrystals oxidized with 260 equivalents of (**A**) ½I_2 and (**B**) FcOTf. The first FcOTf scan shows initial oxidation occurring concurrently with absorption measurement (scan with decreased intensity at $E < 1$ eV).

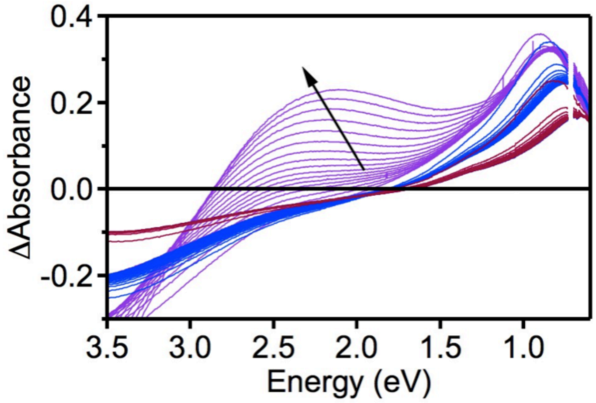

Figure B.2. Differential absorption spectra with excess I_2. Differential absorption spectra of *d* = 5.4 nm copper-sulfide nanocrystals after addition of 260 (red), 520 (blue), and 780 (purple) equivalents of ½I_2.

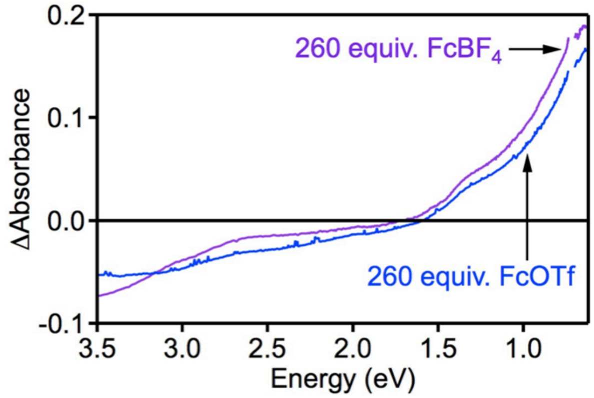

Figure B.3. Comparison between FcOTf and FcBF$_4$ nanocrystal oxidation. Differential absorption spectra of *d* = 5.4 nm copper-sulfide nanocrystals after addition of 260 equivalents of FcBF$_4$ (purple) or FcOTf (blue).

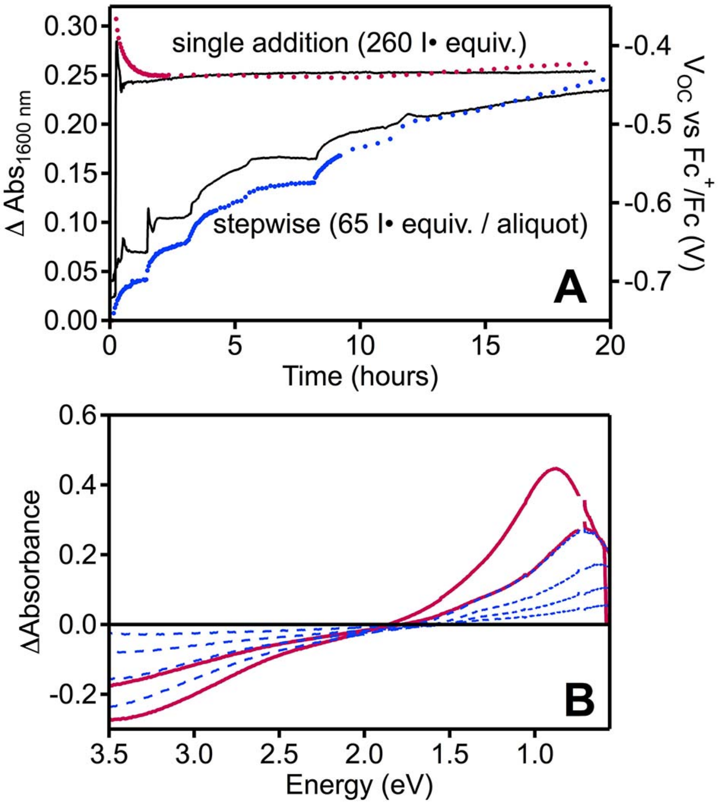

Figure B.4. Spectroelectrochemistry with stepwise I_2 addition. (**A**) Differential absorption intensities (markers) and V_{OC} (lines) *vs* time measured during I_2 oxidation of *d* = 5.4 nm copper-sulfide nanocrystals. The oxidant was added either in a single addition (260 equivalents ½I_2 per nanocrystal) or stepwise in 4 additions (65 equivalents per aliquot). (**B**) Differential absorption spectra collected during single addition (solid) and stepwise additions (dashed). Final LSPR intensities and V_{OC} values are indistinguishable for the two methods.

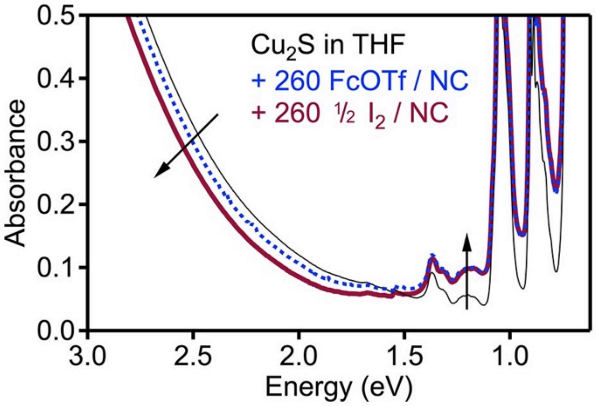

Figure B.5. As-collected absorption spectra of oxidized copper-sulfide nanocrystals. Absorption spectra of d = 5.4 nm copper-sulfide nanocrystals as-prepared (thin solid) and after addition of 260 equivalents of either Fc^+ (added as FcOTf, dashed) or $\frac{1}{2}I_2$ (thick solid). Spectra were collected in 0.1 M $TBAPF_6$ THF without any background subtraction. Difference spectra are shown in Figure 3 of the main text.

B.2 Additional XRD experiments

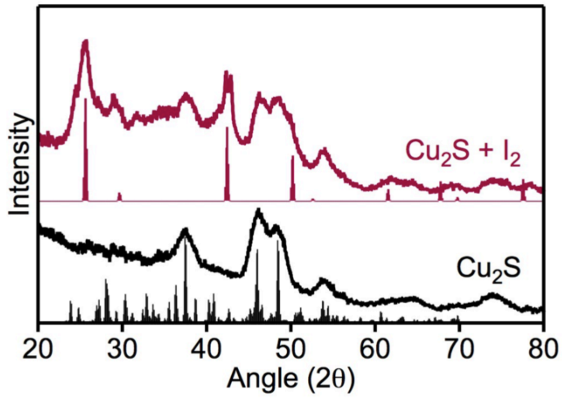

Figure B.6. XRD of small copper-sulfide nanocrystals with I_2. XRD of d = 5.4 nm copper-sulfide nanocrystals after oxidation with I_2 demonstrates CuI formation, but lattice contraction is obscured by the broad peak widths.

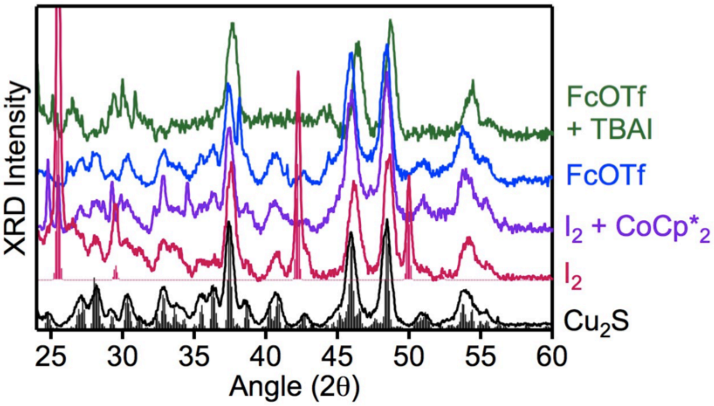

Figure B.7. XRD of *d* ~ 12 nm Cu_2S nanocrystals treated with various oxidants. Low-chalcocite Cu_2S and marshite CuI bulk patterns are shown for reference.

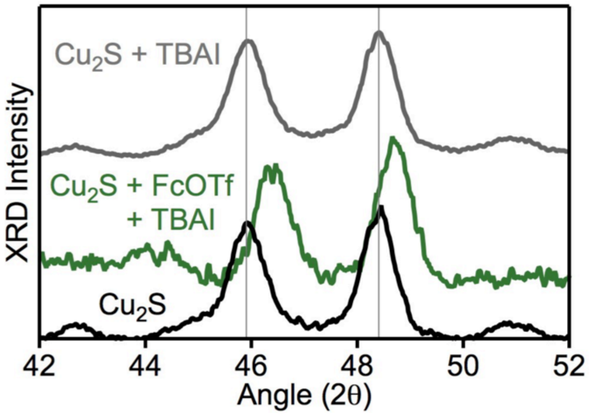

Figure B.8. TBAI XRD control. XRD of *d* ~ 12 nm copper-sulfide nanocrystals in the presence of TBAI with (middle) and without (top) prior addition of FcOTf.

B.3 XPS of copper-sulfide nanocrystals after redox manipulations

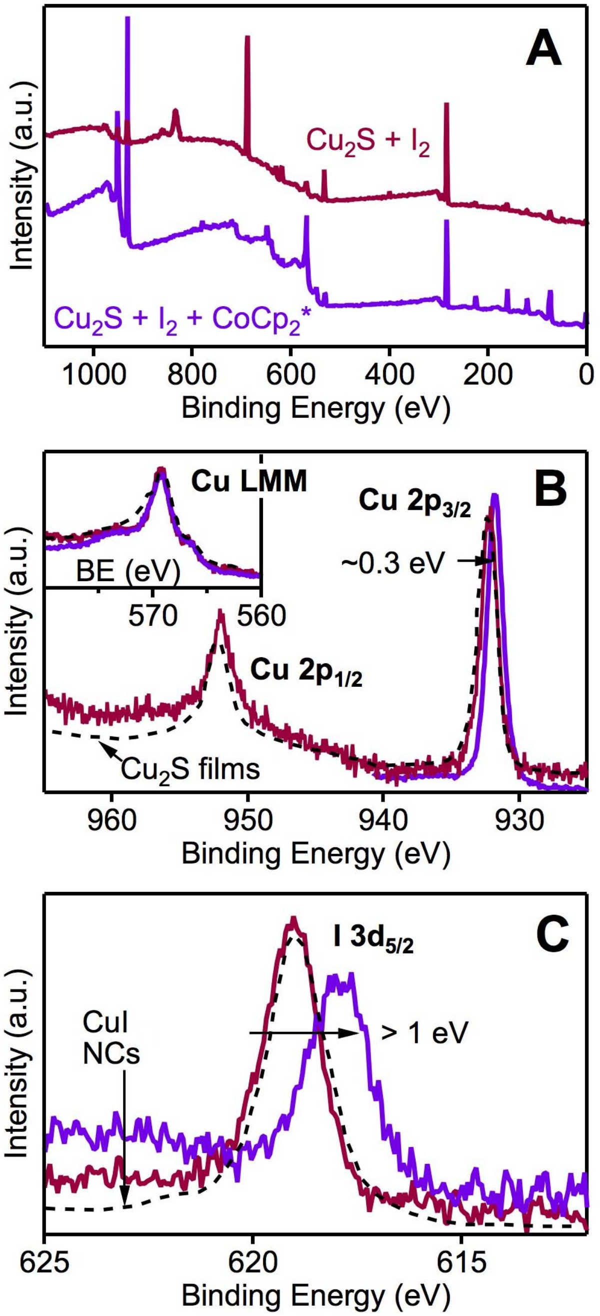

Figure B.9. XPS of copper-sulfide nanocrystals after redox manipulations. (**A**) XPS survey spectrum of $d = 5.4$ nm copper-sulfide nanocrystals oxidized with 520 equivalents of $\frac{1}{2}I_2$ (per nanocrystal) and subsequently reduced with > 520 equivalents of $CoCp^*_2$. (**B**) Cu 2p and Cu LMM (inset) peaks indicate Cu^+. (**C**) I $3d_{5/2}$ region shows evidence of reduced I^- rather than elemental I_2. Dashed traces correspond to literature examples of XPS measurements in Cu_2S nanocrystal films and CuI nanocrystals from Refs 1 and 2, respectively.

B.4 EPR of copper-sulfide nanocrystals treated with I_2

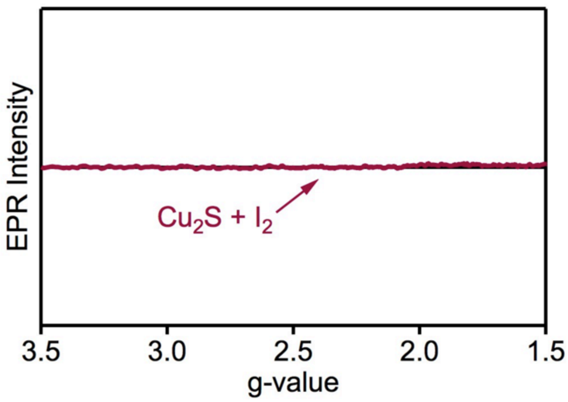

Figure B.10. EPR of copper-sulfide nanocrystals treated with I_2. EPR spectra show no evidence of Cu^{2+} in $d = 5.4$ nm copper-sulfide samples oxidized with I_2.

B.5 References

1. Tang, A.; Qu, S.; Li, K.; Hou, Y.; Teng, F.; Cao, J.; Wang, Y.; Wang, Z. One-Pot Synthesis and Self-Assembly of Colloidal Copper(I) Sulfide Nanocrystals. *Nanotechnology* **2010**, *21*, 285602.
2. Yang, M.; Xu, J.-Z.; Xu, S.; Zhu, J.-J.; Chen, H.-Y. Preparation of Spherical CuI Nanoparticles. *Inorg. Chem. Commun.* **2004**, *7*, 628-630.

Appendix C: *Supplementary Information for Chapter 4*
Cyclotron Splittings in the Plasmon Resonances of Degenerately Doped Semiconductor Nanocrystals Probed by Magnetic Circular Dichroism Spectroscopy

Reproduced with permission from:

Hartstein, K. H.; Schimpf, A. M.; Salvador, M.; Gamelin, D. R. *J. Phys. Chem. Lett.* **2017**, *8*, 1831–1836. Copyright 2017 American Chemical Society.

C.1 $Cu_{2-x}Se$ nanoplatelet characterization

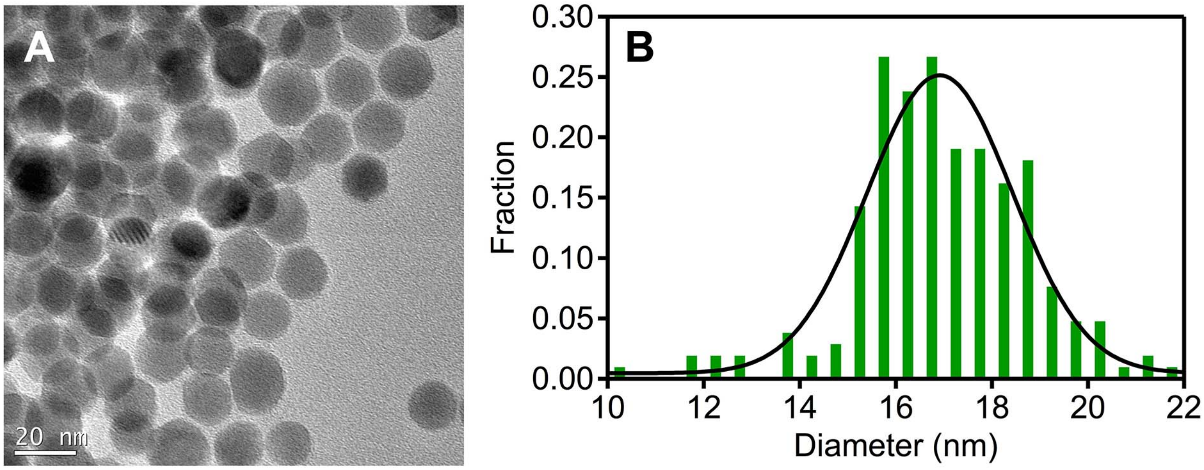

Figure C.1. $Cu_{2-x}Se$ nanoplatelet characterization. (**A**) TEM image and (**B**) corresponding size histogram of the d = 16.9 nm $Cu_{2-x}Se$ nanocrystals measured by MCD. Their thickness here is consistent with the thicknesses of ~2 – 4 nm reported in previous studies of related nanoplatelets.[7,8]

C.2 MCD spectral simulations

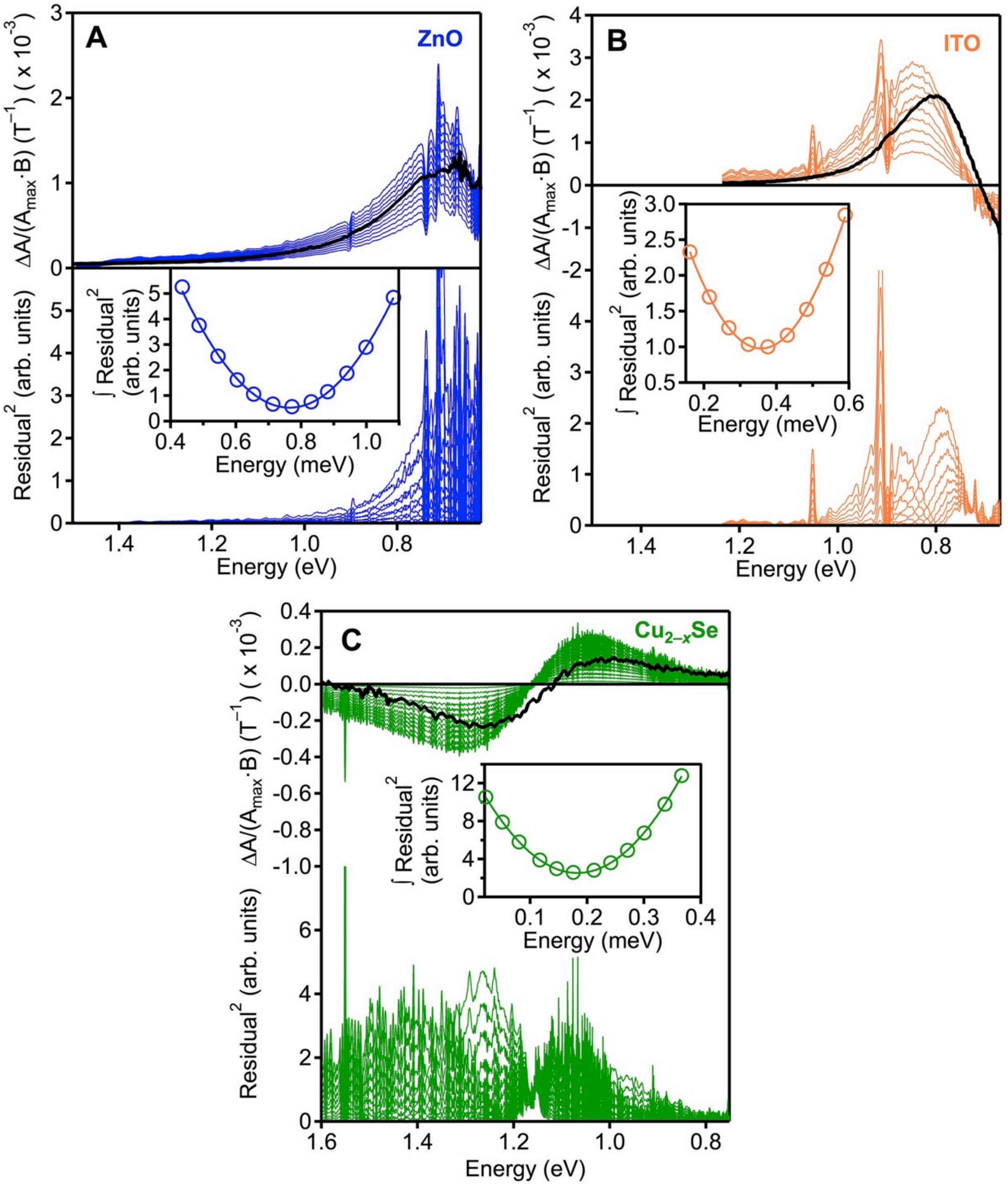

Figure C.2. MCD analysis to obtain splitting energies. MCD spectra were simulated using experimental absorption band shapes using the rigid-shift approximation, which assumes the band shape is independent of magnetic field under these conditions. The thin traces (top axes) show MCD spectra for (**A**) *n*-ZnO, (**B**) *n*-ITO, and (**C**) *p*-$Cu_{2-x}Se$ nanocrystals, calculated for various splitting energies. The thick traces plot the experimental MCD spectra of each corresponding nanocrystal sample. The squared differences between experimental and simulated MCD spectra are plotted on the bottom axes. The insets plot the integrated squared residuals. The minima in these inset curves yield the reported experimental splitting energies.

C.3 Additional MCD data

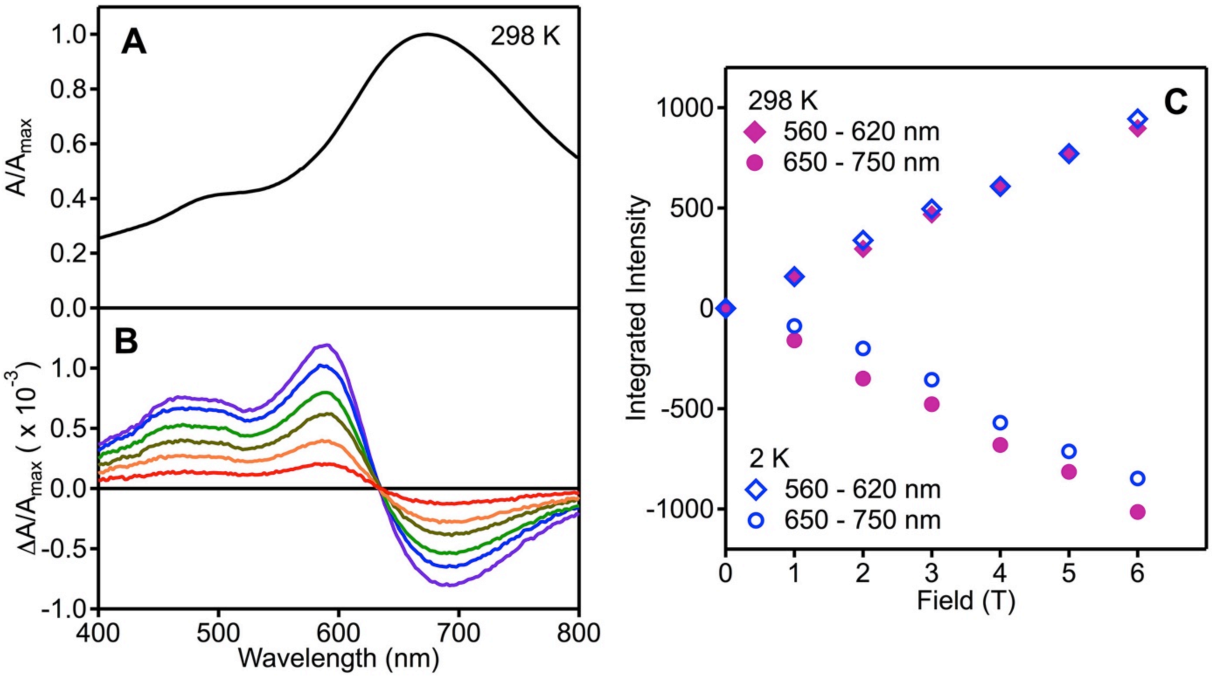

Figure C.3. Temperature- and field-dependent Ag nanoparticle MCD. (**A**) Zero-field absorption and (**B**) magnetic field-dependent MCD spectra of Ag nanoparticles, measured from 1-6 T at 298 K. (**C**) Integrated intensity of MCD spectra at 298 K (filled symbols) and 2 K (open symbols).

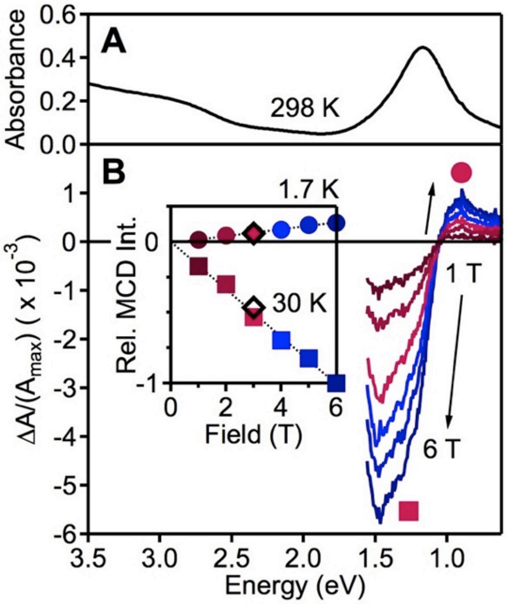

Figure C.4. Temperature- and field-dependent Cu$_{2-x}$Se MCD. (**A**) Room-temperature absorption and (**B**) 1.7 K MCD spectra of d = 16.9 nm p-Cu$_{2-x}$Se nanocrystals. Inset: Relative integrated MCD intensities *vs* magnetic field measured at 1.7 K. Black diamonds represent 3 T MCD intensities at 30 K, demonstrating temperature independence of the MCD signal.

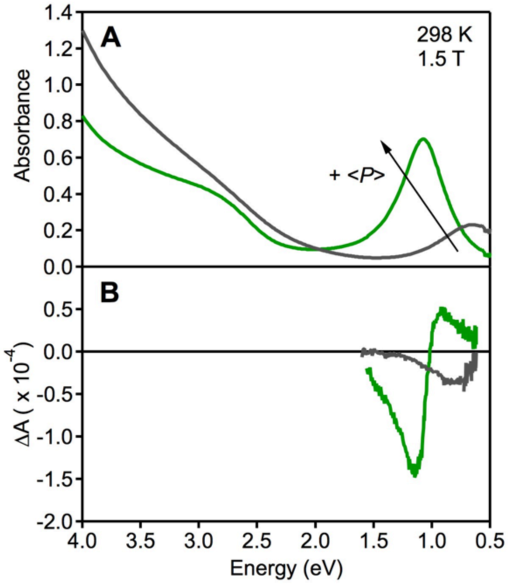

Figure C.5. Cu$_{2-x}$Se MCD with varied carrier density. (**A**) Room-temperature absorption and (**B**) MCD spectra of p-Cu$_{2-x}$Se nanocrystals at different degenerate doping densities $\langle P \rangle$. This representation highlights that the MCD energy tracks the evolution of the LSPR absorption upon oxidation, and its derivative shape is maintained.

C.4 Estimation of Cu_{2-x}Se nanocrystal carrier densities

The IR absorption spectra of heavily doped semiconductor nanocrystals are typically analyzed by invoking the classical Drude model.[9-16] In this model, LSPR frequencies are given by eq C.1, where γ is the scattering frequency, e is the elementary charge, ε_0 is the permittivity of vacuum, ε_m is the medium dielectric, ε_∞ is the high-frequency dielectric, N is the electron density (or P for holes), and m^* is the carrier effective mass. Using this approach and the bulk effective mass, a carrier density of $\langle P \rangle = 2 \times 10^{21}\ \mathrm{cm}^{-3}$ is estimated for the Cu_{2-x}Se nanocrystals shown in Figure 3.1 (Chapter 3).

$$\omega_\mathrm{sp} = \sqrt{\frac{Ne^2}{\varepsilon_0 m^*\left(\varepsilon_\infty + 2\varepsilon_m\right)} - \gamma^2} \tag{C.1}$$

C.5 Comparison of physical parameters, including cyclotron radii (r_C)

The cyclotron radius (r_C) for a given material can be quantified by applying eq C.2, where m^* is the carrier effective mass, v_F is the Fermi velocity, q is the charge of the carrier, and B is the intensity of the magnetic field.

$$\boldsymbol{r_C = \frac{m^* v_\mathrm{F}}{|q|B}} \tag{C.2}$$

Table C.1. Summary of parameters used to describe the materials discussed here.

Sample	<N> or <P> (cm^{-3})	m^* Bulk	m^* MCD	v_F ($\times 10^6$ m/s)	r_c (@ 1T) (nm)	Refs.
Au	5.90×10^{22}	0.99 ± 0.04	–	1.4	79	17,18
Ag	5.85×10^{22}	0.96 ± 0.04	1.0 ± 0.4	1.4	76	17,18
n-ZnO	1.4×10^{20}	0.22 ± 0.08	0.15 ± 0.01	0.84	10	19-21
n-ITO	6×10^{20}	0.35 ± 0.05	0.32 ± 0.06	0.9	18	22-25
p-$Cu_{2-x}Se$	2×10^{21}	0.39 ± 0.06	0.89 ± 0.3	0.53	12	26,27
graphene	$8 \times 10^{12}\ \mathrm{cm}^{-2}$	0.055	–	0.79	2.5	28

C.6 References

1. Dorfs, D.; Härtling, T.; Miszta, K.; Bigall, N. C.; Kim, M. R.; Genovese, A.; Falqui, A.; Povia, M.; Manna, L., Reversible Tunability of the Near-Infrared Valence Band Plasmon Resonance in $Cu_{2-x}Se$ Nanocrystals. *J. Am. Chem. Soc.* **2011,** *133*, 11175-11180.
2. Salvador, M.; MacLeod, B. A.; Hess, A.; Kulkarni, A. P.; Munechika, K.; Chen, J. I. L.; Ginger, D. S., Electron Accumulation on Metal Nanoparticles in Plasmon-Enhanced Organic Solar Cells. *ACS Nano* **2012,** *6*, 10024-10032.
3. Xue, C.; Mirkin, C. A., pH-Switchable Silver Nanoprism Growth Pathways. *Angew. Chem. Int. Ed.* **2007,** *46*, 2036-2038.
4. Pineider, F.; Campo, G.; Bonanni, V.; de Julián Fernández, C.; Mattei, G.; Caneschi, A.; Gatteschi, D.; Sangregorio, C., Circular Magnetoplasmonic Modes in Gold Nanoparticles. *Nano Lett.* **2013,** *13*, 4785-4789.
5. Liu, B.-J.; Lin, K.-Q.; Hu, S.; Wang, X.; Lei, Z.-C.; Lin, H.-X.; Ren, B., Extraction of Absorption and Scattering Contribution of Metallic Nanoparticles Toward Rational Synthesis and Application. *Anal. Chem.* **2015,** *87*, 1058-1065.
6. Piepho, S. B.; Schatz, G. C., *Group Theory in Spectroscopy with Applications to Magnetic Circular Dichroism*. Wiley: New York, **1983**.
7. Lesnyak, V.; George, C.; Genovese, A.; Prato, M.; Casu, A.; Ayyappan, S.; Scarpellini, A.; Manna, L., Alloyed Copper Chalcogenide Nanoplatelets via Partial Cation Exchange Reactions. *ACS Nano* **2014,** *8*, 8407-8418.
8. van der Stam, W.; Akkerman, Q. A.; Ke, X.; van Huis, M. A.; Bals, S.; de Mello Donega, C., Solution-Processable Ultrathin Size- and Shape-Controlled Colloidal $Cu_{2-x}S$ Nanosheets. *Chem. Mater.* **2015,** *27*, 283-291.
9. Nütz, T.; zum Felde, U.; Haase, M., Wet-Chemical Synthesis of Doped Nanoparticles: Blue-Colored Colloids of *n*-Doped SnO_2 :Sb. *J. Chem. Phys.* **1999,** *110*, 12142-12150.
10. Wang, T.; Radovanovic, P. V., Free Electron Concentration in Colloidal Indium Tin Oxide Nanocrystals Determined by Their Size and Structure. *J. Phys. Chem. C* **2011,** *115*, 406-413.
11. Luther, J. M.; Jain, P. K.; Ewers, T.; Alivisatos, A. P., Localized Surface Plasmon Resonances Arising from Free Carriers in Doped Quantum Dots. *Nat. Mater.* **2011,** *10*, 361-366.
12. Niezgoda, J. S.; Harrison, M. A.; McBride, J. R.; Rosenthal, S. J., Novel Synthesis of Chalcopyrite $Cu_xIn_yS_2$ Quantum Dots with Tunable Localized Surface Plasmon Resonances. *Chem. Mater.* **2012,** *24*, 3294-3297.

13. Chou, L. W.; Shin, N.; Sivaram, S. V.; Filler, M. A., Tunable Mid-Infrared Localized Surface Plasmon Resonances in Silicon Nanowires. *J. Am. Chem. Soc.* **2012,** *134*, 16155-16158.
14. Polking, M. J.; Jain, P. K.; Bekenstein, Y.; Banin, U.; Millo, O.; Ramesh, R.; Alivisatos, A. P., Controlling Localized Surface Plasmon Resonances in GeTe Nanoparticles Using an Amorphous-to-Crystalline Phase Transition. *Phys. Rev. Lett.* **2013,** *111*, 037401.
15. Palomaki, P. K. B.; Miller, E. M.; Neale, N. R., Control of Plasmonic and Interband Transitions in Colloidal Indium Nitride Nanocrystals. *J. Am. Chem. Soc.* **2013,** *135*, 14142-14150.
16. Faucheaux, J. A.; Jain, P. K., Plasmons in Photocharged ZnO Nanocrystals Revealing the Nature of Charge Dynamics. *J. Phys. Chem. Lett.* **2013,** *4*, 3024-3030.
17. Johnson, P. B.; Christy, R. W., Optical Constants of the Noble Metals. *Phys. Rev. B* **1972,** *6*, 4370-4379.
18. Omar, M. A., *Elementary Solid State Physics: Principles and Applications*. Addison-Wesley Publishing Company, Inc.: Philippines, **1975**.
19. Madelung, O., *Semiconductors: Data Handbook*. 3rd ed.; Springer: New York, 2004.
20. Morkoç, H.; Özgür, Ü., General Properties of ZnO. In *Zinc Oxide*, Wiley-VCH Verlag GmbH & Co. KGaA: 2009; pp 1-76.
21. Schimpf, A. M.; Thakkar, N.; Gunthardt, C. E.; Masiello, D. J.; Gamelin, D. R., Charge-Tunable Quantum Plasmons in Colloidal Semiconductor Nanocrystals. *ACS Nano* **2014,** *8*, 1065-1072.
22. Lounis, S. D.; Runnerstrom, E. L.; Bergerud, A.; Nordlund, D.; Milliron, D. J., Influence of Dopant Distribution on the Plasmonic Properties of Indium Tin Oxide Nanocrystals. *J. Am. Chem. Soc.* **2014,** *136*, 7110-7116.
23. Preissler, N.; Bierwagen, O.; Ramu, A. T.; Speck, J. S., Electrical Transport, Electrothermal Transport, and Effective Electron Mass in Single-Crystalline In_2O_3 films. *Phys. Rev. B* **2013,** *88*, 1-10.
24. Solieman, A.; Aegerter, M. A., Modeling of Optical and Electrical Properties of In_2O_3:Sn Coatings Made by Various Techniques. *Thin Solid Films* **2006,** *502*, 205-211.
25. Schimpf, A. M.; Runnerstrom, E. L.; Lounis, S. D.; Milliron, D. J.; Gamelin, D. R., Redox Energies and Plasmon Resonance Energies of Photodoped In_2O_3 and Sn-doped In_2O_3 Nanocrystals. *J. Am. Chem. Soc.* **2015,** *137*, 518-524.
26. Mansour, B. A.; Demian, S. E.; Zayed, H. A., Determination of the Effective Mass for Highly Degenerate Copper Selenide from Reflectivity Measurements. *J. Mater. Sci.-Mater. El.* **1992,** *3*, 249-252.
27. Gorbachev, V. V.; Putilin, I. M., Some Parameters of Band Structure in Copper Selenide and Telluride. *Phys. Stat. Sol. A* **1973,** *16*, 553-559.
28. Crassee, I.; Orlita, M.; Potemski, M.; Walter, A. L.; Ostler, M.; Seyller, T.; Gaponenko, I.; Chen, J.; Kuzmenko, A. B., Intrinsic Terahertz Plasmons and Magnetoplasmons in Large Scale Monolayer Graphene. *Nano Lett.* **2012,** *12*, 2470-2474.

Bibliography

Agrawal, A.; Johns, R. W.; Milliron, D. J., Control of Localized Surface Plasmon Resonances in Metal Oxide Nanocrystals. *Annu. Rev. Mater. Res.* **2017,** *47*, 1-31.

Alam, R.; Labine, M.; Karwacki, C. J.; Kamat, P. V., Modulation of $Cu_{2-x}S$ Nanocrystal Plasmon Resonance through Reversible Photoinduced Electron Transfer. *ACS Nano* **2016,** *10*, 2880-2886.

Asami, K.; Nishi, H.; Tatsuma, T., Electrochemical Redox-Based Tuning of Near Infrared Localized Plasmons of CuS Nanoplates. *Nanoscale* **2016,** *8*, 14092-14096.

Araujo, J.; Brozek, C. K.; Kroupa, D. M.; Gamelin, D. R., Degenerately *n*-Doped Colloidal PbSe Quantum Dots: Band Assignments and Electrostatic Effects. *Submitted* **2018**.

Armelles, G.; Cebollada, A.; Garcia-Martin, A.; Gonzalez, M. U., Magnetoplasmonics: Combining Magnetic and Plasmonic Functionalities. *Adv. Opt. Mater.* **2013,** *1*, 10-35.

Artemyev, M.; Krutokhvostov, R.; Melnikau, D.; Oleinikov, V.; Sukhanova, A.; Nabiev, I., Low-Field Magnetic Circular Dichroism in Silver and Gold Colloidal Nanoparticles of Different Sizes, Shapes, and Aggregation States. *Proc. SPIE* **2012,** *8457*, 845729.

Beaulac, R.; Archer, P. I.; Ochsenbein, S. T.; Gamelin, D. R., Mn^{2+}-Doped CdSe Quantum Dots: New Inorganic Materials for Spin-Electronics and Spin-Photonics. *Adv. Funct. Mater.* **2008,** *18*, 3873-3891.

Beaulac, R.; Ochsenbein, S. T.; Gamelin, D. R., Colloidal Transition-Metal-Doped Quantum Dots. In *Nanocrystal Quantum Dots, 2nd ed.*, CRC Press: Boca Raton, FL, 2010; pp 397-453.

Beberwyck, B. J.; Surendranath, Y.; Alivisatos, A. P., Cation Exchange: A Versatile Tool for Nanomaterials Synthesis. *J. Phys. Chem. C* **2013,** *117*, 19759-19770.

Bekenstein, Y.; Vinokurov, K.; Keren-Zur, S.; Hadar, I.; Schilt, Y.; Raviv, U.; Millo, O.; Banin, U., Thermal Doping by Vacancy Formation in Copper Sulfide Nanocrystal Arrays. *Nano Lett.* **2014,** *14*, 1349-1353.

Boehme, S. C.; Wang, H.; Siebbeles, L. D. A.; Vanmaekelbergh, D.; Houtepen, A. J., Electrochemical Charging of CdSe Quantum Dot Films: Dependence on Void Size and Counterion Proximity. *ACS Nano* **2013,** *7*, 2500-2508.

Boles, M. A.; Ling, D.; Hyeon, T.; Talapin, D. V., The Surface Science of Nanocrystals. *Nat. Mater.* **2016,** *15*, 141-153.

Brozek, C. K.; Hartstein, K. H.; Gamelin, D. R., Potentiometric Titrations for Measuring the Capacitance of Colloidal Photodoped ZnO Nanocrystals. *J. Am. Chem. Soc.* **2016,** *138*, 10605-10610.

Buonsanti, R.; Llordes, A.; Aloni, S.; Helms, B.; Milliron, D., Tunable Infrared Absorption and Visible Transparency of Colloidal Aluminum-Doped Zinc Oxide Nanocrystals. *Nano Lett.* **2011,** *11*, 4706-4716.

Carroll, G. M.; Brozek, C. K.; Hartstein, K. H.; Tsui, E. Y.; Gamelin, D. R., Potentiometric Measurements of Semiconductor Nanocrystal Redox Potentials. *J. Am. Chem. Soc.* **2016,** *138*, 4310-4313.

Carroll, G. M.; Schimpf, A. M.; Tsui, E. Y.; Gamelin, D. R., Redox Potentials of Colloidal *n*-Type ZnO Nanocrystals: Effects of Confinement, Electron Density, and Fermi-Level Pinning by Aldehyde Hydrogenation. *J. Am. Chem. Soc.* **2015,** *137*, 11163-11169.

Carroll, G. M.; Tsui, E. Y.; Brozek, C. K.; Gamelin, D. R., Spectroelectrochemical Measurement of Surface Electrostatic Contributions to Colloidal CdSe Nanocrystal Redox Potentials. *Chem. Mater.* **2016,** *28*, 7912-7918.

Chen, O.; Zhao, J.; Chauhan, V. P.; Cui, J.; Wong, C.; Harris, D. K.; Wei, H.; Han, H.-S.; Fukumura, D.; Jain, R. K.; Bawendi, M. G., Compact High-Quality CdSe–CdS Core–Shell Nanocrystals with Narrow Emission Linewidths and Suppressed Blinking. *Nat. Mater.* **2013,** *12*, 445-451.

Chen, Y.; Vela, J.; Htoon, H.; Casson, J. L.; Werder, D. J.; Bussian, D. A.; Klimov, V. I.; Hollingsworth, J. A., “Giant” Multishell CdSe Nanocrystal Quantum Dots with Suppressed Blinking. *J. Am. Chem. Soc.* **2008,** *130*, 5026-5027.

Chou, L. W.; Shin, N.; Sivaram, S. V.; Filler, M. A., Tunable Mid-Infrared Localized Surface Plasmon Resonances in Silicon Nanowires. *J. Am. Chem. Soc.* **2012,** *134*, 16155-16158.

Cohn, A. W.; Janßen, N.; Mayer, J. M.; Gamelin, D. R., Photocharging ZnO Nanocrystals: Picosecond Hole Capture, Electron Accumulation, and Auger Recombination. *J. Phys. Chem. C* **2012,** *116*, 20633-20642.

Cohn, A. W.; Rinehart, J. D.; Schimpf, A. M.; Weaver, A. L.; Gamelin, D. R. Size Dependence of Negative Trion Auger Recombination in Photodoped CdSe Nanocrystals. *Nano Lett.* **2013**, *14*, 353-358.

Comin, A.; Manna, L., New Materials for Tunable Plasmonic Colloidal Nanocrystals. *Chem. Soc. Rev.* **2014,** *43*, 3957-3975.

Coropceanu, I.; Bawendi, M. G., Core/Shell Quantum Dot Based Luminescent Solar Concentrators with Reduced Reabsorption and Enhanced Efficiency. *Nano Lett.* **2014,** *14*, 4097-4101.

Coughlan, C.; Ibáñez, M.; Dobrozhan, O.; Singh, A.; Cabot, A.; Ryan, K. M., Compound Copper Chalcogenide Nanocrystals. *Chem. Rev.* **2017,** *117*, 5865-6109.

Crassee, I.; Orlita, M.; Potemski, M.; Walter, A. L.; Ostler, M.; Seyller, T.; Gaponenko, I.; Chen, J.; Kuzmenko, A. B., Intrinsic Terahertz Plasmons and Magnetoplasmons in Large Scale Monolayer Graphene. *Nano Lett.* **2012,** *12*, 2470-2474.

Crockett, B. M.; Jansons, A. W.; Koskela, K. M.; Johnson, D. W.; Hutchison, J. E., Radial Dopant Placement for Tuning Plasmonic Properties in Metal Oxide Nanocrystals. *ACS Nano* **2017,** *11*, 7719-7728.

De Trizio, L.; Buonsanti, R.; Schimpf, A. M.; Llordes, A.; Gamelin, D. R.; Simonutti, R.; Milliron, D. J., Nb-Doped Colloidal TiO_2 Nanocrystals with Tunable Infrared Absorption. *Chem. Mater.* **2013,** *25*, 3383-3390.

De Trizio, L.; Manna, L., Forging Colloidal Nanostructures via Cation Exchange Reactions. *Chem. Rev.* **2016,** *116*, 10852-10887.

Dorfs, D.; Härtling, T.; Miszta, K.; Bigall, N. C.; Kim, M. R.; Genovese, A.; Falqui, A.; Povia, M.; Manna, L., Reversible Tunability of the Near-Infrared Valence Band Plasmon Resonance in $Cu_{2-x}Se$ Nanocrystals. *J. Am. Chem. Soc.* **2011,** *133*, 11175-11180.

Edwards, P. P.; Porch, A.; Jones, M. O.; Morgan, D. V.; Perks, R. M., Basic Materials Physics of Transparent Conducting Oxides. *Dalton Transactions* **2004**, 2995-3002.

Efros, A. L.; Rosen, M., The Electronic Structure of Semiconductor Nanocrystals. *Annu. Rev. Mater. Sci.* **2000,** *30*, 475-521.

Ehrat, F.; Simon, T.; Stolarczyk, J. K.; Feldmann, J., Size Effects on Photocatalytic H_2 Generation with CdSe/CdS Core-Shell Nanocrystals. *Z. Phys. Chem.* **2015,** *229*, 205-219.

Elimelech, O.; Liu, J.; Plonka, A. M.; Frenkel, A. I.; Banin, U., Size Dependence of Doping *via* Vacancy Formation in Copper Sulfide Nanocrystals. *Angew. Chem. Int. Ed.* **2017,** *56*, 10335-10340.

Fang, H.; Hegde, M.; Yin, P.; Radovanovic, P. V., Tuning Plasmon Resonance of In_2O_3 Nanocrystals Throughout the Mid-Infrared Region by Competition between Electron Activation and Trapping. *Chem. Mater.* **2017,** *29*, 4970-4979.

Faucheaux, J. A.; Jain, P. K., Plasmons in Photocharged ZnO Nanocrystals Revealing the Nature of Charge Dynamics. *J. Phys. Chem. Lett.* **2013,** *4*, 3024-3030.

Fukuzumi, S.; Ohkubo, K., Metal Ion-Coupled and Decoupled Electron Transfer. *Coord. Chem. Rev.* **2010,** *254*, 372-385.

Fukuzumi, S.; Ohkubo, K.; Morimoto, Y., Mechanisms of Metal Ion-Coupled Electron Transfer. *Phys. Chem. Chem. Phys.* **2012,** *14*, 8472-8484.

Galland, C.; Ghosh, Y.; Steinbrück, A.; Hollingsworth, J. A.; Htoon, H.; Klimov, V. I., Lifetime Blinking in Nonblinking Nanocrystal Quantum Dots. *Nat. Commun.* **2012,** *3*, 908.

Garcia, G.; Buonsanti, R.; Runnerstrom, E. L.; Mendelsberg, R. J.; Llordes, A.; Anders, A.; Richardson, T. J.; Milliron, D. J., Dynamically Modulating the Surface Plasmon Resonance of Doped Semiconductor Nanocrystals. *Nano Lett.* **2011,** *11*, 4415-4420.

Germeau, A.; Roest, A. L.; Vanmaekelbergh, D.; Allan, G.; Delerue, C.; Meulenkamp, E. A., Optical Transitions in Artificial Few-Electron Atoms Strongly Confined Inside ZnO Nanocrystals. *Phys. Rev. Lett.* **2003,** *90*, 097401.

Gorbachev, V. V.; Putilin, I. M., Some Parameters of Band Structure in Copper Selenide and Telluride. *Phys. Stat. Sol. A* **1973,** *16*, 553-559.

Guyot-Sionnest, P., Charging Colloidal Quantum Dots by Electrochemistry. *Microchim. Acta* **2008,** *160*, 309-314.

Haase, M.; Weller, H.; Henglein, A., Photochemistry and Radiation Chemistry of Colloidal Semiconductors. 23. Electron Storage on ZnO Particles and Size Quantization. *J. Phys. Chem.* **1988,** *92*, 482-487.

Hartstein, K. H.; Erickson, C. S.; Tsui, E. Y.; Marchioro, A.; Gamelin, D. R., Electron Stability and Negative-Tetron Luminescence in Free-Standing Colloidal *n*-Type CdSe/CdS Quantum Dots. *ACS Nano* **2017,** *11*, 10430-10438.Hartstein, K. H.; Schimpf, A. M.; Salvador, M.; Gamelin, D. R. Cyclotron Splittings in the Plasmon Resonances of Electronically Doped Semiconductor Nanocrystals Probed by Magnetic Circular Dichroism Spectroscopy. *J. Phys. Chem. Lett.* **2017**, *8,* 1831-1836.

Hayoun, R.; Whitaker, K. M.; Gamelin, D. R.; Mayer, J. M., Electron Transfer Between Colloidal ZnO Nanocrystals. *J. Am. Chem. Soc.* **2011,** *133*, 4228-4231.

Hsu, S.-W.; Bryks, W.; Tao, A. R., Effects of Carrier Density and Shape on the Localized Surface Plasmon Resonances of $Cu_{2-x}S$ Nanodisks. *Chem. Mater.* **2012,** *24*, 3765-3771.

Hsu, S.-W.; On, K.; Tao, A. R., Localized Surface Plasmon Resonances of Anisotropic Semiconductor Nanocrystals. *J. Am. Chem. Soc.* **2011,** *133*, 19072-19075.

Ishikawa, Y.; Yao, H., Surface Magnetoplasmons in Silver Nanoparticles: Apparent Magnetic-Field Enhancement Manifested by Simultaneous Deconvolution of UV–Vis Absorption and MCD Spectra. *Chem. Phys. Lett.* **2014,** *609*, 93-97.

Jain, P. K.; Manthiram, K.; Engel, J. H.; White, S. L.; Faucheaux, J. A.; Alivisatos, A. P., Doped Nanocrystals as Plasmonic Probes of Redox Chemistry. *Angew. Chem. Int. Ed.* **2013,** *52*, 13671-13675.

Jha, P. P.; Guyot-Sionnest, P., Photoluminescence Switching of Charged Quantum Dot Films. *J. Phys. Chem. C* **2007,** *111*, 15440-15445.

Jha, P. P.; Guyot-Sionnest, P., Trion Decay in Colloidal Quantum Dots. *ACS Nano* **2009,** *3*, 1011-1015.

Johnson, P. B.; Christy, R. W., Optical Constants of the Noble Metals. *Phys. Rev. B* **1972,** *6*, 4370-4379.

Kalevich, V. K.; Merkulov, I. A.; Shiryaev, A. Y.; Kavokin, K. V.; Ikezawa, M.; Okuno, T.; Brunkov, P. N.; Zhukov, A. E.; Ustinov, V. M.; Masumoto, Y., Optical Spin Polarization and Exchange Interaction in Doubly Charged InAs Self-Assembled Quantum Dots. *Phys. Rev. B* **2005,** *72*, 045325.

Kanehara, M.; Koike, H.; Yoshinaga, T.; Teranishi, T., Indium Tin Oxide Nanoparticles with Compositionally Tunable Surface Plasmon Resonance Frequencies in the Near-IR Region. *J. Am. Chem. Soc.* **2009,** *131*, 17736-17737.

Kasap, S., *Principles of Electronic Materials and Devices*. 2nd ed.; McGraw-Hill: New York, NY, 2002.

Koh, W.-K.; Koposov, A. Y.; Stewart, J. T.; Pal, B. N.; Robel, I.; Pietryga, J. M.; Klimov, V. I., Heavily Doped *n*-Type PbSe and PbS Nanocrystals Using Ground-State Charge Transfer from Cobaltocene. *Sci. Rep.* **2013,** *3*, 1-8.

Kovalenko, M. V.; Manna, L.; Cabot, A.; Hens, Z.; Talapin, D. V.; Kagan, C. R.; Klimov, V. I.; Rogach, A. L.; Reiss, P.; Milliron, D. J.; Guyot-Sionnest, P.; Konstantatos, G.; Parak, W. J.; Hyeon, T.; Korgel, B. A.; Murray, C. B.; Heiss, W., Prospects of Nanoscience with Nanocrystals. *ACS Nano* **2015,** *9*, 1012-1057.

Kriegel, I.; Jiang, C.; Rodríguez-Fernández, J.; Schaller, R. D.; Talapin, D. V.; da Como, E.; Feldmann, J., Tuning the Excitonic and Plasmonic Properties of Copper Chalcogenide Nanocrystals. *J. Am. Chem. Soc.* **2011,** *134*, 1583-1590.

Kriegel, I.; Rodríguez-Fernández, J.; Wisnet, A.; Zhang, H.; Waurisch, C.; Eychmüller, A.; Dubavik, A.; Govorov, A. O.; Feldmann, J., Shedding Light on Vacancy-Doped Copper Chalcogenides: Shape-Controlled Synthesis, Optical Properties, and Modeling of Copper Telluride Nanocrystals with Near-Infrared Plasmon Resonances. *ACS Nano* **2013,** *7*, 4367-4377.

Kriegel, I.; Scotognella, F.; Manna, L., Plasmonic Doped Semiconductor Nanocrystals: Properties, Fabrication, Applications and Perspectives. *Phys. Rep.* **2017,** *674*, 1-52.

Kroupa, D. M.; Hughes, B. K.; Miller, E. M.; Moore, D. T.; Anderson, N. C.; Chernomordik, B. D.; Nozik, A. J.; Beard, M. C., Synthesis and Spectroscopy of Silver-Doped PbSe Quantum Dots. *J. Am. Chem. Soc.* **2017,** *139*, 10382-10394.

Lesnyak, V.; George, C.; Genovese, A.; Prato, M.; Casu, A.; Ayyappan, S.; Scarpellini, A.; Manna, L., Alloyed Copper Chalcogenide Nanoplatelets via Partial Cation Exchange Reactions. *ACS Nano* **2014,** *8*, 8407-8418.

Lhuillier, E.; Guyot-Sionnest, P., Recent Progresses in Mid Infrared Nanocrystal Based Optoelectronics. *IEEE J. Sel. Top. Quant. Electr.* **2017,** *23*, 1-8.

Li, J. J.; Wang, Y. A.; Guo, W.; Keay, J. C.; Mishima, T. D.; Johnson, M. B.; Peng, X., Large-Scale Synthesis of Nearly Monodisperse CdSe/CdS Core/Shell Nanocrystals Using Air-Stable Reagents *via* Successive Ion Layer Adsorption and Reaction. *J. Am. Chem. Soc.* **2003,** *125*, 12567-12575.

Liu, B.-J.; Lin, K.-Q.; Hu, S.; Wang, X.; Lei, Z.-C.; Lin, H.-X.; Ren, B., Extraction of Absorption and Scattering Contribution of Metallic Nanoparticles Toward Rational Synthesis and Application. *Anal. Chem.* **2015,** *87*, 1058-1065.

Liu, H.; Brozek, C. K.; Sun, S.; Lingerfelt, D. B.; Gamelin, D. R.; Li, X., A Hybrid Quantum-Classical Model of Electrostatics in Multiply Charged Quantum Dots. *J. Phys. Chem. C* **2017,** *121*, 26086-26095.

Liu, Y.; Liu, M.; Swihart, M. T., Plasmonic Copper Sulfide-Based Materials: A Brief Introduction to Their Synthesis, Doping, Alloying, and Applications. *J. Phys. Chem. C* **2017,** *121*, 13435-13447.

Liu, W. K.; Whitaker, K. M.; Kittilstved, K. R.; Gamelin, D. R., Stable Photogenerated Carriers in Magnetic Semiconductor Nanocrystals. *J. Am. Chem. Soc.* **2006,** *128*, 3910-3911.

Liu, W. K.; Whitaker, K. M.; Smith, A. L.; Kittilstved, K. R.; Robinson, B. H.; Gamelin, D. R., Room-Temperature Electron Spin Dynamics in Free-Standing ZnO Quantum Dots. *Phys. Rev. Lett.* **2007,** *98*, 186804.

Liu, Z.; Beaulac, R., Nature of the Infrared Transition of Colloidal Indium Nitride Nanocrystals: Nonparabolicity Effects on the Plasmonic Behavior of Doped Semiconductor Nanomaterials. *Chem. Mater.* **2017,** *29*, 7507-7514.

Llorente, V. B.; Dzhagan, V. M.; Gaponik, N.; Iglesias, R. A.; Zahn, D. R. T.; Lesnyak, V., Electrochemical Tuning of Localized Surface Plasmon Resonance in Copper Chalcogenide Nanocrystals. *J. Phys. Chem. C* **2017,** *121*, 18244-18253.

Lounis, S. D.; Runnerstrom, E. L.; Bergerud, A.; Nordlund, D.; Milliron, D. J., Influence of Dopant Distribution on the Plasmonic Properties of Indium Tin Oxide Nanocrystals. *J. Am. Chem. Soc.* **2014,** *136*, 7110-7116.

Lukashev, P.; Lambrecht, W. R. L.; Kotani, T.; van Schilfgaarde, M., Electronic and Crystal Structure of $Cu_{2-x}S$: Full-Potential Electronic Structure Calculations. *Phys. Rev. B* **2007,** *76*, 195202.

Luther, J. M.; Jain, P. K.; Ewers, T.; Alivisatos, A. P., Localized Surface Plasmon Resonances Arising from Free Carriers in Doped Quantum Dots. *Nat. Mater.* **2011,** *10*, 361-366.

Madelung, O., *Semiconductors: Data Handbook*. 3rd ed.; Springer: New York, **2004**.

Mahler, B.; Spinicelli, P.; Buil, S.; Quelin, X.; Hermier, J.-P.; Dubertret, B., Towards Non-Blinking Colloidal Quantum Dots. *Nat. Mater.* **2008,** *7*, 659-664.

Malko, A. V.; Park, Y.-S.; Sampat, S.; Galland, C.; Vela, J.; Chen, Y.; Hollingsworth, J. A.; Klimov, V. I.; Htoon, H., Pump-Intensity- and Shell-Thickness-Dependent Evolution of Photoluminescence Blinking in Individual Core/Shell CdSe/CdS Nanocrystals. *Nano Lett.* **2011,** *11*, 5213-5218.

Mansour, B. A.; Demian, S. E.; Zayed, H. A., Determination of the Effective Mass for Highly Degenerate Copper Selenide from Reflectivity Measurements. *J. Mater. Sci.-Mater. El.* **1992,** *3*, 249-252.

Manthiram, K.; Alivisatos, A., Tunable Localized Surface Plasmon Resonances in Tungsten Oxide Nanocrystals. *J. Am. Chem. Soc.* **2012,** *134*, 3995-3998.

Mendelsberg, R. J.; Garcia, G.; Li, H.; Manna, L.; Milliron, D. J., Understanding the Plasmon Resonance in Ensembles of Degenerately Doped Semiconductor Nanocrystals. *J. Phys. Chem. C* **2012,** *116*, 12226-12231.

Morkoç, H.; Özgür, Ü., General Properties of ZnO. In *Zinc Oxide*, Wiley-VCH Verlag GmbH & Co. KGaA: **2009**; pp 1-76.

Nelson, H. D.; Bradshaw, L. R.; Barrows, C. J.; Vlaskin, V. A.; Gamelin, D. R., Picosecond Dynamics of Excitonic Magnetic Polarons in Colloidal Diffusion-Doped $Cd_{1-x}Mn_xSe$ Quantum Dots. *ACS Nano* **2015,** *9*, 11177-11191.

Niezgoda, J. S.; Harrison, M. A.; McBride, J. R.; Rosenthal, S. J., Novel Synthesis of Chalcopyrite $Cu_xIn_yS_2$ Quantum Dots with Tunable Localized Surface Plasmon Resonances. *Chem. Mater.* **2012,** *24*, 3294-3297.

Nütz, T.; zum Felde, U.; Haase, M., Wet-Chemical Synthesis of Doped Nanoparticles: Blue-Colored Colloids of *n*-Doped SnO_2:Sb. *J. Chem. Phys.* **1999,** *110*, 12142-12150.

Ochsenbein, S. T.; Feng, Y.; Whitaker, K. M.; Badaeva, E.; Liu, W. K.; Li, X.; Gamelin, D. R., Charge-Controlled Magnetism in Colloidal Doped Semiconductor Nanocrystals. *Nat. Nanotechnol.* **2009,** *4*, 681-687.

Omar, M. A., *Elementary Solid State Physics: Principles and Applications*. Addison-Wesley Publishing Company, Inc.: Philippines, **1975**.

Palomaki, P. K. B.; Miller, E. M.; Neale, N. R., Control of Plasmonic and Interband Transitions in Colloidal Indium Nitride Nanocrystals. *J. Am. Chem. Soc.* **2013,** *135*, 14142-14150.

Park, Y.-S.; Bae, W. K.; Pietryga, J. M.; Klimov, V. I., Auger Recombination of Biexcitons and Negative and Positive Trions in Individual Quantum Dots. *ACS Nano* **2014,** *8*, 7288-7296.

Pelton, M.; Smith, G.; Scherer, N. F.; Marcus, R. A., Evidence for a Diffusion-Controlled Mechanism for Fluorescence Blinking of Colloidal Quantum Dots. *Proc. Natl. Acad. Sci.* **2007,** *104*, 14249.

Peng, X.; Schlamp, M. C.; Kadavanich, A. V.; Alivisatos, A. P., Epitaxial Growth of Highly Luminescent CdSe/CdS Core/Shell Nanocrystals with Photostability and Electronic Accessibility. *J. Am. Chem. Soc.* **1997,** *119*, 7019-7029.

Piepho, S. B.; Schatz, G. C., *Group Theory in Spectroscopy with Applications to Magnetic Circular Dichroism*. Wiley: New York, **1983**.

Pineider, F.; Campo, G.; Bonanni, V.; de Julián Fernández, C.; Mattei, G.; Caneschi, A.; Gatteschi, D.; Sangregorio, C., Circular Magnetoplasmonic Modes in Gold Nanoparticles. *Nano Lett.* **2013,** *13*, 4785-4789.

Polking, M. J.; Jain, P. K.; Bekenstein, Y.; Banin, U.; Millo, O.; Ramesh, R.; Alivisatos, A. P., Controlling Localized Surface Plasmon Resonances in GeTe Nanoparticles Using an Amorphous-to-Crystalline Phase Transition. *Phys. Rev. Lett.* **2013,** *111*, 037401.

Pradhan, N.; Adhikari, S. D.; Nag, A.; Sarma, D. D., Luminescence, Plasmonic, and Magnetic Properties of Doped Semiconductor Nanocrystals. *Angew. Chem. Int. Ed.* **2017,** *56*, 7038-7054.

Preissler, N.; Bierwagen, O.; Ramu, A. T.; Speck, J. S., Electrical Transport, Electrothermal Transport, and Effective Electron Mass in Single-Crystalline In_2O_3 films. *Phys. Rev. B* **2013,** *88*, 1-10.

Qu, L.; Peng, X., Control of Photoluminescence Properties of CdSe Nanocrystals in Growth. *J. Am. Chem. Soc.* **2002,** *124*, 2049-2055.

Rabouw, F. T.; Vaxenburg, R.; Bakulin, A. A.; Dijk-Moes, R. J. A. v.; Bakker, H. J.; Rodina, A.; Lifshitz, E.; Efros, A. L.; Koenderink, A. F.; Vanmaekelbergh, D., Dynamics of Intraband and Interband Auger Processes in Colloidal Core–Shell Quantum Dots. *ACS Nano* **2015,** *9*, 10366-10376.

Rinehart, J. D.; Schimpf, A. M.; Weaver, A. L.; Cohn, A. W.; Gamelin, D. R., Photochemical Electronic Doping of Colloidal CdSe Nanocrystals. *J. Am. Chem. Soc.* **2013,** *135*, 18782-18785.

Rivest, J. B.; Jain, P. K., Cation Exchange on the Nanoscale: An Emerging Technique for New Material Synthesis, Device Fabrication, and Chemical Sensing. *Chem. Soc. Rev.* **2013,** *42*, 89-96.

Routzahn, A. L.; White, S. L.; Fong, L.-K.; Jain, P. K., Plasmonics with Doped Quantum Dots. *Israel J. Chem.* **2012,** *52*, 983-991.

Saba, M.; Aresti, M.; Quochi, F.; Marceddu, M.; Loi, M. A.; Huang, J.; Talapin, D. V.; Mura, A.; Bongiovanni, G., Light-Induced Charged and Trap States in Colloidal Nanocrystals Detected by Variable Pulse Rate Photoluminescence Spectroscopy. *ACS Nano* **2013,** *7*, 229-238.

Salvador, M.; MacLeod, B. A.; Hess, A.; Kulkarni, A. P.; Munechika, K.; Chen, J. I. L.; Ginger, D. S., Electron Accumulation on Metal Nanoparticles in Plasmon-Enhanced Organic Solar Cells. *ACS Nano* **2012,** *6*, 10024-10032.

Sampat, S.; Karan, N. S.; Guo, T.; Htoon, H.; Hollingsworth, J. A.; Malko, A. V., Multistate Blinking and Scaling of Recombination Rates in Individual Silica-Coated CdSe/CdS Nanocrystals. *ACS Photonics* **2015,** *2*, 1505-1512.

Schimpf, A. M.; Gunthardt, C. E.; Rinehart, J. D.; Mayer, J. M.; Gamelin, D. R., Controlling Carrier Densities in Photochemically Reduced Colloidal ZnO Nanocrystals: Size Dependence and Role of the Hole Quencher. *J. Am. Chem. Soc.* **2013,** *135*, 16569-16577.

Schimpf, A. M.; Knowles, K. E.; Carroll, G. M.; Gamelin, D. R., Electronic Doping and Redox Potential Tuning in Colloidal Semiconductor Nanocrystals. *Acc. Chem. Res.* **2015,** *48*, 1929-1937.

Schimpf, A. M.; Ochsenbein, S. T.; Buonsanti, R.; Milliron, D. J.; Gamelin, D. R., Comparison of Extra Electrons in Colloidal *n*-Type Al^{3+}-Doped and Photochemically Reduced ZnO Nanocrystals. *Chem. Commun.* **2012,** *48*, 9352-9354.

Schimpf, A. M.; Rinehart, J. D.; Ochsenbein, S. T.; Gamelin, D. R., Charge-State Control of Mn^{2+} Spin Relaxation Dynamics in Colloidal *n*−Type $Zn_{1-x}Mn_xO$ Nanocrystals. *J. Phys. Chem. Lett.* **2015,** *6*, 1748-1753.

Schimpf, A. M.; Runnerstrom, E. L.; Lounis, S. D.; Milliron, D. J.; Gamelin, D. R., Redox Energies and Plasmon Resonance Energies of Photodoped In_2O_3 and Sn-doped In_2O_3 Nanocrystals. *J. Am. Chem. Soc.* **2015,** *137*, 518-524.

Schimpf, A. M.; Thakkar, N.; Gunthardt, C. E.; Masiello, D. J.; Gamelin, D. R., Charge-Tunable Quantum Plasmons in Colloidal Semiconductor Nanocrystals. *ACS Nano* **2014,** *8*, 1065-1072.

Scotognella, F.; Della Valle, G.; Srimath Kandada, A. R.; Dorfs, D.; Zavelani-Rossi, M.; Conforti, M.; Miszta, K.; Comin, A.; Korobchevskaya, K.; Lanzani, G.; Manna, L.; Tassone, F., Plasmon Dynamics in Colloidal $Cu_{2-x}Se$ Nanocrystals. *Nano Lett.* **2011,** *11*, 4711-4717.

Scotognella, F.; Valle, G.; Srimath Kandada, A.; Zavelani-Rossi, M.; Longhi, S.; Lanzani, G.; Tassone, F., Plasmonics in Heavily-Doped Semiconductor Nanocrystals. *Eur. Phys. J. B* **2013,** *86*, 1-13.

Shim, M.; Guyot-Sionnest, P., Organic-Capped ZnO nanocrystals: Synthesis and *n*-Type Character. *J. Am. Chem. Soc.* **2001,** *123*, 11651-11654.

Shim, M.; Wang, C.; Guyot-Sionnest, P., Charge-Tunable Optical Properties in Colloidal Semiconductor Nanocrystals. *J. Phys. Chem. B* **2001,** *105*, 2369-2373.

Shimizu, K. T.; Neuhauser, R. G.; Leatherdale, C. A.; Empedocles, S. A.; Woo, W. K.; Bawendi, M. G., Blinking Statistics in Single Semiconductor Nanocrystal Quantum Dots. *Phys. Rev. B* **2001,** *63*, 205316.

Smith, A. M.; Nie, S., Semiconductor Nanocrystals: Structure, Properties, and Band Gap Engineering. *Acc. Chem. Res.* **2010,** *43*, 190-200.

Solieman, A.; Aegerter, M. A., Modeling of Optical and Electrical Properties of In_2O_3:Sn Coatings Made by Various Techniques. *Thin Solid Films* **2006,** *502*, 205-211.

Steiner, D.; Dorfs, D.; Banin, U.; Della Sala, F.; Manna, L.; Millo, O., Determination of Band Offsets in Heterostructured Colloidal Nanorods Using Scanning Tunneling Spectroscopy. *Nano Lett.* **2008,** *8*, 2954-2958.

Stern, N. P.; Poggio, M.; Bartl, M. H.; Hu, E. L.; Stucky, G. D.; Awschalom, D. D., Spin Dynamics in Electrochemically Charged CdSe Quantum Dots. *Phys. Rev. B* **2005,** *72*, 161303.

Tang, A.; Qu, S.; Li, K.; Hou, Y.; Teng, F.; Cao, J.; Wang, Y.; Wang, Z. One-Pot Synthesis and Self-Assembly of Colloidal Copper(I) Sulfide Nanocrystals. *Nanotechnology* **2010**, *21*, 285602.

Tang, J.; Marcus, R. A., Mechanisms of Fluorescence Blinking in Semiconductor Nanocrystal Quantum Dots. *J. Chem. Phys.* **2005,** *123*, 054704.

Tsui, E. Y.; Carroll, G. M.; Miller, B.; Marchioro, A.; Gamelin, D. R., Extremely Slow Spontaneous Electron Trapping in Photodoped *n*-Type CdSe Nanocrystals. *Chem. Mater.* **2017,** *29*, 3754-3762.

Tsui, E. Y.; Hartstein, K. H.; Gamelin, D. R., Selenium Redox Reactivity on Colloidal CdSe Quantum Dot Surfaces. *J. Am. Chem. Soc.* **2016,** *138*, 11105-11108.

Vanmaekelbergh, D.; Liljeroth, P., Electron-Conducting Quantum Dot Solids: Novel Materials Based on Colloidal Semiconductor Nanocrystals. *Chem. Soc. Rev.* **2005,** *34*, 299-312.

van der Stam, W.; Akkerman, Q. A.; Ke, X.; van Huis, M. A.; Bals, S.; de Mello Donega, C., Solution-Processable Ultrathin Size- and Shape-Controlled Colloidal $Cu_{2-x}S$ Nanosheets. *Chem. Mater.* **2015,** *27*, 283-291.

van der Stam, W.; Berends, A. C.; de Mello Donega, C., Prospects of Colloidal Copper Chalcogenide Nanocrystals. *Chem. Phys. Chem.* **2016,** *17*, 559-581.

van der Stam, W.; Gudjonsdottir, S.; Evers, W. H.; Houtepen, A. J., Switching between Plasmonic and Fluorescent Copper Sulfide Nanocrystals. *J. Am. Chem. Soc.* **2017,** *139*, 13208-13217.

Vinokurov, K.; Elimelech, O.; Millo, O.; Banin, U., Copper Sulfide Nanocrystal Level Structure and Electrochemical Functionality towards Sensing Applications. *Chem. Phys. Chem.* **2016,** *17*, 675-680.

Vlaskin, V. A.; Barrows, C. J.; Erickson, C. S.; Gamelin, D. R., Nanocrystal Diffusion Doping. *J. Am. Chem. Soc.* **2013,** *135*, 14380-14389.

Wang, C.; Shim, M.; Guyot-Sionnest, P., Electrochromic Nanocrystal Quantum Dots. *Science* **2001,** *291*, 2390-2392.

Wang, C.; Wehrenberg, B. L.; Woo, C. Y.; Guyot-Sionnest, P., Light Emission and Amplification in Charged CdSe Quantum Dots. *J. Phys. Chem. B* **2004,** *108*, 9027-9031.

Wang, T.; Radovanovic, P. V., Free Electron Concentration in Colloidal Indium Tin Oxide Nanocrystals Determined by Their Size and Structure. *J. Phys. Chem. C* **2011,** *115*, 406-413.

Wang, Y.; Runnerstrom, E. L.; Milliron, D. J., Switchable Materials for Smart Windows. *Annu. Rev. Chem. Biomol. Eng.* **2016,** *7*, 283-304.

Wehrenberg, B. L.; Guyot-Sionnest, P., Electron and Hole Injection in PbSe Quantum Dot Films. *J. Am. Chem. Soc.* **2003,** *125*, 7806-7807.

Weick, G.; Weinmann, D., Lifetime of the Surface Magnetoplasmons in Metallic Nanoparticles. *Phys. Rev. B* **2011,** *83*, 1-10.

Whitaker, K. M.; Ochsenbein, S. T.; Polinger, V. Z.; Gamelin, D. R., Electron Confinement Effects in the EPR Spectra of Colloidal *n*-Type ZnO Quantum Dots. *J. Phys. Chem. C* **2008,** *112*, 14331-14335.

Wood, A.; Giersig, M.; Mulvaney, P., Fermi Level Equilibration in Quantum Dot-Metal Nanojunctions. *J. Phys. Chem. B* **2001,** *105*, 8810-8815.

Wu, K.; Lim, J.; Klimov, V. I., Superposition Principle in Auger Recombination of Charged and Neutral Multicarrier States in Semiconductor Quantum Dots. *ACS Nano* **2017,** *11*, 8437-8447.

Xie, Y.; Riedinger, A.; Prato, M.; Casu, A.; Genovese, A.; Guardia, P.; Sottini, S.; Sangregorio, C.; Miszta, K.; Ghosh, S.; Pellegrino, T.; Manna, L., Copper Sulfide Nanocrystals with Tunable Composition by Reduction of Covellite Nanocrystals with Cu^+ Ions. *J. Am. Chem. Soc.* **2013,** *135*, 17630-17637.

Xue, C.; Mirkin, C. A., pH-Switchable Silver Nanoprism Growth Pathways. *Angew. Chem. Int. Ed.* **2007,** *46*, 2036-2038.

Yang, M.; Xu, J.-Z.; Xu, S.; Zhu, J.-J.; Chen, H.-Y. Preparation of Spherical CuI Nanoparticles. *Inorg. Chem. Commun.* **2004**, *7*, 628-630.

Yao, H.; Shiratsu, T., Individual and Collective Modes of Surface Magnetoplasmon in Thiolate-Protected Silver Nanoparticles Studied by MCD Spectroscopy. *Nanoscale* **2016,** *8*, 11264-11274.

Yu, D.; Wang, C.; Guyot-Sionnest, P., *n*-Type Conducting CdSe Nanocrystal Solids. *Science* **2003,** *300*, 1277-1280.

Yu, W. W.; Qu, L.; Guo, W.; Peng, X., Experimental Determination of the Extinction Coefficient of CdTe, CdSe, and CdS Nanocrystals. *Chem. Mater.* **2003,** *15*, 2854-2860.

Zaitoun, M. A.; Mason, W. R.; Lin, C. T., Magnetic Circular Dichroism Spectra for Colloidal Gold Nanoparticles in Xerogels at 5.5 K. *J. Phys. Chem. B* **2001,** *105*, 6780-6784.

Zhao, Y.; Burda, C., Development of Plasmonic Semiconductor Nanomaterials with Copper Chalcogenides for a Future with Sustainable Energy Materials. *Energy Environ. Sci.* **2012,** *5*, 5564-5576.

Zhao, Y.; Pan, H.; Lou, Y.; Qiu, X.; Zhu, J.; Burda, C., Plasmonic $Cu_{2-x}S$ Nanocrystals: Optical and Structural Properties of Copper-Deficient Copper(I) Sulfides. *J. Am. Chem. Soc.* **2009,** *131*, 4253-4261.